Search for R-parity Violating Supersymmetry in $p-\overline{p}$ collisions at $\sqrt{s}$=1.8 TeV

Nirmalya Parua

Tata Institute of Fundamental Research

Mumbai, India 400 005

1998

Search for R-parity Violating Supersymmetry in $p - \overline{p}$ collisions at $\sqrt{s} = 1.8$ TeV

Nirmalya Parua

Tata Institute of Fundamental Research

Mumbai, India 400 005

A thesis submitted to the

University of Mumbai

for the degree of

Doctor of Philosophy in Physics

September, 1998

To my Parents and Pisi

Acknowledgements

There are many people who helped me reach this point. I shall take this opportunity to express my appreciation and gratitude to them.

I feel extremely fortunate to have Prof. V.S. Narasimham as my thesis advisor. Without his unfailing inspiration, criticism and guidance this work would never have been completed. I am indebted to Prof. N.K. Mondal for his invaluable help at every step in my graduate student life. It is a great pleasure to thank Prof. B.S. Acharya, Dr. Sudeshna Banerjee, Dr. S.R. Dugad and Prof. M.R. Krishnaswamy for their generous help at times of need. Thanks are due to Prof. M.V.S. Rao and Prof. P.R. Vishwanath. I am thankful to Ambreesh, Shankar and Supriya for many helps. Working with Joshi, Kalmani, Nagraj, Reddy, Satya and Sudarshan was very enjoyable. At the time of scintillator detector fabrication staffs of the central workshop and the workshop of HECR group extended tremendous help. In particular I appreciate help from Bhujbal, Elangovan, E.Q. Fernandes, Joseph and Ganesh.

I benefited a lot from the courses on particle physics by Prof. K.V.L. Sharma (Deceased) and Prof. D.P. Roy. I enjoyed many discussions with Prof. Amitava Datta, Prof. Sunanda Banerjee, Dr. Debajyoti Choudhury, Dr. Monoranjan Guchait, Dr. Kajari Mazumdar and Dr. Sreerup Raychaudhury.

I would also like to thank all the members of the DØ collaboration for maintaining such a wonderful facility. In particular I want to thank Prof. Dave Cutts, Dr. Jim Cochran, Prof. Sarah Eno, Prof. Thomas Ferbel, Prof. John Hobbs, Prof. A.S. Ito, Dr. Rich Jesik, Dr. Wyatt Merritt, Dr. Doug Norman, Dr. Marc Paterno for many beneficial discussions as well as suggestions. Thanks are due to Taylor Goss and Cathy Crestinger for making available the detector diagrams. I am grateful to the DØ management for financial support during my stay at Fermilab.

During the six and a half years of graduate student life I have come across many wonderful people both at TIFR and at Fermilab. Subir, Suchandra and Manas were always there with smiling faces when I needed their company. I had nice time with Sandip and Gobinda. Thanks to them for everything they did for me. I am grateful to Soma for her relentless encouragement and prodding at right proportion. She always kept track on the number of chapters I had written on my thesis and demanded progress report at the end of every day. I shall cherish the memories at our weekend dinner club - "The khai-khai Sangha". I thank all of its members : Bunty, Kartik, Zakir, Sarmistha, Sarmistha, Dilip, Pathikrit-da, Chitrak, Goutam-da and Aparajita. I would like to thank Amal, Apurba, Asesh, Biswajit, Bidisha, Chandrasekhar, Dilip, Goutam, Haripada, Hemant, Koushik, Lokesh, Lina, Mita, Mrinal, Mousumi, Nakul, Prabir, Premjit, Pratik, Poulose, Srivatsan, Soumen, Sudipta, Sukesh, Subham, Swagato, Tapan, Vandana, Varsha and many others for their friendship.

During my stay at Fermilab Dhiman and Sudeshna, their parents, Bhola, Swapna-di and Dipan never let me feel that I was away from home. I am grateful to them for many happy moments. I have enjoyed wonderful times with Ashutosh, Bala, Barnali, Brajesh, Djoko, Guoliang, Harpreet, Harsh, Mary Lou, Mrinmoy, Neeti, Prem, Prajakta, Sailesh, Satyadev and Vipin. Thanks to all of them.

Thanks to my teachers Dr. Rampada Mishra and Dr. G. C. Biswas for getting me interested in physics.

I am deeply indebted to all the members of my family for their encouragement and support. Words are insufficient to express my gratitude to them.

Contents

List of Figures

List of Tables

Chapter 1

Introduction

1.1 The Standard Model

The Standard Model (SM) of particle physics describes all the experimentally observed phenomena at the subatomic level ($\sim 10^{-15}$ m). It is a quantum field theory based on $SU(3) \times SU(2) \times U(1)$ symmetry group.

1.1.1 Particle contents and interactions

There are two basic types of particles in this theory, fermions and bosons. Spin 1/2 fermions are the fundamental building blocks of matter and they interact with each other through the exchange of spin 1 bosons, called the gauge bosons.

The fermions can be further classified into two groups; (i) Leptons and (ii) Quarks. There are six flavours of both quarks and leptons which can be grouped into three generations. Properties of each generation are similar except that the particles of higher generations are more massive. Each generation of leptons has one charged particle and one massless neutral particle. Quarks possess fractional charge i.e., either $2/3e$ or 1/3e. Apart from this, quarks carry colour charge (there are three colour charges viz., red, green and blue assigned to them as a matter of convention) for strong interaction.

There are four basic types of interactions in nature. These are (1) the *strong interaction*, responsible for the nuclear binding force, (2) the *electromagnetic interaction*, by which chemical reactions, electrical and magnetic phenomena etc. can be explained, (3) the *weak interaction* which manifests itself in the nuclear β decay and (4) the *gravitational* *interaction*, which is responsible for gravity.

Particles with electric charge participate in the electromagnetic interaction and its carrier is the photon (γ). Photon is massless and does not carry any electric charge. Strong force is mediated by gluons. Gluons are also massless and electrically neutral but they carry the colour charge for strong interaction. There are in total eight of them depending on the colour combination they carry. Because gluons carry the colour charge they have self interaction, whereas photons being electrically neutral do not interact among themselves. The weak interaction is mediated by the $W^{\pm}$ and Z^{0} bosons. Unlike the gluons and photons these are massive ($\sim 100\ GeV/c^2$), which implies that the weak interaction is of very short range ($\sim 10^{-18}$ m). At very high energy ($\sim m_Z$), electromagnetic and weak forces unify and are theoretically treated as a single force called the *Electroweak* force. There is no well-developed gauge theory for gravitational interaction. As its effect in high energy and short distance is negligible, it is left out from any discussion of the Standard Model.

The unbroken electroweak symmetry requires $W^{\pm}$ and Z^{0} bosons to be massless. If it were so, the weak interaction would have infinite range. But it is known that weak interaction has very short range, hence its carriers must be massive. Higgs mechanism was introduced to provide masses to the W and Z bosons by spontaneously breaking this symmetry. But this mechanism requires a new particle, the spin 0 Higgs boson, to be introduced in the Standard Model. The triumph of this mechanism is to predict the masses of the W and Z bosons correctly. The quarks and leptons can also acquire mass through coupling to the Higgs field; the stronger the coupling, the more massive the corresponding particle is.

Some characteristics of the Standard Model particles are shown in Table 1.1. All the particles listed here except the Higgs boson have been either directly observed or inferred. The tau neutrino has not yet been directly observed but experimental data suggests its existence. The recent discovery of the top quark is a boost for the Standard Model. Every effort is being made to find the Higgs boson and it is widely believed that the LHC experiment (which will be operational sometime around 2005) will give us a final answer about its existence.

Fundamental fermions

Particle	Symbol	Mass (MeV)	Charge
Quarks (spin 1/2)			
Up	u	~ 4	2/3
Down	d	~ 7	-1/3
Charm	c	~ 1100	2/3
Strange	s	~ 150	-1/3
Top	t	~ 170000	2/3
Bottom	b	~ 4200	-1/3
Leptons (spin 1/2)			
Electron neutrino	ν_e	$< 15 \times 10^{-3}$	0
Electron	e	.511	-1
Muon neutrino	ν_μ	< 0.27	0
Muon	μ	105	-1
Tau neutrino	ν_τ	< 31	0
Tau	τ	1777	-1

Gauge bosons

Particle	Symbol	Mass (GeV)	Charge	Force
Gluon	g	0	0	Strong
Photon	γ	0	0	Electromagnetic
$W^\pm$	$W^\pm$	80	± 1	Weak (Charged)
Z	Z	91	0	Weak (Neutral)

Fundamental scalar

Particle	Symbol	Mass (MeV)	Charge
Higgs	H	?	?

Table 1.1: Particle contents of the Standard Model.

1.1.2 Shortfalls of the Standard Model

Precision measurements of the values of some of the key quantities of the Standard Model (viz., m_Z, Γ_Z, m_t, $sin^2\theta_w$, α_s) at the LEP, SLC and Tevatron experiments in the recent years have confirmed the validity of the SM. But in spite of its tremendous success it is not considered a fundamental theory for various reasons, some of which are listed below.

(i) Standard Model has a large number of free parameters whose values, although measured very accurately, are not predicted by the theory. (ii) There is no understanding of the replication of generation or prediction of their exact number. (iii) Although Higgs mechanism gives the masses to W and Z boson, it was added in an ad hoc manner; the SM does not predict the electroweak symmetry breaking (EWSB) by itself. (iv) A truly fundamental theory is expected to have an unified description of all the forces including gravity at some high energy scale. (v) Although there is no theoretical prediction for the mass of Higgs, it is constrained to be less than about a TeV from the perturbative unitarity condition. But within the Standard Model there is no symmetry which protects the mass of Higgs particle from large radiative corrections. This is a feature associated with only scalar fields. Masses of all other particles are protected by some mechanism, e.g., photon remains massless due to the exact U(1) gauge invariance of QED or the correction term to the mass of electron is very small due to chiral symmetry. The radiative correction(δm_H) to the mass of the Higgs (m_H) diverges quadratically as the internal momentum in the loop (one such diagram is shown in Fig. 1.1) becomes very large.

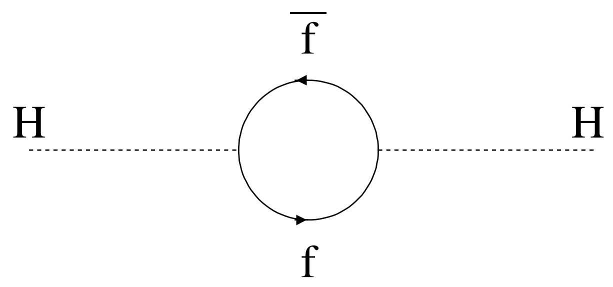

Figure 1.1: Radiative correction to the Higgs mass in the SM.

This can be mathematically expressed as

$$m_H^2(\mu_2) = m_H^2(\mu_1) + Cg^2 \int_{\mu_2^2}^{\mu_1^2} dk^2 + Rg^2 + O(g^4) \tag{1.1}$$

Where μ_2 is the electroweak scale, $\sim m_W$; $m_H(\mu_2)$ is the running mass of the Higgs boson evaluated at the electroweak scale; μ_1 is the scale where new physics becomes important (for example, in GUTs, $\mu_1 \sim 10^{15}$ GeV); g is the coupling constant; C is a dimensionless quantity and R grows almost logarithmically with μ_1 as $\mu_1 \to \infty$.

The term proportional to C in equation 1.1 diverges quadratically with μ_1 and is $\sim 10^{30}$ at the GUT scale. So, in order to get $m_H(\mu_2) \sim 1$ TeV, one has to fine tune $m_H(\mu_1)$ extremely accurately to cancel out the quadratically divergent term. This is called the fine tuning problem and the huge difference between the two scales μ_1 and μ_2 is referred to as the hierarchy problem.

1.1.3 Beyond the Standard Model

There are various theoretical attempts to solve the above problems. One of them is the technicolour model in which there are no light elementary scalar Higgs particles. In this theory Higgs particle is composite of more fundamental fermions. Nearly all technicolour models predict the existence of low mass (< 25 GeV/c^2) charged technipions (which are like charged Higgs bosons). However there is no evidence for them in the existing data.

An alternative approach to solve some of these problems is Supersymmetry (SUSY) [1–6]. As the aim of this thesis is to search for supersymmetry, it is discussed in some detail in the next section.

1.2 Supersymmetry

Supersymmetry is a novel type of symmetry that interrelates bosons and fermions. It solves the fine tuning problem in an elegant way by introducing a supersymmetric particle (sparticle) corresponding to each SM particle with spin differing by 1/2 and all other quantum numbers remaining the same. The additional diagrams which contribute to the radiative correction to the Higgs boson mass in the presence of Supersymmetry are shown in Fig. 1.2.

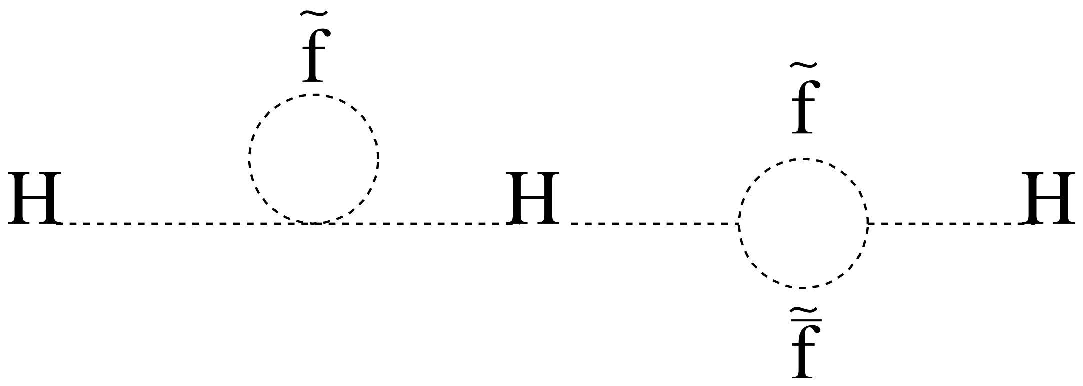

Figure 1.2: Additional diagrams for the radiative correction to the Higgs mass when SUSY is introduced.

The radiative corrections to the mass of Higgs involving loop diagrams of fermions cancel those involving sfermions. The cancellation would be exact if sparticles had mass equal to their SM counterpart. But that is obviously not the case because no selectron with mass 511 KeV/c^2 or smuon with mass 106 MeV/c^2 has been found. So Supersymmetry must be a broken symmetry. But if SUSY has to ameliorate the fine tuning problem, sparticles must have masses smaller than O(1 TeV). This provides ample motivation to search for supersymmetric particles in the existing high energy colliders at Tevatron, CERN or DESY. Further motivation of low energy SUSY is provided by the observation of Amaldi et al. [7]. According to their analysis, the strong and electroweak coupling constants do not meet at a single unification point when they are evolved using Standard Model parameters only, from their values at the electroweak scale measured at LEP to higher energy using renormalisation group equation (Fig. 1.3a). In contrast, the Minimal Supersymmetric Standard Model with SUSY scale around 1 TeV leads to a single unification scale of $\sim 10^{16}$ GeV (Fig. 1.3b).

1.2.1 Minimal Supersymmetric Standard Model

The Minimal Supersymmetric Standard Model (MSSM) is the simplest supersymmetrisation of the Standard Model in which the smallest number of new particles and new interactions are added. The particle content of the MSSM is shown in the Table 1.2. For each of the SM chiral fermions f_i (i=L,R) it contains a spin zero superpartner $\tilde{f}_i$. Similarly there are eight gluinos corresponding to eight gluons. In the electroweak sector there are

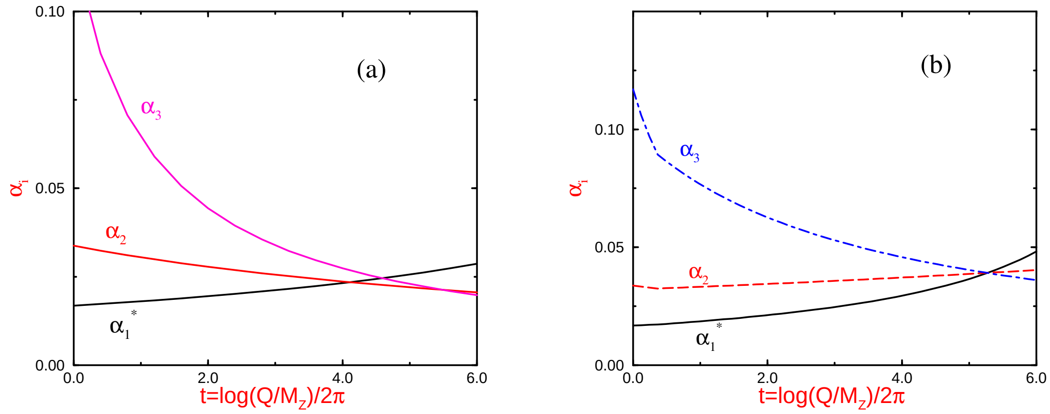

Figure 1.3: Evolution of the gauge coupling constants from the experimentally measured values at the Z-pole: (a)in the case of the Standard Model and (b) in the case of low energy SUSY model.

wino, zino and a photino as superpartners of $W^{\pm}$, Z and photon respectively. But the Higgs sector needs to be extended once SUSY is introduced. This is because, in the Standard Model the electroweak symmetry is broken by a single Higgs doublet which acquires a non vanishing vacuum expectation value in the ground state. The single Higgs field could give masses to all the SM fermions, because the doublet (complex conjugate of the doublet) can couple to the $T_3 = 1/2$ ($T_3 = -1/2$) fermions in a gauge invariant way. But mass of particles in the presence of Supersymmetry comes from a superpotential which cannot depend on a field as well as its complex conjugate. Thus, in order to give masses to all the fermions, two Higgs doublets h and h', with vacuum expectation values v and v' are introduced. These two Higgs fields have their supersymmetric partner fields (higgsino field) $\tilde{h}$ and $\tilde{h}'$ respectively. Consequently, in the extended Higgs sector of SM there are five Higgs particles; two charged scalar Higgs $H^{\pm}$, two neutral scalar Higgs H and h and one pseudoscalar Higgs A. The ratio of the vacuum expectation values v/v' of the two Higgs doublets, also referred to as $tan\beta$, has an important role in supersymmetry. Another parameter originating from the Higgs sector is the higgsino mass parameter, μ. Electroweak gauginos (winos and binos) and Higgsinos with same $SU(2) \times U(1)$ quantum number can mix when electroweak symmetry is broken. Thus, bino, neutral winos and neutral higgsinos mix to form four neutralinos ($m_{\tilde{\chi}^0_1}, m_{\tilde{\chi}^0_2}, m_{\tilde{\chi}^0_3}, m_{\tilde{\chi}^0_4}$) where $m_{\tilde{\chi}^0_1} < m_{\tilde{\chi}^0_2} < m_{\tilde{\chi}^0_3} < m_{\tilde{\chi}^0_4}$. Similarly charged winos and charged higgsinos form two chargino pairs ($m_{\tilde{\chi}^{\pm}_1}, m_{\tilde{\chi}^{\pm}_2}$) with

	Particles		Sparticles	Mass Eigenstates
Quarks (Spin 1/2)	u_L, u_R, d_L, d_R c_L, c_R, s_L, s_R t_L, t_R b_L, b_R	Squarks (Spin 0)	$\tilde{u}_L$, $\tilde{u}_R$, $\tilde{d}_L$, $\tilde{d}_R$ $\tilde{c}_L$, $\tilde{c}_R$, $\tilde{s}_L$, $\tilde{s}_R$ $\tilde{t}_L$, $\tilde{t}_R$ $\tilde{b}_L$, $\tilde{b}_R$	$\tilde{u}_L$, $\tilde{u}_R$, $\tilde{d}_L$, $\tilde{d}_R$ $\tilde{c}_L$, $\tilde{c}_R$, $\tilde{s}_L$, $\tilde{s}_R$ $\tilde{t}_1$, $\tilde{t}_2$ $\tilde{b}_1$, $\tilde{b}_2$
Leptons (Spin 1/2)	e_L, ν_{eL}, e_R μ_L, $\nu_{\mu L}$, μ_R τ_L, $\nu_{\tau L}$, τ_R	Sleptons (Spin 0)	$\tilde{e}_L$, $\tilde{\nu}_{eL}$, $\tilde{e}_R$ $\tilde{\mu}_L$, $\tilde{\nu}_{\mu L}$, $\tilde{\mu}_R$ $\tilde{\tau}_L$, $\tilde{\nu}_{\tau L}$, $\tilde{\tau}_R$	$\tilde{e}_L$, $\tilde{\nu}_{eL}$, $\tilde{e}_R$ $\tilde{\mu}_L$, $\tilde{\nu}_{\mu L}$, $\tilde{\mu}_R$ $\tilde{\tau}_L$, $\tilde{\nu}_{\tau L}$, $\tilde{\tau}_R$
	g		$\tilde{g}$	$\tilde{g}$
Gauge Bosons (Spin 0)	γ Z h,H,A	Gauginos (Spin 1/2)	$\tilde{\gamma}$ $\tilde{Z}$ $\tilde{H}^0_{1,2}$	$\tilde{\chi}^0_{1,2,3,4}$ (Neutralinos)
Gauge Bosons Higgs Boson	$W^{\pm}$ $H^{\pm}$	Gauginos Higgsinos	$\tilde{W}^{\pm}$ $\tilde{H}^{\pm}$	$\tilde{\chi}^{\pm}_{1,2}$ (Charginos)

Table 1.2: Particle content of the MSSM.

$m_{\tilde{\chi}_1^{\pm}} < m_{\tilde{\chi}_2^{\pm}}$. The wino, bino and higgsino content of the neutralinos and charginos are determined by $tan(\beta)$ and μ.

1.2.2 Minimal Supergravity

In MSSM, the lack of proper understanding of the SUSY breaking mechanism leads to a large number of soft SUSY breaking masses and interactions ($\sim$ 100). Unless further theories about the SUSY-breaking interactions are in place, this leads to a proliferation of model dependent parameters making systematic search for supersymmetric particles impossible. One attractive theory is the Supergravity (SUGRA) [8–10] which unifies the strong, weak, electromagnetic and gravitational forces at some very large energy scale, M_X. This energy scale may be the GUT scale ($\sim 10^{16}$ GeV) or the Planck scale ($\sim 10^{19}$ GeV). The parameters needed to describe SUGRA are as follows :

- m_0, the common mass for scalar fermions at the unification scale
- $m_{1/2}$, the common mass for all gauginos at the unification scale
- $tan(\beta)$, the ratio of the vacuum expectation values of the two Higgs doublets

- A_0, common trilinear coupling constant at the unification scale
- $sign(\mu)$, the sign of the Higgsino mixing parameter.

If one assumes that there is no new physics process between the unification and the electroweak scale, it is straightforward to determine the masses and mixing angles of SUSY particles at the electroweak scale by evolving the SUSY parameters from the unification scale down to the electroweak scale by using renormalisation group equations. One typical example of such evolution is shown in Fig. 1.4.

In the following, we show a few important relationships to the lowest order in the SUGRA model:

$$m_{\tilde{g}} = m_3(m_W) = \frac{\alpha_3(m_W)}{\alpha_{GUT}(m_W)} m_{1/2} \tag{1.2}$$

$$m_i(m_W) = \frac{g_i^2}{g_{GUT}^2} m_{1/2} \tag{1.3}$$

$$\begin{aligned}
m_{\tilde{u}_L}^2 &= m_0^2 + 6.28 m_{1/2}^2 + 0.35 m_Z^2 cos(2\beta) \\
m_{\tilde{d}_L}^2 &= m_0^2 + 6.28 m_{1/2}^2 - 0.42 m_Z^2 cos(2\beta) \\
m_{\tilde{u}_R}^2 &= m_0^2 + 5.87 m_{1/2}^2 + 0.16 m_Z^2 cos(2\beta) \\
m_{\tilde{d}_R}^2 &= m_0^2 + 5.82 m_{1/2}^2 - 0.08 m_Z^2 cos(2\beta) \\
m_{\tilde{\nu}_L}^2 &= m_0^2 + 0.52 m_{1/2}^2 + 0.50 m_Z^2 cos(2\beta) \\
m_{\tilde{e}_L}^2 &= m_0^2 + 0.52 m_{1/2}^2 - 0.27 m_Z^2 cos(2\beta) \\
m_{\tilde{e}_R}^2 &= m_0^2 + 0.15 m_{1/2}^2 - 0.23 m_Z^2 cos(2\beta) \\
m_{\tilde{b}_R}^2 &= m_{\tilde{d}_R}^2 \\
m_{\tilde{b}_L}^2 &= m_{\tilde{d}_L}^2 - 0.49 m_0^2 - 1.21 m_{1/2}^2 \\
m_{\tilde{t}_R}^2 &= m_{\tilde{u}_R}^2 + m_t^2 - 0.99 m_0^2 - 2.42 m_{1/2}^2 \\
m_{\tilde{t}_L}^2 &= m_{\tilde{u}_L}^2 + m_t^2 - 0.49 m_0^2 - 1.21 m_{1/2}^2
\end{aligned} \tag{1.4}$$

Here m_1, m_2, m_3, are the gaugino masses associated with U(1), SU(2) and SU(3) subgroups of the SM.

The value of μ can be determined from the following formula

$$tan^2(\beta) = \frac{\mu^2 + m_{H_1}^2 + m_Z^2/2}{\mu^2 + m_{H_2}^2 + m_Z^2/2} \tag{1.5}$$

In the limit of $|\mu| \gg m_2, m_Z$, the masses of charginos and neutralinos reduce to

$$
\begin{aligned}
m_{\tilde{\chi}_1} \simeq & m_2 - \frac{m_W^2}{\mu^2}(m_2 + \mu sin2\beta) \\
m_{\tilde{\chi}_1} \simeq & |\mu| + \frac{m_W^2}{\mu^2}\epsilon_\mu(m_2 sin2\beta + \mu) \\
m_{\tilde{\chi}_1^0} \simeq & m_1 - \frac{m_Z^2}{\mu^2}(m_1 + \mu sin2\beta)sin^2\theta_W \\
m_{\tilde{\chi}_2^0} \simeq & m_2 - \frac{m_W^2}{\mu^2}(m_2 + \mu sin2\beta)cos^2\theta_W \\
m_{\tilde{\chi}_3^0} \simeq & |\mu| + \frac{1}{2}\frac{m_Z^2}{\mu^2}\epsilon_\mu(1 - sin2\beta)(\mu + m_2 sin^2\theta_W + m_1 cos^2\theta_W) \\
m_{\tilde{\chi}_4^0} \simeq & |\mu| + \frac{1}{2}\frac{m_Z^2}{\mu^2}\epsilon_\mu(1 + sin2\beta)(\mu - m_2 sin^2\theta_W - m_1 cos^2\theta_W)
\end{aligned}
\tag{1.6}
$$

One added attraction of the SUGRA model, apart from its having less number of free parameters, is that it induces the electroweak symmetry breaking by driving the Higgs mass parameter to a negative value at the electroweak scale. Moreover, a common scalar mass at the unification scale leads to an approximate degeneracy of the first two generations of squarks masses, which is required in understanding the phenomenology of K mesons [11].

1.2.3 R-parity Violation

The most general superpotential can be written as

$$W = W_1 + W_2 \tag{1.7}$$

Where

$$W_1 = W_{MSSM} = h^e_{ij} L_i H_1 \overline{E}_j + h^d_{ij} Q_i H_1 \overline{D}_j + h^u_{ij} Q_i H_2 \overline{U}_j + \mu H_1 H_2 \tag{1.8}$$

and

$$W_2 = \lambda_{ijk} L_i L_j \overline{E_k} + \lambda^{'}_{ijk} L_i Q_j \overline{D_k} + \lambda^{''}_{ijk} \overline{U_i D_j D_k} \tag{1.9}$$

where L and $\overline{E}$ (Q and $\overline{U}, \overline{D}$) correspond to left-handed lepton doublet and the antilepton singlet (quark doublet and antiquark singlets) chiral superfields respectively, and i,j,k

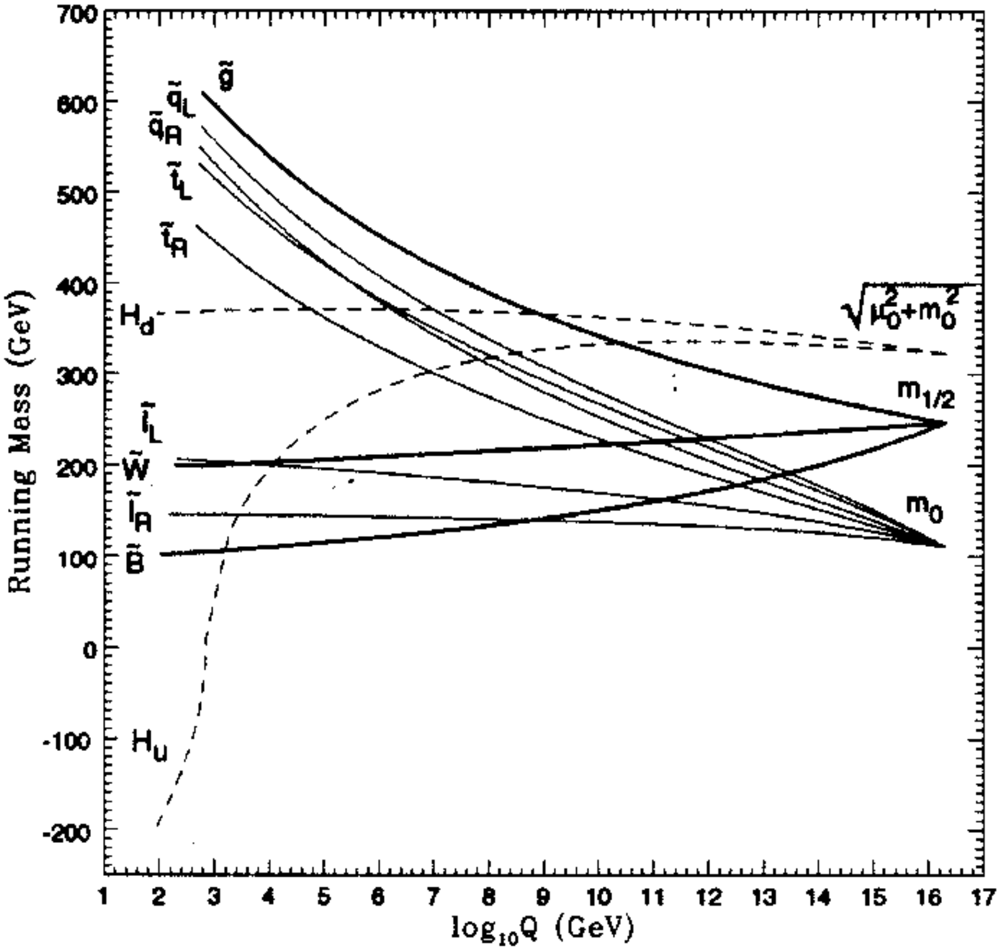

Figure 1.4: Evolution of Sparticle mass parameters in SUGRA.

are the generation indices. H_1 and H_2 are the two Higgs fields. The terms in W_2 can be simplified in terms of scalar and fermionic components as follows:

$$\lambda_{ijk} l_i \tilde{l}_j \overline{e_k} + \lambda'_{ijk} l_i \tilde{q}_j \overline{d_k} + \lambda''_{ijk} \overline{u_i} \overline{\tilde{d}_j} \overline{d_k} \tag{1.10}$$

These terms, however, violate either baryon or lepton number, and can generate an unacceptably large rate for proton decay. To prevent this, the conservation of a new multiplicative quantum number, called the R-parity, is imposed. R-parity is defined as $(-1)^{3B+L+2S}$, where L is the lepton number, B is the Baryon number and S is spin of the particle. R parity is +1 for Standard Model particles and -1 for their superpartners. The conservation of R-parity implies that SUSY particles are pair produced and their decay in cascades must terminate in LSPs (Lightest Supersymmetric Particles). In most SUSY models, the LSP is the lightest neutralino $\tilde{\chi}_1^0$. Being a weakly interacting particle, LSP escapes detection, resulting in events with large missing transverse energy ($\not{E}_T$), which is the canonical signature used extensively in the SUSY searches at $p\overline{p}$ colliders as well as at LEP. However, as can be seen from Fig. 1.5, for the stability of the proton, either lepton number conservation or baryon number conservation is necessary and sufficient. Therefore, R-parity conservation, i.e., conservation of both lepton and baryon numbers, is not needed.

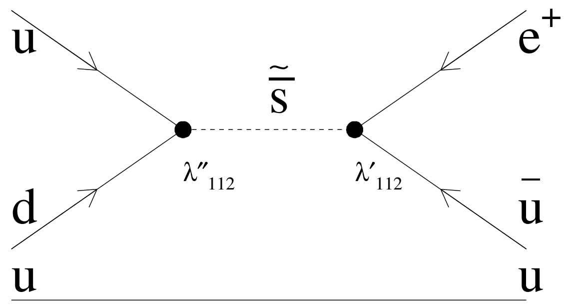

Figure 1.5: Proton decay via $\lambda^{''}_{112}$ and $\lambda^{'}_{112}$ couplings.

We can therefore consider two R-parity violating scenarios.

(i) λ_{ijk} and/or $\lambda^{'}_{ijk} \neq 0$ and $\lambda^{''}_{ijk} = 0$

This will produce lepton number violation but will conserve baryon number.

(ii) $\lambda^{''}_{ijk} \neq 0$ and λ_{ijk}, $\lambda^{'}_{ijk} = 0$

This will produce baryon number violation but will conserve lepton number.

In either case, the LSP need no longer be stable, and can decay as follows (Fig. 1.6):

$\tilde{\chi}_1^0 \xrightarrow{\tilde{l}} l_i l_j \overline{e_k} \quad (\lambda_{ijk} \neq 0)$

$\tilde{\chi}_1^0 \xrightarrow{\tilde{q}} l_i q_j \overline{d}_k \quad (\lambda^{'}_{ijk} \neq 0\ )$

$\tilde{\chi}_1^0 \xrightarrow{\tilde{q}} u_i d_j d_k \quad (\lambda^{''}_{ijk} \neq 0\ )$

The Yukawa couplings $\lambda_{ijk}(\lambda^{''}_{ijk})$ are antisymmetric in the first (last) two generation indices which implies that

$\lambda_{ijk} = -\lambda_{jik}$ & $\lambda^{''}_{ijk} = -\lambda^{''}_{ikj}$

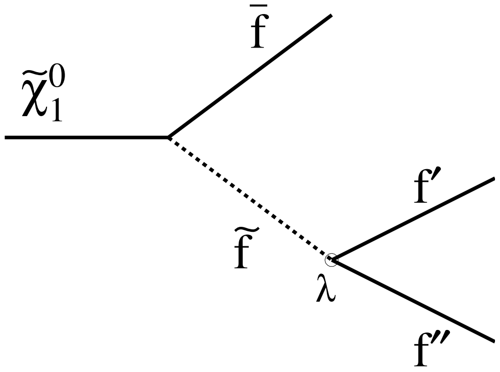

Figure 1.6: Decay of LSP, where f denotes either a quark or a lepton and $\tilde{f}$ is the squark or slepton.

Thus there are 9 independent λ and λ'' couplings and 27 λ' coupling terms, which add up to a total of 45 independent R-parity violating coupling terms.

It is however impossible to search for such a large number of R-parity violating Yukawa interactions in any single analysis. The following three assumptions are therefore made to limit the parameter space for the present search.

1. Out of the 45 R-parity violating coupling terms only one dominates. This assumption is based on the fact that the new couplings are similar in nature to the SM Yukawa couplings, where only the top quark Yukawa term dominates.

2. The R-parity violating couplings under consideration are strong enough so that the LSP is unstable and decays within the detector.
The decay length of the LSP, for the decay mode shown in Fig. 1.6, is given by [12]

$$c\gamma\tau_{\tilde{\chi}_1^0} \sim 3\gamma.10^{-3}(m_{\tilde{f}}/100GeV)^4(1GeV/m_{\tilde{\chi}_1^0})^5(1/\lambda)^2 \; m \qquad (1.11)$$

where $c\gamma\tau_{\tilde{\chi}_1^0}$ is the decay length (c is the velocity of light, γ is the Lorentz boost factor for the LSP, and τ is the lifetime of the LSP in its rest frame), $m_{\tilde{f}}$ is the mass of the sfermion, $m_{\tilde{\chi}_1^0}$ is the mass of the LSP and λ is the strength of the R-parity violating coupling.

For the LSP to decay close to the interaction vertex (< 1 cm), one needs

$$c\gamma\tau_{\tilde{\chi}_1^0} < 1\ cm \qquad (1.12)$$

From Equations 1.11 and 1.12 we get

$$\lambda > 0.5\gamma^{1/2}(m_{\tilde{f}}/100GeV)^2(1GeV/m_{\tilde{\chi}_1^0})^{5/2} \qquad (1.13)$$

Using $m_{\tilde{f}} \sim 200$ GeV, $m_{\tilde{\chi}_1^0} \sim 30$ GeV and $\gamma \sim 10$, as typical values, we get

$$\lambda > 0.001 \qquad (1.14)$$

Although, at present, there is no information on the possible values of these λ parameters there are strong phenomenological upper limits on the strengths for many of them. These are listed in Table 1.3. A complete discussion of how these limits were obtained can be found elsewhere [13]. From the table one can see that, even after taking into account the existing limits, for most of these couplings, there exists a large allowed range that satisfies relation (1.14).

ijk	λ_{ijk}	ijk	λ'_{ijk}	ijk	λ'_{ijk}	ijk	λ'_{ijk}	ijk	λ''_{ijk}
121	0.05	111	0.001	211	0.09	311	0.16	112	10^{-6}
122	0.05	112	0.02	212	0.09	312	0.16	113	10^{-5}
123	0.05	113	0.02	213	0.09	313	0.16	123	1.25
131	0.06	121	0.035	221	0.18	321	0.20	212	1.25
132	0.06	122	0.06	222	0.18	322	0.20	213	1.25
133	0.004	123	0.20	223	0.18	323	0.20	223	1.25
231	0.06	131	0.035	231	0.22	331	0.26	312	0.43
232	0.06	132	.33	232	0.39	332	0.26	313	0.43
233	0.06	133	0.002	233	0.39	333	0.26	323	0.43

Table 1.3: Upper limits on couplings (all values should be multiplied by $\frac{m_{\tilde{f}}}{100}$GeV).

3. For the present analysis, it is also assumed that only the LSP decays through R-parity violating channels. Branching ratios for other SUSY particles to decay through R-parity violating modes are negligible compared to those of the R-parity conserving modes. This assumption is again justified, because the strengths of the

R-violating couplings indicated in Table 5.4 are small compared to R-conserving couplings of Standard Model. A more detailed discussion of the branching ratios of R-violating vs R-conserving decays can be found in Ref [14].

1.3 Status of the search for supersymmetric particles

Although Supersymmetry has been a subject of extensive theoretical and experimental scrutiny over the past decade no experimental evidence has been found yet. Limits on the masses, couplings and cross-sections of supersymmetric particles have been set from these negative results. In this section we briefly summarise the present status of searches both with R-parity conservation and R-parity violation.

1.3.1 Searches with R-parity conservation

Experiments at the CERN e^+e^- collider (LEP1) ruled out the existence of sleptons, squarks and charginos lighter than $m_Z/2$ in a model independent way. All other limits are model dependent. The most stringent *lower* limits on the masses of squarks and gluinos come from searches at DØ [15, 16] and CDF [17] in the $\not{E}_T$+ jets and dileptons + jets + $\not{E}_T$ channels.

The DØ limit on the gluino mass is 185 GeV/c^2 for $tan\beta$ =2 and 134 GeV/c^2 for $tan\beta = 6$. The CDF limit on the mass of gluino is 180 GeV/c^2 for large value of squark mass and for $tan\beta$ =4.
For equal masses of squarks and gluinos the limits are 267 GeV/c^2 (for $tan\beta$ =2) and 220 GeV/c^2 (for $tan\beta$ =4) from DØ and CDF respectively.
The limit on the squark mass (except stop) from DØ is 250 GeV/c^2 for $tan\beta$ =2.

DØ has searched for the stop pair production [18] in the scenario in which the lighter of the two, i.e., $\tilde{t}_1$, decays with 100% branching fraction to charm quark and the lightest neutralino $\tilde{\chi}_1^0$, yielding two acollinear jets and $\not{E}_T$.
The resulting lower limit on $m_{\tilde{t}_1}$ is 93 GeV/c^2 for $m_{\tilde{\chi}_1^0} = 8\ GeV/c^2$.
The ALEPH collaboration [19] has set a lower limit of 70 GeV/c^2 on stop mass from the analysis in the $\tilde{t} \to bl\tilde{\nu}$ channel using data taken at $\sqrt{s}$ = 161, 170 and 172 GeV.

ALEPH collaboration has analysed data taken at $\sqrt{s}$= 161 and 172 GeV to search for sleptons [20]. Their limits depend on the mass difference between sleptons and the lightest

neutralino.
The lower limits on $m_{\tilde{\mu}_R}$, $m_{\tilde{\tau}_R}$ are 59 and 53 GeV/c^2 respectively.
For $m_{\tilde{e}_R}$ the limits range from 75 GeV/c^2 to 58 GeV/c^2 depending on various assumptions. For mass degenerate sleptons the limit is 76 GeV/c^2. All these lower limits are derived for μ=-500 GeV and $tan\beta$ =2.

Both DØ and CDF have looked for chargino-neutralino signal in the trilepton (eee, eeμ, e$\mu\mu$ and $\mu\mu\mu$) + $\not{E}_T$ final states and put limit on the $\sigma_{\tilde{\chi}_1^{\pm}\tilde{\chi}_2^0}.BR(\tilde{\chi}_1^{\pm}\tilde{\chi}_2^0 \rightarrow 3l + \not{E}_T)$ as a function of $m_{\tilde{\chi}_1^{\pm}}$.
DØ limits [21] are 0.66 pb for $m_{\tilde{\chi}_1^{\pm}} = 45$ GeV/c^2 and 0.01 pb for $m_{\tilde{\chi}_1^{\pm}} = 124$ GeV/c^2.
CDF limits [22] are 0.34 pb for $m_{\tilde{\chi}_1^{\pm}} > 81.5$ GeV/c^2 and $m_{\tilde{\chi}_2^0} > 82.2$ GeV/c^2.
To compare the DØ and the CDF results one should note that the DØ limit is on the average of 4 modes (eee, $ee\mu$, $e\mu\mu$ and $\mu\mu\mu$) whereas the CDF limit is on the sum.
ALEPH also searched for chargino [23] and put a lower limit on the mass of chargino at 85.5 GeV/c^2 for gaugino-like chargino ($\mu = -500$ GeV/c^2), and 85.0 GeV/c^2 for Higgsino-like charginos ($m_2 = 500$ GeV/c^2), for $m_{\tilde{\nu}} \geq 200$ GeV/c^2 and $tan\beta = \sqrt{2}$.

1.3.2 Searches with R-parity violation

Searches at LEP

OPAL had searched [24] for massive unstable photinos using a data sample collected at $\sqrt{s} = m_Z$. Photinos could be produced through selectron exchange conserving R-parity. Assuming that they decay into $\tau^{\pm}l^{\pm}\nu_l$ ($l = e$ or μ) through lepton number violating λ_{123} coupling, an exclusion contour in the $(m_{\tilde{e}}, m_{\tilde{\gamma}})$ plane was obtained from the data as shown in Fig. 1.7.

L3 collaboration [25] had looked for deviations in the cross-section and the forward-backward asymmetries in the reactions $e^+e^- \rightarrow e^+e^-$ and $e^+e^- \rightarrow \mu^+\mu^-$ due to the effect of R-parity breaking $\tilde{\nu}_\tau$ exchange. The study was made for energies ranging from 91 GeV to 172 GeV which lead to exclusion contours as shown in Fig. 1.8.

ALEPH collaboration [26] had reported search for supersymmetry with non-zero values of R-parity violating λ_{ijk} couplings at the energy $\sqrt{s} = m_Z$.
Scalar leptons of all flavours are ruled out for the mass range of 12 GeV/c^2 to 45.6 GeV/c^2.
For squarks (except stop), the limits range from 12 GeV/c^2 to 45.3 GeV/c^2.
Stops are also excluded in the mass range of 11 GeV/c^2 to 41 GeV/c^2.

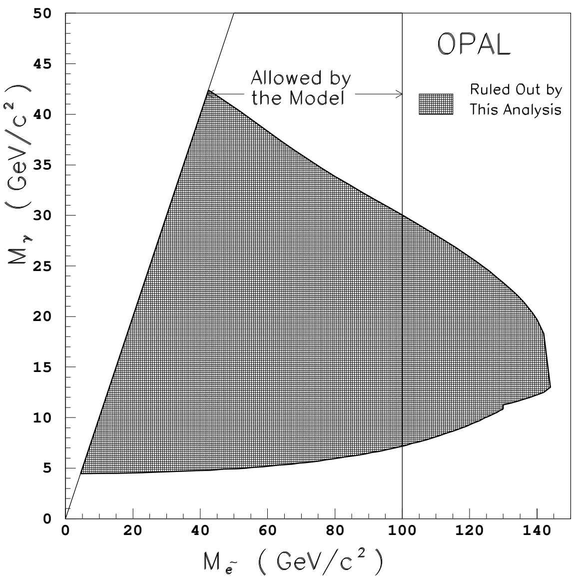

Figure 1.7: 95% C.L. exclusion contour in the $m_{\tilde{\gamma}}$ versus $m_{\tilde{e}}$ plane as obtained by the OPAL collaboration.

All these results are based upon the assumption that $\tilde{g}$ is much heavier than $\tilde{q}$.
Charginos up to $m_Z/2$ are excluded (without any dedicated search) since the production of charginos can seriously alter the Z decay width.

Recently ALEPH [27] reported another search for supersymmetry with R-parity violating λ coupling at the centre of mass energies of 130 GeV to 172 GeV. Charginos with masses less than 73 GeV/c^2 and neutralinos with masses less than 23 GeV/c^2 are excluded at 95 % C.L. in the most conservative case. For the most conservative choice of the coupling, the mass limits for $tan\beta = 2$ are:
$m_{\tilde{e}_R} > 64$ GeV/c^2, $m_{\tilde{\mu}_R} > 62$ GeV/c^2, $m_{\tilde{\tau}_R} > 56$ GeV/c^2,

$m_{\tilde{\nu}_e} > 72$ GeV/c^2, $m_{\tilde{\nu}_\mu}, m_{\tilde{\nu}_\tau} > 49$ GeV/c^2,

$m_{\tilde{t}_L} > 60$ GeV/c^2, $m_{\tilde{b}_L} > 58$ GeV/c^2.

Searches at HERA

In e-p collisions, a single squark can be produced through R-parity violating λ' coupling. The H1 group has searched for direct single production of squarks (R-parity violating production) via λ' coupling [28]. All possible R-parity violating decays and gauge decays of squarks were taken into account when scanning the parameter space of the MSSM. As

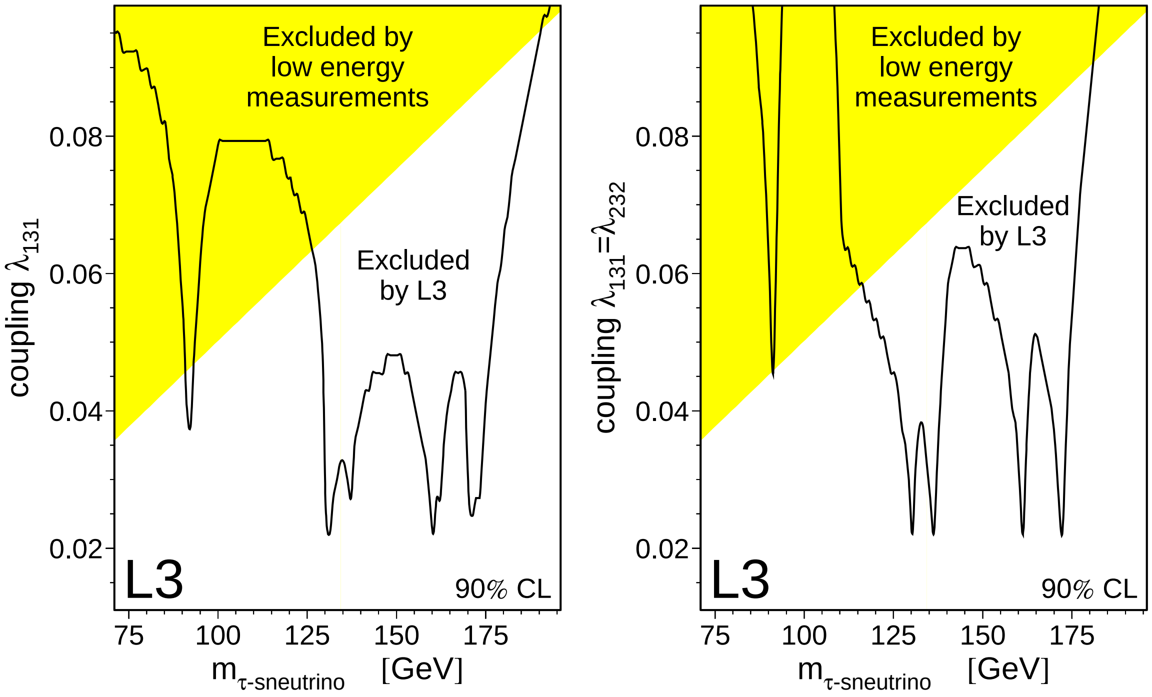

Figure 1.8: Upper limits on the coupling strengths as a function of $m_{\tilde{\nu}_\tau}$. The shaded area is excluded by low energy measurements and the solid line shows the 90% C.L. upper limit from L3 analysis.

no significant evidence of the production was found, mass dependent limits on the couplings were given (shown in Fig. 1.9). First generation squarks below mass of 240 GeV/c^2 are ruled out at 95 % C.L. for the strength of the Yukawa coupling of $\lambda'_{111}/4\pi = \alpha_{em}$. Stop squarks are searched in pair and single production modes. Light stop is ruled out between masses 9 GeV/c^2 to 24.4 GeV/c^2 at 95 % confidence level for non-zero values of λ'_{13k} couplings. For λ'_{131} coupling with strength $(\lambda'_{131} \times cos\theta_t)^2/4\pi \geq 0.01\alpha_{em}$, stops below 138 GeV/$c^2$ are ruled out.

Searches at Tevatron

The first search for R-parity violating supersymmetry at Tevatron was done using dilepton data taken by CDF collaboration [29]. In that analysis lepton number violating couplings were assumed to have non-zero values. The lower limit obtained on the mass of squark/gluino $\sim$ 100 GeV/c^2 is comparable to the corresponding limit obtained for the R-parity conserved modes in Tevatron experiments.

The observation of the excess of high Q^2 events at HERA experiments [30, 31] have sparked

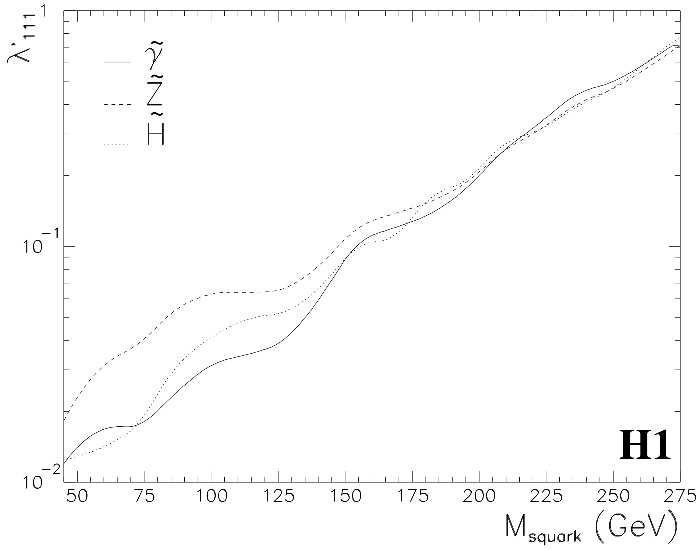

Figure 1.9: 95% CL exclusion upper limits for the coupling λ'_{111} as a function of squark mass for different natures of the LSP (mass 40 GeV/c^2) at $tan\beta = 1$. The regions above the curves are excluded by the H1 group.

interest in $\not{R}_p$ SUSY, because such events can be explained by the production and decay of a charm squark of mass $\sim$ 200 GeV/c^2 when R-parity is violated [32, 33]. The preferred coupling for this scenario is λ'_{121}. CDF collaboration has searched for two $\not{R}_p$ processes involving λ'_{121} coupling [34] :

(i) $p\overline{p} \rightarrow \tilde{g}\tilde{g} \rightarrow (c\tilde{c}_L)(c\tilde{c}_L) \xrightarrow{\not{R}_p} c(e^{\pm}d)c(e^{\pm}d)$ and

(ii) $p\overline{p} \rightarrow \tilde{q}\tilde{\overline{q}} \rightarrow (q\tilde{\chi}_1^0)(\overline{q}\tilde{\chi}_1^0) \xrightarrow{\not{R}_p} q(dce^{\pm})\overline{q}(dce^{\pm})$.

From the first analysis they excluded the scenario of a 200 GeV/c^2 $\tilde{c}_L$ as a function of the masses of $\tilde{g}$ and $\tilde{q}$. By the second analysis $\tilde{t}_1$ below 135 GeV/c^2 was ruled out under a heavy neutralino scenario. For the case of heavy neutralinos and gluinos ($m_{\tilde{g}}$ = 200 GeV/c^2), the squark masses (excluding that of stop) below 260 GeV/c^2 is ruled out.

1.4 Overview of the Thesis

From the discussion presented above it is clear that a large amount of the SUSY parameter space remains unexplored. The large centre of mass energy of 1.8 TeV at Tevatron and about 100 pb^{-1} of data collected with the DØ detector are used for the present thesis to study R-parity violating SUSY signals for the first time in DØ. We have performed a search for R-parity violating supersymmetry assuming non-zero values of λ'_{ijk} couplings involving first generation leptons. We assume that supersymmetric particles are produced in pairs, and decay into lighter supersymmetric particles, and finally to LSP s. Then each LSP decays into one electron (or neutrino) and two quarks. The signal we seek will therefore be comprised of final states with two or more electrons and four or more jets. The DØ detector is well suited for this study. In this thesis we describe this search in detail. The rest of the thesis is organised as follows:

Chapter 2 discusses the apparatus used in this search, viz., the Tevatron and the DØ detector. Chapter 3 explains in some detail how the data are taken and written in the format useful for the analysis. This chapter also describes the identification techniques of various useful objects e.g., electrons, jets etc. in the detector. Event selection criteria, analysis of experimental data and estimation of background are discussed in Chapter 4. Chapter 5 describes how cross-section limits are extracted at various points in the m_0-$m_{1/2}$ plane starting from the signal efficiency, number of events passing all the selection criteria in the data and the background estimation. Exclusion contours in the $m_0 - m_{1/2}$ plane as well as in the plane of the masses of supersymmetric particles are also discussed in this chapter. Finally, in Chapter 6 the results are summarised and future directions are indicated.

Chapter 2

The Tevatron and the DØ Detector

The data collected with the DØ detector [35, 36] located at one of the two luminous points of the Tevatron [37–41] collider at the Fermi National Accelerator Laboratory is used to search for SUSY signals in the present work. This chapter describes the Tevatron collider briefly as well as the technical details of the DØ detector with emphasis on calorimetry and tracking.

2.1 The Accelerator

The proton-antiproton collider at Fermi National Accelerator Laboratory is presently the world's highest energy accelerator with a center of mass energy of 1.8 TeV. A schematic view of the accelerator complex is shown in the Fig. 2.1. The beams originate in the preaccelerator as H^- ions and are accelerated to 750 KeV by an electrostatic Cockroft-Walton generator. The ions are bunched and transported to the Linac, a 150 m long linear accelerator. The ions attain an energy of 200 MeV in the Linac. Then they are passed through a carbon foil where the electrons are stripped off producing protons. The protons are then injected into the Booster, a 151 m diameter synchrotron. The Booster operates at a frequency of 15 Hz and increases the energy of the protons to 8 GeV. The protons are then injected into the Main Ring, a large (1 km radius) synchrotron composed of about 1000 conventional copper-coiled magnets. Protons in the main ring are accelerated either to 120 GeV and used for making antiprotons, or to 150 GeV and injected into the Tevatron.

While collisions occur in the Tevatron, the Main Ring runs to produce antiprotons [39].

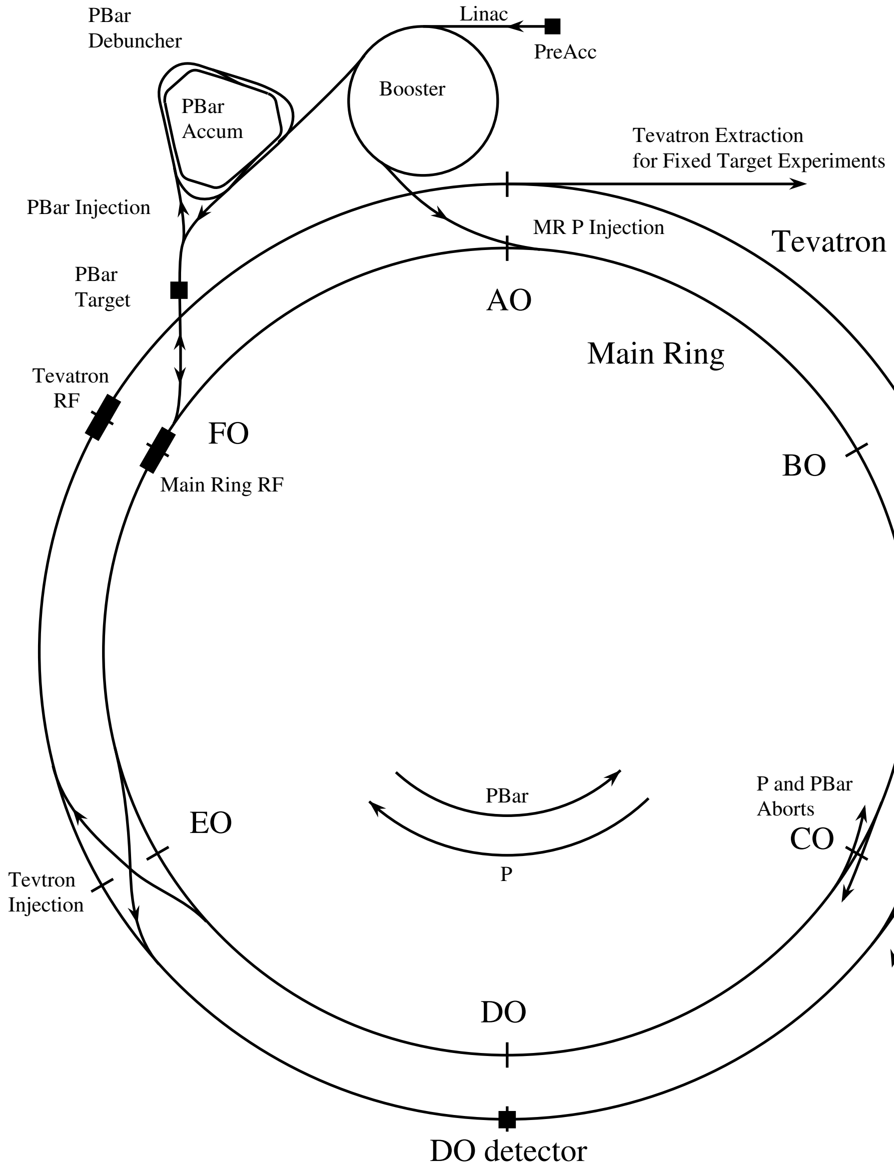

Figure 2.1: Schematic diagram of the Fermilab accelerator complex.

Protons are accelerated to 120 GeV and extracted onto a nickel target, and the resulting antiprotons are selected from accompanying debris by a series of magnets. These antiprotons are cooled in the Debuncher ring and stored in the Accumulator. Operation cycle time of the antiproton source is 2.4 seconds.

The Tevatron is a proton synchrotron using superconducting magnets [38, 40] which operate at a temperature of liquid helium (4.6^o K) and produce fields of $\sim$ 3 Tesla. It is located in the same tunnel as the Main Ring and is separated vertically by 1 m, except at the B0 (CDF) and the DØ detector areas where the separations are 5.8 metres and 2.3 metres respectively. In the final phase, six bunches of protons ($\sim 10^{11}$ particles/bunch) and six bunches of antiprotons ($\sim 5 \times 10^{10}$ particles/bunch) are accelerated to an energy of 900 GeV. Once this energy is attained (called the flattop), the beams are focussed and made to collide at the CDF and DØ experimental areas. Everywhere else the beams are kept apart by electrostatic separators. The luminosity is increased by focussing the beams. The beam spot has a spread of $\sigma_{x,y} \approx 40\mu m$ and $\sigma_z \approx 30$ cm. The useful lifetime of the beams is in the range of 12-20 hours, after which the Tevatron ring is emptied and refilled. Typical down-time is about 2 hours.

During the 1993-95 run (Run 1B), the integrated luminosity recorded at DØ was ~ 100 pb^{-1} with the peak instantaneous luminosity of 3×10^{31} particles per cm^2 per second.

2.2 The DØ Coordinate System

Before describing the DØ detector it is useful to define the coordinate system and angle convention used in the experiment. In DØ a right handed coordinate system is used, with the direction of the proton beam as the positive $z-$axis and the y axis pointing up. The angular coordinates are defined such that $\phi = 0$ coincides with the $+x$ direction and $\theta = 0$ with the $+z$ direction. In place of θ it is convenient to use the *pseudorapidity* η defined as

$$\eta = -ln\ tan\frac{\theta}{2} \tag{2.1}$$

The pseudorapidity approximates the true rapidity,

$$y = \frac{1}{2}ln\frac{E + p_z}{E - p_z} \tag{2.2}$$

in the limit $m/E \to 0$ where m is the rest mass of the particle.

In $p\bar{p}$ collider, many products of the collision escape detection by going down the beam pipe, thus making the measurement of momentum or energy of the colliding partons impossible. However, as their transverse momenta (p_T) are negligible, one can apply conservation of momentum and energy in the transverse plane. The transverse energy, E_T ($= E sin\theta$) and $\not{E}_T$, the missing transverse energy, are two quantities used extensively in the analyses of collider data.

2.3 The DØ Detector

The DØ experiment uses a large multipurpose detector to study $p\bar{p}$ collisions at $\sqrt{s}$ = 1.8 TeV. It has been operating since 1992. The prime physics focus is the study of phenomena involving high p_T and high mass states as in the search for the top quark, precision study of the W and Z bosons or search for heavy exotic particles like supersymmetric particles. The main emphasis was on excellent identification of electrons and muons and a good measurement of their energy; good measurement of the energy and direction of parton jets and the determination of missing transverse energy.

Detectors for colliding beam experiments generally consist of three main elements: the tracking chamber, the calorimeter and the muon system. Surrounding the beam pipe are the *tracking* detectors, which can measure the three-dimensional trajectories of charged particles passing through them. Often, the tracking detectors are placed in a magnetic field enabling the determination of the momenta of the charged particles via the measurement of their deflection. Surrounding the tracking detectors is typically a *calorimeter* to measure the energy of the particles. A calorimeter should be thick enough to absorb all the energy of the incident particles; the tracking chamber should contain very little material to minimize multiple scattering and loss of energy of the particles before they enter the calorimeter. Muons are identified by the tracking chambers outside the calorimeter. Any charged particle originating from the interaction point and penetrating the calorimeter is probably a muon. Neutrinos, being neutral and weakly interacting can only be inferred from the imbalance of the overall transverse energy in the event.

The DØ detector (Fig. 2.2) follows the general philosophy of a collider detector described above. The detector design was optimised for a compact, hermetic calorimeter with high resolution for the measurement of the energies of electrons and jets. As a consequence

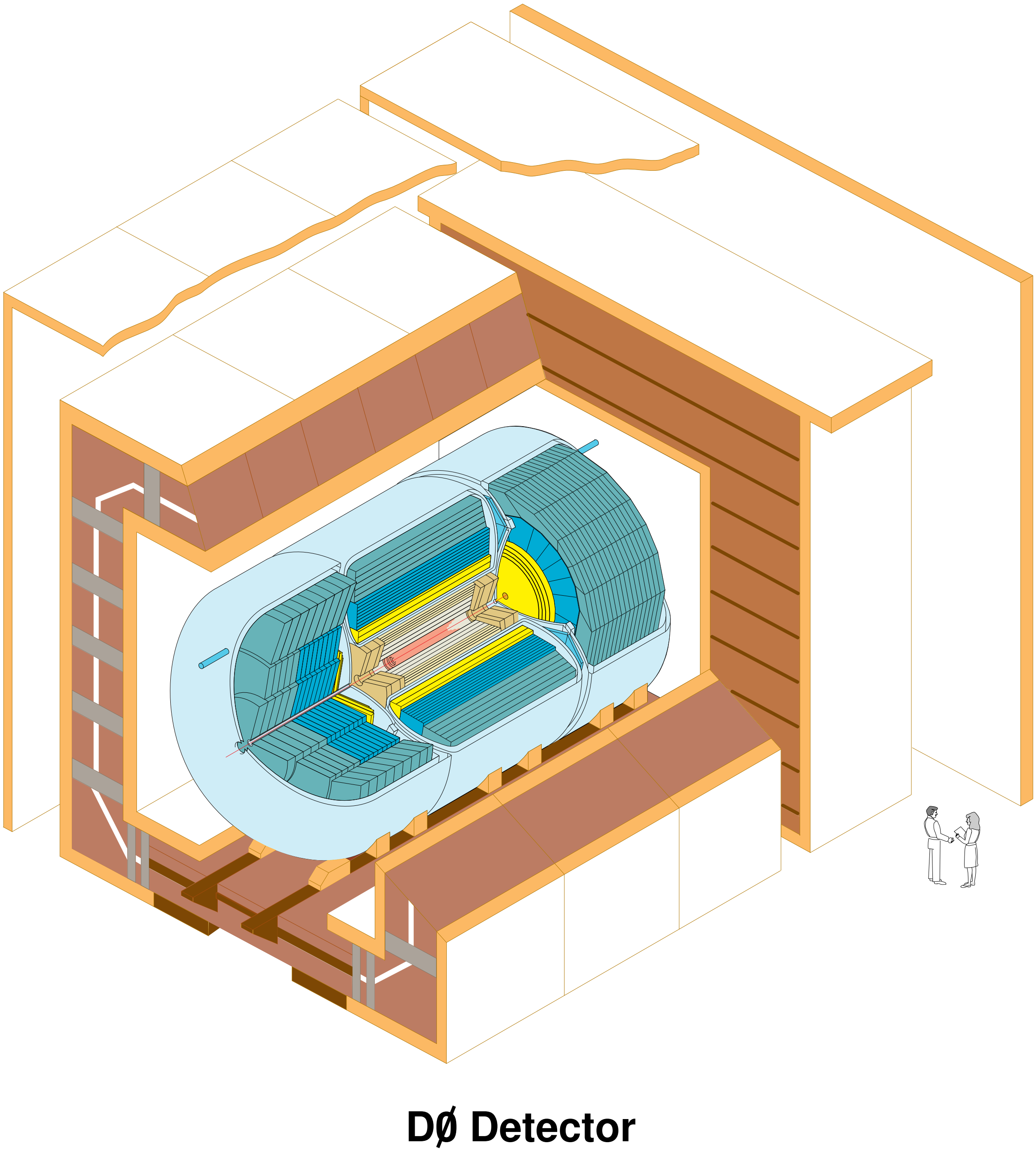

Figure 2.2: Cutaway view of the DØ detector

the tracking detector is relatively small and there is no central magnetic field. As the momentum resolution in the magnetic tracker is roughly proportional to the momentum, whereas the energy resolution in the calorimeter varies as $1/\sqrt{E}$, for high p_T objects a better momentum resolution can be achieved with the calorimeter than with a tracking chamber. Moreover, the presence of magnetic field degrades the energy resolution of the calorimeter by: 1) sweeping low energy charged particles away from the jet and 2) adding additional material (due to the solenoid) prior to the calorimeter. Very good calorimetry in DØ is achieved by using a liquid argon sampling calorimeter made primarily from depleted uranium (in some places copper and steel absorbers are also used). Muons are identified by tracking chambers outside the calorimeter. Muon momenta are measured from the bending of their trajectory in the iron toroidal magnet placed between the first two layers of the tracking chamber.

The detector measures 13 m (height) $\times$ 11 m (width) $\times$ 17 m (length) and weighs 5500 tons. The entire assembly rests on a detector platform which is mounted on rollers so that the entire detector may be rolled from the assembly area to the collision hall. The platform also provides space for detector electronics and other utilities (such as gas, power, cryogenics, cable utilities). The analog signals are read via cables from the detector platform to the Moving Counting House (MCH). The MCH is a three-storey enclosure housing the Level-0 and Level-1 trigger electronics, high voltage power supplies, and digitization electronics for all detector parts. The cables are then led out of the MCH into the assembly building where software trigger, online systems and the control room are located.

Some of the individual elements of the DØ detector are described below.

2.4 Central Detector

The DØ tracking detector is also called the central detector (CD). As shown in Fig. 2.3, it has 4 separate systems: (i) the vertex drift chamber (VTX), (ii) the transition radiation detector (TRD), (iii) the central drift chamber (CDC) and (iv) two forward drift chambers (FDC). The whole of CD fits within the inner cylindrical aperture of the calorimeters within a volume bounded by $r = 78$ cm and $z = \pm 135$ cm. The CD is used for the reconstruction of the three-dimensional trajectories of charged particles which pass through them and for a precise measurement of the locations of the interaction vertices of each event. The major emphasis is placed on good two-track resolving power, high efficiency and good ionisation measurement to distinguish between electrons and closely spaced conversion pairs ($\gamma \rightarrow e^+e^-$). Precise position measurements are useful for calibrating the position measurements obtained from calorimeter response and for improving the accuracy of muon momentum measurements. The following sections describe details of the CD subdetectors and the basics of drift chamber operation which is used extensively in the central detectors.

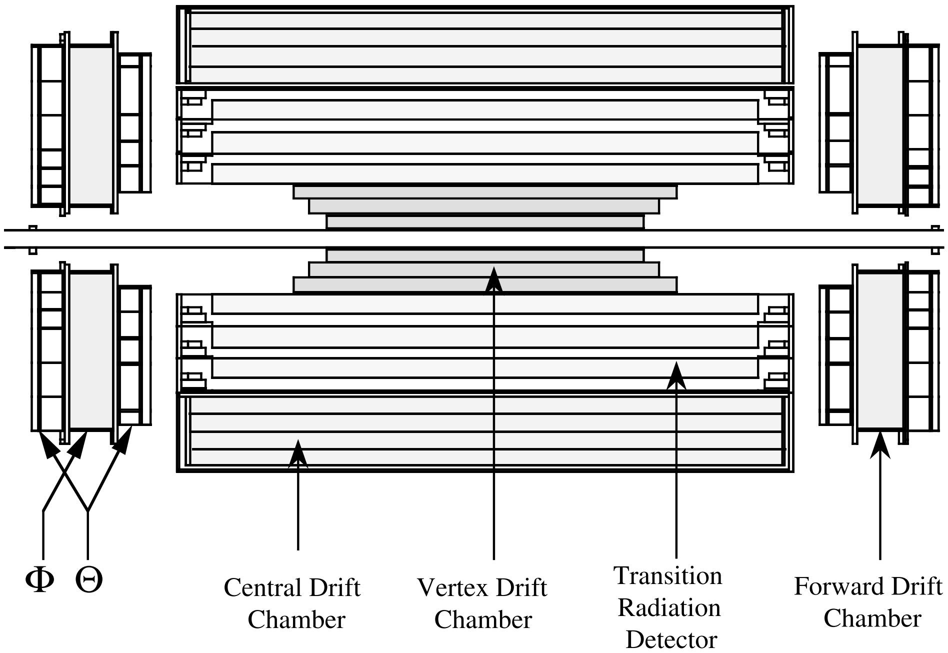

Figure 2.3: Side view of the DØ central detector.

2.4.1 Principles of Operation of Proportional Drift Chamber

A fast charged particle passing through a gaseous medium interacts mainly through Coulomb interaction with the nearby atomic electrons. This results in the creation of electron-ion pairs in the medium. The number of such pairs depend on the energy of the particle and the type of gas. For high energy particles (also called the minimum ionising particles) the number of pairs created does not vary with energy. For such minimum ionising particles and for a typical gas, at NTP the average number of electron-ion pairs created is $\sim\ 100/cm$. This is called primary ionisation and is too weak to give a measurable signal.

When an electric field is applied across the gas volume, the electrons drifts towards the anode. In a proportional drift chamber the anode is a thin wire so that the electric field all over the gas region is low and constant but in its vicinity it is very high ($\sim 10^4 - 10^5\ V/cm$). In such an electric field the electron travels from the position of its creation to very close to the anode wire at a constant velocity and without creating any more electron-ion pairs. But when it reaches close to the anode wire, due to the high electric field it acquires enough energy to knock out electrons from the molecules in the gas, upon collision. These additional electrons ionise more gas molecules; in this way an avalanche is formed and the number of electron-ion pair increases exponentially. This is called secondary ionisation and it gives rise to a measurable signal. The time electron takes to reach the anode wire can be converted easily into the position of its creation as the electron drifts with a known speed over most of the distance. For a good linear relationship between the distance and the drift time the electric field needs to be uniform over a large volume. This can be achieved by putting additional field shaping wires between cathode and anode.
A more detailed discussion on the drift chambers can be found in [45, 49, 50].

2.4.2 Vertex Chamber

The Vertex Chamber (VTX) [46–48] is the innermost tracking detector covering a pseudorapidity range $|\eta| \leq 2.0$. It can be used to precisely determine the position of the event vertex and is composed of three concentric cylindrical layers occupying the region 3.7 cm $< r <$ 16.2 cm. The inner layer has a length of 97 cm, with each successive layer being about 10 cm longer. A cross sectional view of the VTX chamber is shown in Fig. 2.4.

The innermost layer has 16 cells in azimuth whereas the outer two layers have 32 cells each. In each cell, eight 25 μm thick sense wires provide measurement of the $r-\phi$ coordinate. Adjacent sense wires are staggered by $\pm 100\ \mu m$ to resolve the left-right ambiguities; the cells of the three layers are offset in ϕ to further aid the pattern recognition. The $r-\phi$ coordinate of a hit is obtained from the drift time and the wire hit, while the z position is measured using a charge division method. The $r\phi$ and z resolutions are 60 μm and 1.5

cm respectively.

Additional details of the VTX are given in Table 2.1.

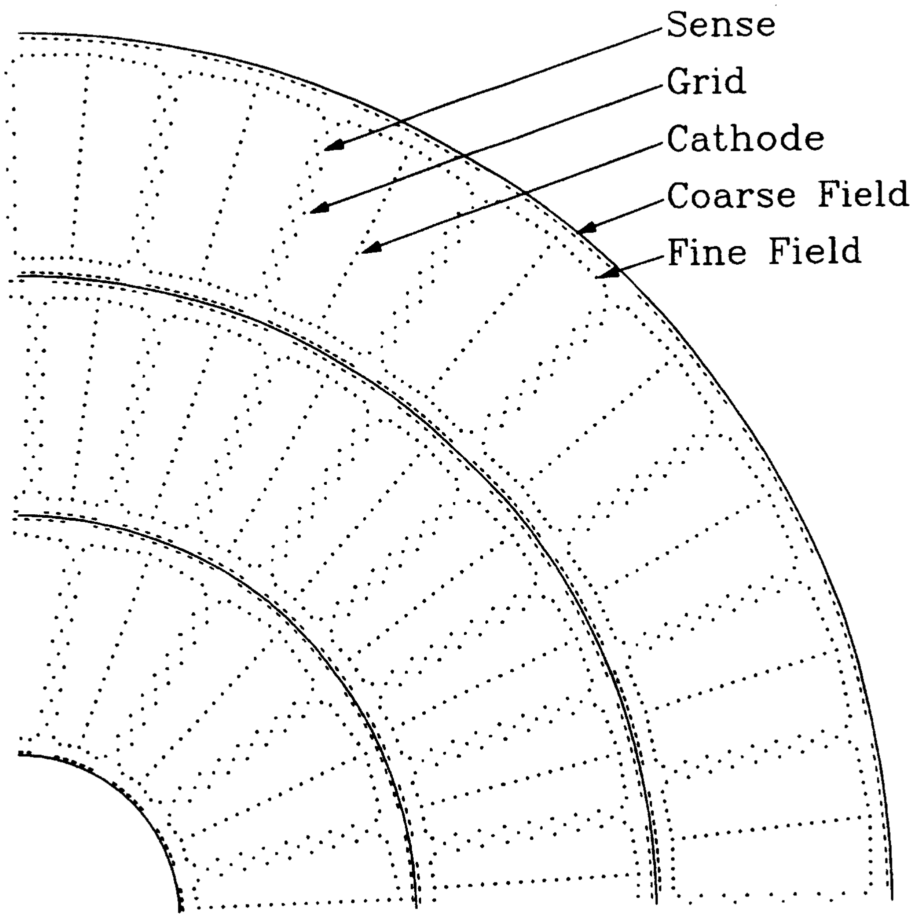

Figure 2.4: $r - \phi$ view of a quadrant of the VTX chamber.

2.4.3 Transition Radiation Detector

When a charged particle traverses a medium with varying dielectric constants, e.g. alternate layers of foils and air gaps, it radiates in the forward direction [49, 50]. For a relativistic particle with time dilation factor $\gamma = E/mc^2$, the radiation is concentrated in a cone with opening angle $1/\gamma$ and the intensity of radiation is proportional to γ.

The DØ transition radiation detector (TRD) [51, 52] is a device designed to distinguish

Number of layers	3
Active Radius (cm)	3.7 - 16.2
Active length of each layer (cm)	96.6, 106.6, 116.8
Number of sense wires	8 per cell, 640 total
Sense wire separation	4.57 mm radially with 100 μm stagger
Sense wire specifications	25 μm NiCoTin, 80 g tension
Sense wire Voltage	+2.5 kV
Gas	95% CO_2, 5% Ethane, 0.5 H_2O%
Drift Velocity	7.3 $\mu m/ns$
Drift field	1 kV/cm
Max. drift distance	1.6 cm
Gas Gain	4×10^4
$r - \phi$ resolution	$\sim$ 60 μm
Z resolution	$\sim$ 1.5 cm
Two hit resolution	90% eff. at 0.63 mm separation

Table 2.1: Vertex Chamber Parameters.

electrons from heavier particles. It envelopes the VTX and consists of three radial layers as shown in Fig. 2.3. The radiator section of each TRD unit has 393 foils of 18 μm thick polypropylene with a mean separation of 150 μm. The gaps between the foils are filled with dry nitrogen. An ultra relativistic particle traversing the layers of foil-gas emits radiation in the X-ray region with an energy peaking around 8 KeV and these are detected by xenon-filled drift chambers.

2.4.4 Central Drift Chamber

The central drift chamber (CDC)[47, 53–55] is the outermost tracking detector covering pseudorapidity range of $|\eta| < 1.2$. It consists of four layers of cells with length of 184 cm and radii between 49.5 cm and 74.5 cm. Fig. 2.5 shows an end view of the CDC.

Each layer has 32 identical modules. Within each cell, there are 7 sense wires, staggered by 200 μm relative to each other for resolving left-right ambiguities. Alternate cells along the radial direction are offset by one half cell to further aid the pattern recognition. The $r\phi$ position of a hit is determined via the drift time and the wire hit. For the determination of the z position delay lines are embedded in the inner and outer shelves of each cell. When an avalanche occurs near an outer sense wire, a pulse is induced in the nearby

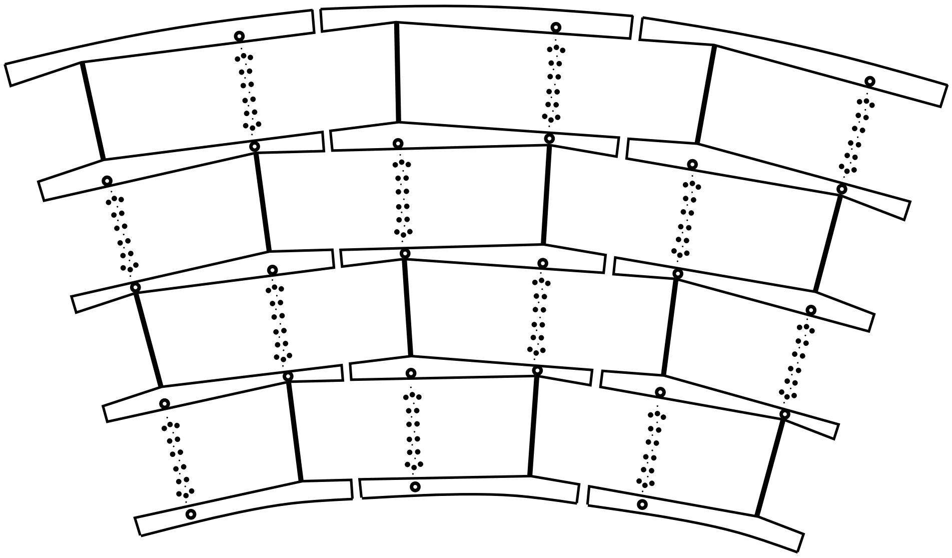

Figure 2.5: End view of three out of 32 segments of the CDC.

delay line. By comparing the arrival times of the pulse at both ends, the z position can be determined. A summary of CDC parameters is given in Table 2.2.

2.4.5 Forward Drift Chamber

The forward drift chambers (FDC)[47, 53, 56, 57] extend the coverage of charged particle tracking down to $\theta = 5^0$ ($|\eta| < 3.1$). There are two packages of FDC's on either side of the CDC. Each FDC consists of three separate modules, a Φ module sandwiched between two Θ modules. In the Φ module sense wires are radial and measure the ϕ coordinate, while in the Θ modules the sense wires approximately measure the θ coordinate. Fig. 2.6 shows the sense wire orientations for each of these modules. Each Θ module has four mechanically separated quadrants, each containing six rectangular cells at increasing radii. Each cell contains eight sense wires in z; the sense wires in the three inner cells are placed at the edge of the cell so that the electrons can drift only in one direction. Each Θ cell also contains a delay line to measure the coordinate along the wire. The two Θ chambers are rotated relative to each other by $\pi/4$. The Φ chamber is divided into 36 azimuthal drift cells, each containing 16 radial sense wires. All adjacent sense wires of both Θ and Φ

Number of layers	4
Active Radius (cm)	51.8 - 71.9
Active length of each layer (cm)	179.4
Number of sense wires	7 per cell, 896 total
Sense wire separation	6.0 mm radially with 200 μm stagger
Sense wire specifications	30 μm Au plated W, 110 g tension
Sense wire Voltage	+1.45 kV (inner SW), +1.58 kV (outer SW)
Number of delay lines	2/cell, 256 total
Delay line velocity	2.35 mm/ns
Gas	93% Ar, 4% Methane, 3% CO_2, 0.5 H_2O%
Drift Velocity	34 $\mu m/ns$
Drift field	620 V/cm
Max. drift distance	7 cm
Gas Gain	2×10^4 (inner SW) - 6×10^4 (outer SW)
$r - \phi$ resolution	$\sim 150 - 250$ μm
Z resolution	~ 2.0 cm
Two hit Resolution	90% eff. at 2 mm separation

Table 2.2: Central Drift Chamber Parameters

modules are staggered by $\pm 200 \mu m$ to resolve ambiguity.

A summary of FDC parameters is shown in Table 2.3.

2.4.6 Central Detector Readout

The electronics for reading out signals from different CD devices are similar. Signals from the chambers are fed into preamplifiers mounted directly on the chambers themselves. From there signals are sent to analog pulse shaping cards located on the platform underneath the detector. Finally the signals go to the flash ADC digitizers located in the MCH. If the event is accepted by the level-1 trigger, the data are zero suppressed and sent to the level-2 trigger.

2.5 Calorimeter

Conceptually, a calorimeter is a block of matter of sufficient thickness which can cause the primary particle incident on it to interact and deposit all its energy. In DØ, the calorimeter is used to measure the energy of most particles (except muon and neutrino)

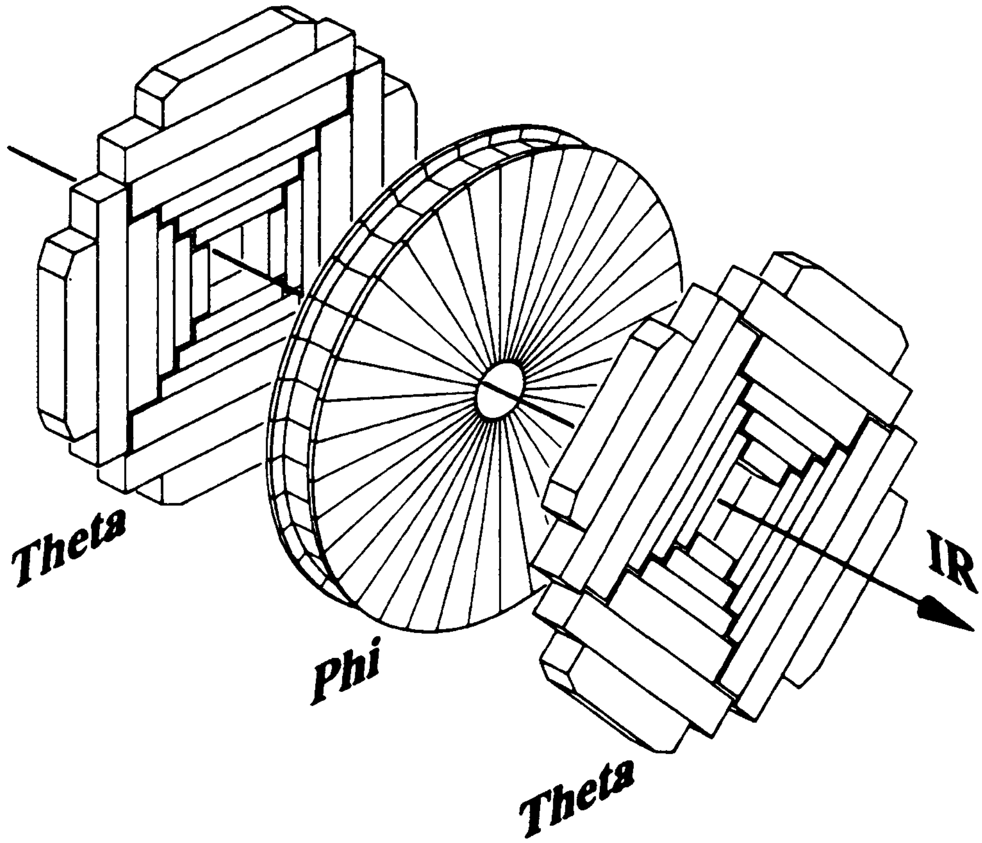

Figure 2.6: The Forward Drift Chambers.

	Θ Modules	Φ Modules
Active radius	11 cm - 62 cm	11 cm - 61.3 cm
Z extent	104.8 cm - 111.2 cm 128.8 cm - 135.2 cm	113.0 cm - 127.0 cm
Number of cells / layer	4 quadrants of 6 cells	36
Number of Sense wires	8 per cell, 384/FDC	16/cell, 576 total
Sense wire separation	8 mm radially with 200 μm stagger	
Sense wire specifications	30 μm Au-plated W, 50-100 g tension	
Sense wire voltage	+ 1.55 kV	+1.66 kV
Number of delay lines	1 / cell, 48/FDC	None
Delay line velocity	2.35 mm/ns	-
Gas	93 % Ar, 4% CH_4, 3% CO_2, 0.5% H_2O	
Drift velocity	40 μm/ns	37 μm/ns
Drift field	1 kV/cm	1 kV/cm
Maximum drift distance	5.3 cm	5.3 cm
Gas gain	2.3×10^4 (inner SW) 5.3×10^4 (outer SW)	3.6×10^4
$r - \phi$ resolution	200 μm	
z resolution	2 mm	
two hit resolution	90% eff. at 2 mm separation	

Table 2.3: Forward Drift Chamber Parameters

that are incident on it. The calorimeter design was crucial for the optimization of the DØ detector. Since there is no central magnetic field, calorimetry is the only available method for the measurement of the energy of electrons, photons and jets. In addition, the calorimeters play an important role in the identification of electrons, photons, jets and muons, and in establishing the transverse energy imbalance in an event. A detailed discussion of Calorimetry can be found elsewhere[49, 58, 59].

2.5.1 Calorimetry principle

When a high energy electron ($\gg$ 10 MeV) traverses through matter of high atomic number it losses its energy primarily through Bremsstrahlung. Similarly, for a high energy photon the energy loss is predominantly via the electron-positron pair production in the vicinity of the nucleus. The electrons and positrons created through pair production can in turn lose energy through Bremsstrahlung. This process continues until the energy of the secondary particles fall below a critical energy level where the other energy loss mechanisms (like ionisation) become important. This is called an *electromagnetic shower*. Since, at high energies, the angle of emission of electrons-positrons or photons is small, the shower develops primarily in the direction of the original electron or photon. The energy loss of a particle through electromagnetic interaction can be characterised by *radiation length* X_0:

$$\frac{dE}{E} = -\frac{dx}{X_0} \tag{2.3}$$

The radiation length is dependent on the absorbing medium, e.g, in case of Uranium it is 3.2 mm.

Hadrons lose energy primarily through inelastic collision with the atomic nuclei. Secondary hadrons produced in these collisions can in turn undergo inelastic collisions. This process is called *hadronic shower*, and it continues until particles are stopped by either ionisation losses or absorbed by nuclear processes. Typical hadron production occurs with a mean transverse momentum $\sim$ 350 MeV/c. Thus, hadronic showers tend to be more spread out laterally than electromagnetic showers. The size of hadronic showers is usually measured in terms of the nuclear interaction (absorption) length λ and it depends on the medium. For uranium, $\lambda \approx 10.5$ cm.

Calorimeters can be classified as i) *homogeneous* and ii) *sampling* types. In a homogeneous calorimeter, absorbers act as active materials too. Although homogeneous calorimeters achieve better resolutions, quite often they are not practical for large, high-energy detectors. In sampling calorimeter, absorber layers are interspersed with layers of active materials. One desirable aspect of calorimetry is compensation. As in every hadronic shower there will be a significant component of electromagnetic energy deposition, it is desirable that the responses of the calorimeter to both electrons and hadrons are as close as possible. It is measured by a quantity called *e/π ratio* which should be close to unity in compensating calorimeters.

Even if a calorimeter is perfectly compensating, there are many additional effects which tend to degrade the energy resolution. Since the showering and sampling processes are statistical in nature the resolution depends on $1/\sqrt{N}$, where N is the number of ionising electrons liberated and this is directly proportional to the energy of the incident particle. So the energy resolution scales as $1/\sqrt{E}$. Additional sources of energy fluctuations in the calorimeter are:

- Energy leakage out of the calorimeter.

- Electronic noise.
- Variation in the high voltage, absorber thickness etc.

The calorimeter can also be used to measure the positions of incident particles by studying the transverse profile of the shower and calculating its centre of gravity.

2.5.2 Calorimeter Design

The DØ calorimeter has liquid argon as the active medium to sample the ionisation produced in electromagnetic or hadronic showers. The primary absorber material is depleted uranium but in the outer layers stainless steel and copper are also used. Due to the high density of uranium the calorimeter is compact. The choice of liquid argon is supported by the unit gain, relative simplicity of calibration, flexibility in segmenting the calorimeter into longitudinal and transverse cells, good radiation hardness and low unit cost of electronics and readout system. But the disadvantage is that it needs a cryogenic system for liquid argon. The massive containment vessel for the cryogenic system leaves regions of uninstrumented material and the calorimeter modules are inaccessible during operation. To make provision for some degree of access to the central tracking detectors within the calorimeter cavity, more than one containment vessel is necessary. The design chosen is shown schematically in Fig. 2.7. The central calorimeter (CC) covers roughly $|\eta| \leq 1$ and two end calorimeters (EC) extend the coverage up to the region $|\eta| \approx 4$. The Inter-cryostat Detector (ICD) covers the overlapping region. The boundary between CC and EC is approximately perpendicular to the beam direction. This choice is shown to give good $\not{E}_T$ resolution.

The calorimeter is modular and is finely segmented in the transverse and longitudinal directions of the shower. Three distinct types of modules are used in CC as well as in EC. An electromagnetic section with thinner absorber plates and fine segmentation, a fine hadronic section (FH) with thicker absorber plates than EM section and coarse hadronic section (CH) with thick copper and stainless steel plates are used in the DØ calorimeter. Each module consists of a stack of interleaved absorber plates and signal boards as shown in the Fig. 2.8. The absorber plates are separated from signal boards by a liquid argon gap of 2.3 mm. Signal boards are constructed by laminating a copper pad with two 0.5 mm thick pieces of G10. Outer surface of these boards are coated with resistive epoxy. Electric field is applied by grounding the metal absorber plate and connecting the resistive

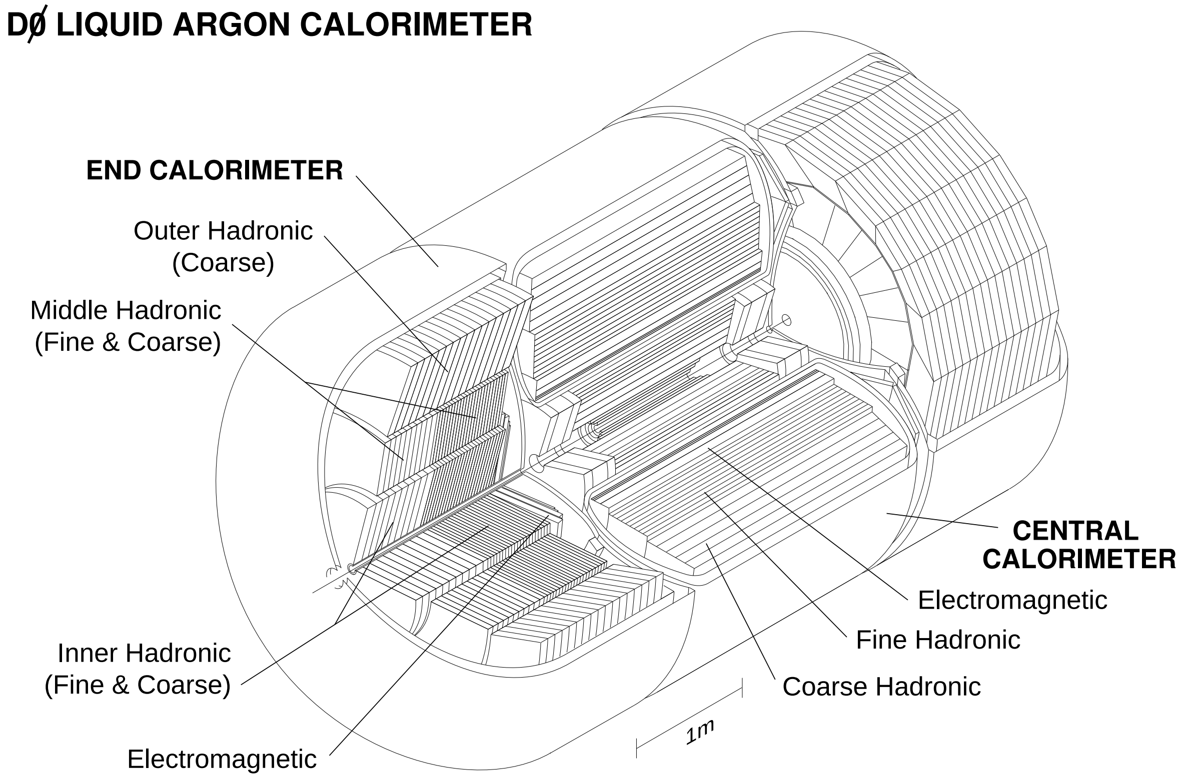

Figure 2.7: Isometric view of the DØ calorimeter showing the central and two end calorimeters.

surface of the signal boards to a positive high voltage of typical value 2.0-2.5 kV. The electron drift time across the gap is $\approx 450ns$. Signals from several pads at approximately the same η and ϕ are ganged together in depth to form a *readout cell* ; the details of these gangings vary from cell to cell. The pattern and sizes of readout cells were determined from considerations of shower shape. The transverse sizes of the cells were chosen to be comparable to the transverse sizes of showers: $\sim 1-2$ cm for EM showers and ~ 10 cm for hadronic showers. Longitudinal segmentation within EM, fine hadronic and coarse hadronic sections are useful for distinguishing between electrons and hadrons. The final design was chosen to have *pseudo-projective* readout towers with each tower subdivided in depth. Pseudo-projective means that the centres of cells of increasing shower depth lie on a straight line emanating from the centre of the interaction region, but the cells boundaries are aligned perpendicular to the absorber plates. Fig. 2.9 shows the segmentation for a portion of the DØ calorimeter.

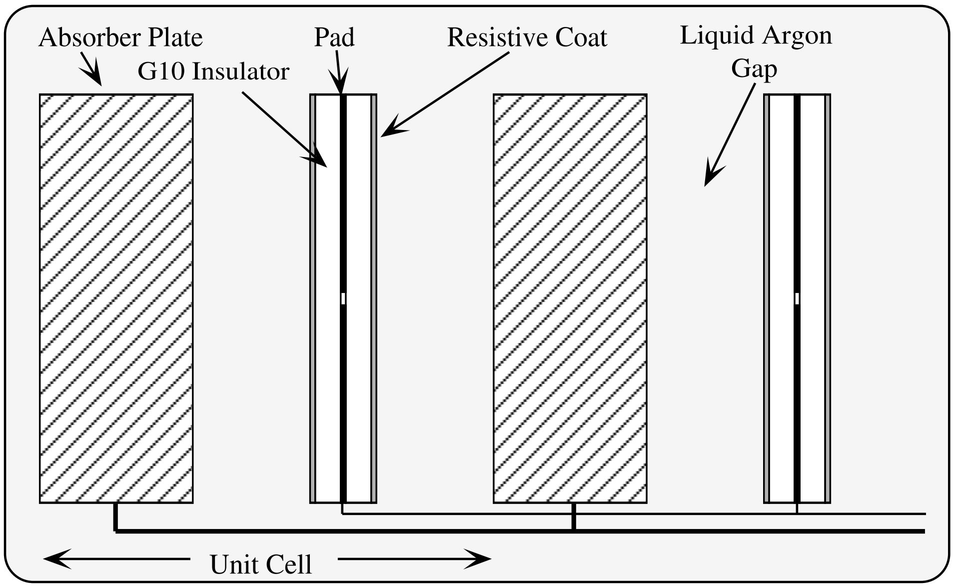

Figure 2.8: A schematic view of a calorimeter cell.

2.5.3 Central Calorimeter

The central calorimeter consists of three concentric cylindrical layers of modules. It is 226 cm long and radially it occupies the space 75 cm$< r <$ 222 cm and covers up to $|\eta| < 1.2$. There are 32 electromagnetic, 16 fine hadronic and 16 coarse hadronic modules in it. The transverse segmentation is 0.1×0.1 in $\eta \times \phi$ space except in the third layer of the EM module where EM shower maximum is expected; the latter has a segmentation of 0.05×0.05 in $\eta \times \phi$ space. The EM, FH and CH module boundaries are rotated to avoid continuous inter module crack. The major design specifications are listed in Table 2.4.

2.5.4 End Calorimeters

The end calorimeter provides coverage in the range $1.1 < |\eta| < 4.5$. Each EC cryostat is divided into four sections : the electromagnetic (EM), the inner hadronic (IH), the middle hadronic (MH) and the outer hadronic (OH) calorimeter.

The ECEM module contains four readout sections with outer radii varying between 84 and 104 cm and inner radii 5.7 cm. The transverse segmentation is mostly 0.1×0.1 in

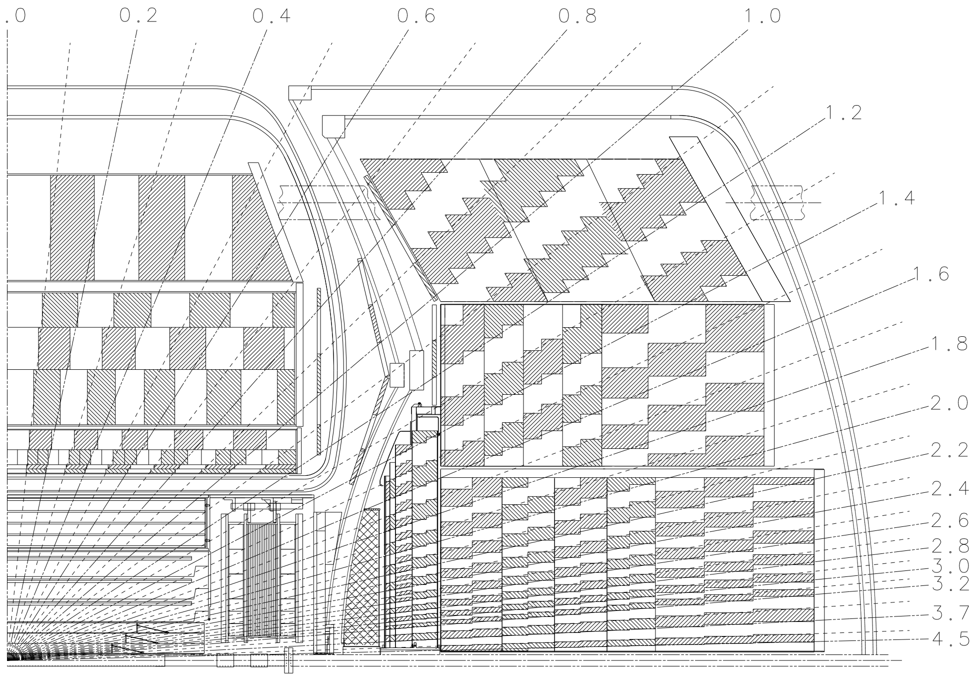

Figure 2.9: Side view of the calorimeter showing the segmentation and pseudo-projective tower geometry.

$\eta \times \phi$ space, but for $|\eta| > 3.2$ the segmentation is increased to 0.2×0.2. As in the CC, here also the third EM layer has finer segmentation with 0.05×0.05 for $|\eta| < 2.7$, 0.1×0.1 for $2.7 < |\eta| < 3.2$ and 0.2×0.2 for $|\eta| > 3.2$.

The IH modules are cylindrical with inner and outer radii of 3.92 cm and 86.4 cm respectively. Longitudinally, IH is divided into fine hadronic and coarse hadronic sections. Stainless steel is used as absorbing material in the coarse section. The transverse segmentation of IH is $\Delta\eta \times \Delta\phi = 0.1 \times 0.1$ for $|\eta| < 3.2$, 0.2×0.2 for $3.2 < |\eta| < 3.8$ and 0.4×0.2 for $|\eta| > 3.8$. Surrounding the IH is the middle hadronic module, it also has fine hadronic and coarse hadronic parts; here also stainless steel absorbers are used in the coarse hadronic sections. The transverse segmentation of MH is similar to that of IH. The OH module has only coarse hadronic section. The inner and outer radii of OH

Module Type	EM	FH	CH
η coverage	$\pm$ 1.2	$\pm$1.0	$\pm$0.6
# of modules	32	16	16
Absorber	U	UNb	Cu
Thickness (mm)	3	6	46.5
Liquid argon gap	2.3 mm	2.3 mm	2.3 mm
# of readout layers	4	3	1
# of cells / readout layer	2,2,7,10	20,16,14	9
Layer thickness	2.0, 2.0, 6.8, 9.8 X_0	1.3, 1.0, 1.9 λ	3.2 λ
Total radiation length	20.5	96.0	32.9
Total Absorption length	0.76	3.2	3.2
Sampling Fraction (%)	11.79	6.79	1.45
Total readout cells	10368	3000	1224

Table 2.4: Central Calorimeter Parameters

module are 162 cm and 226 cm respectively. The major design specifications of the End Cap calorimeter are listed in Table 2.5.

2.5.5 Inter Cryostat and Massless Gap Detectors

There is a big uninstrumented area in the transition region between the CC and the EC ($0.8 < |\eta| < 1.5$) where the amount of energy deposited is not sampled. Therefore, two detector elements have been added i.e., Intercryostat Detector (ICD) and Massless Gap (MG) detectors. The ICD is a set of scintillator detectors mounted on the surface of the EC cryostat with a typical segmentation of 0.1×0.1 in $\eta \times \phi$. The massless gap detectors are single-cell structures mounted on the end plates of the CCFH, ECMH and ECOH modules.

2.5.6 Calorimeter Readout

Signals from the calorimeter modules are first brought out of the four feedthrough ports to the charge sensitive preamplifiers mounted on top of the cryostats. Output signals from preamplifiers are transported to baseline subtracters (BLS) where analog shaping and splitting of the pulse into two paths is done. The first is used for trigger. The signals

Module Type	EM	IFH	ICH	MFH	MCH	OH
η coverage	1.3-3.7	1.6-4.5	2.0-4.5	1.0-1.7	1.3-1.9	0.7-1.4
# of modules	1	1	1	16	16	16
Absorber plates	U	UNb	SS	UNb	SS	SS
Absorber Thickness (mm)	4	6	6	6	46.5	46.5
Liquid argon gap (mm)	2.3	2.1	2.1	2.2	2.2	2.2
# of readout layers	4	4	1	4	1	3
# of cells / readout layer	2,2,6,8	16	14	15	12	8
Layer thickness	.3 ,2.6, 7.9, 9.3 X_0	1.2 λ each	3.6 λ	1.0 λ each	4.1 λ	7.0 λ
Total X_0	20.5	121.8	32.8	115.5	37.9	65.1
Total λ	0.95	4.9	3.6	4.0	4.1	7.0
Sampling Fraction (%)	11.9	5.7	1.5	6.7	1.6	1.6
Total readout cells	7488	4288	928	1472	1344	

Table 2.5: End Calorimeter Parameters

from fine hadronic and electromagnetic cells within 0.2×0.2 towers are summed and used as the input of level-1 calorimeter trigger. The second part of the signal is used for data readout. This signal is sampled just before the beam crossing and again 2.2 μs later and the difference between these two samples is a DC voltage proportional to the total charge collected. The difference signal is sent to the ADC where, if the event is accepted by the level-1 trigger, the signals are digitized, zero-suppressed and sent to the level-2 trigger.

2.5.7 Calorimeter Resolutions

The response of the DØ calorimeter modules has been extensively studied with test beams [60–63] and cosmic rays. The response for both single electrons and pions is found to be linear within $\sim 0.5\%$ over the energy range of 10-150 GeV.

The resolution can be parametrised as

$$\left(\frac{\sigma}{E}\right)^2 = C^2 + \frac{S^2}{E} + \frac{N^2}{E^2} \tag{2.4}$$

where the constants C, S, and N represent calibration errors, sampling fluctuations and noise contributions respectively. The noise term is important only at low energy. The measured values of the constants are,

$$C = 0.003 \pm 0.002, \quad S = 0.157 \pm 0.005(GeV)^{1/2}, \quad N \approx 0.140GeV \tag{2.5}$$

for electrons, and

$$C = 0.032 \pm 0.004, \quad S = 0.41 \pm 0.04(GeV)^{1/2}, \quad N \approx 1.28GeV \tag{2.6}$$

for pions.

The position resolution of electrons is about 0.8-1.2 mm and varies approximately as $1/\sqrt{E}$.
The e/π ratio of the calorimeter varies from 1.11 at 10 GeV to 1.04 at 150 GeV giving rise to excellent compensation.

2.6 Muon System

Muons deposit very little energy in the calorimeter and can be identified as those particles which penetrate through it. The DØ muon detection system [64], as shown in the Fig. 2.10, consists of five toroidal magnets together with sets of proportional drift tube chambers (PDTs). The momenta of the muons are determined from their deflection in the toroidal field. The PDT's measure the position of the muon before entering and after exiting the magnetic field. The five magnets are CF covering the region $|\eta| < 1$, the two EFs covering $1 < |\eta| < 2.5$ and two SAMUS (Small Angle MUon system) magnets covering $2.5 < |\eta| < 3.6$. The CF and EFs are together called Wide Angle Muon System (WAMUS); each section has one layer of drift tubes just before the magnet, a second layer just after the magnet and a third layer 1-3 m further out. The minimum momentum needed for a muon to pass through the calorimeter and the toroid varies in the region 3.5-5.0 GeV/c. The momentum resolution is parametrised in terms of the inverse of momentum $k = 1/p$ i.e., as

$$\left(\frac{\delta k}{k}\right)^2 = (0.18)^2 + \left(\frac{0.01}{kGeV}\right)^2 \tag{2.7}$$

A few important parameters of the muon detection system are shown in Table 2.6.

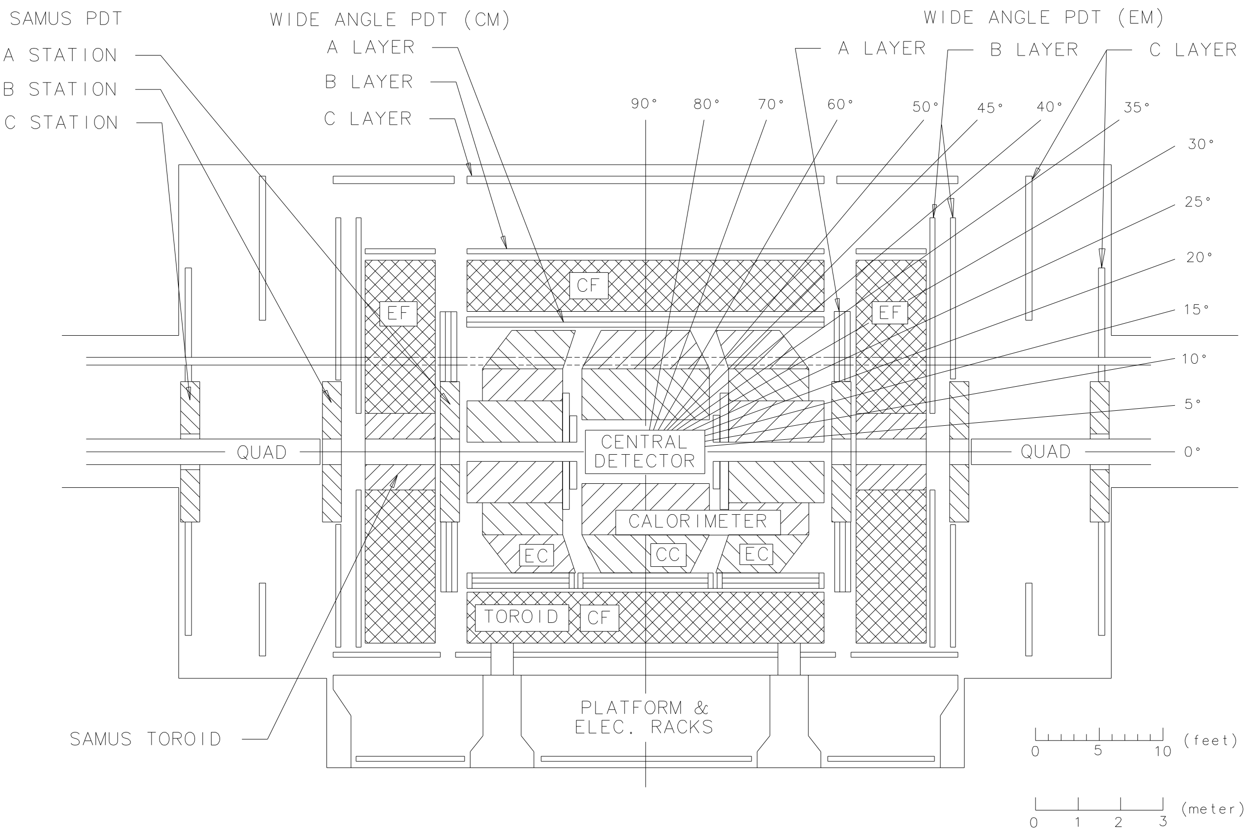

Figure 2.10: Elevation view of the DØ detector showing Muon system.

	Wamus	Samus
η coverage	$\|\eta\| < 1.7$	$1.7 \leq \|\eta\| \leq 3.6$
Magnetic Field	2 T	2 T
Number of modules	164	6
Number of drift cells	11386	5308
Sense wire properties	50 μm Au-plated W, 300 g tension	50 μm Au-plated W 208 g tension
Sense wire voltage	4.56 kV	4.0 kV
Cathode pad material	Glasteel coated Cu strip	No cathode
Cathode pad voltage	2.3 kV	-
Gas	Ar 90%, CF_4 5%, CO_2 5%	CF_4 90%, CH_4 10%
Drift velocity	6.5 cm/μs	9.7 cm/μs
Maximum drift distance	5 cm	1.45 cm
Bend view resolution	$\pm$0.53 mm	$\pm$0.35 mm
Non-bend view resolution	$\pm$0.3 mm	$\pm$0.35 mm

Table 2.6: Muon System Parameters

Chapter 3

Data Acquisition, Reconstruction and Particle Identification

Collisions happen at a very high rate at DØ intersection, but a majority of the events are not interesting for further studies. In this chapter a brief description is given on how the interesting events are selected (*Trigger*) and written in the storage medium (*Data Acquisition System*). In the later part we describe reconstruction of physical objects (such as electrons, jets etc.) from the raw data and corrections that need to be applied to the energy estimates of these objects prior to analysis.

3.1 Trigger and Data Acquisition System

At the Tevatron, during Run I, the bunch crossing rate was 286 kHz; the typical luminosity was $5 \times 10^{30}\ cm^{-2}s^{-1}$ leading to 0.75 interactions per bunch crossing. This amounts to an event rate of about 200 kHz. However, processes of interest are much rarer and it is impractical to record and process data from all the bunch crossings. The technique of selecting interesting events for further processing is called *triggering*. The layout of the DØ trigger system is shown in Fig. 3.1 [36]. It has three different levels with increasingly sophisticated event characterisation. The Level-0 scintillator based trigger selects events occurring due to beam-beam inelastic collisions. Level-1 trigger is based on a collection of programmable hardware processors that can make a decision within the 3.5 μs interval between beam crossings, without incurring any dead time. However, some triggers, referred to as Level-1.5, require more time during which several bunch crossings occur. Level-1 (and Level-1.5) triggers reduce the event rate to $\sim 150 - 200$ Hz.

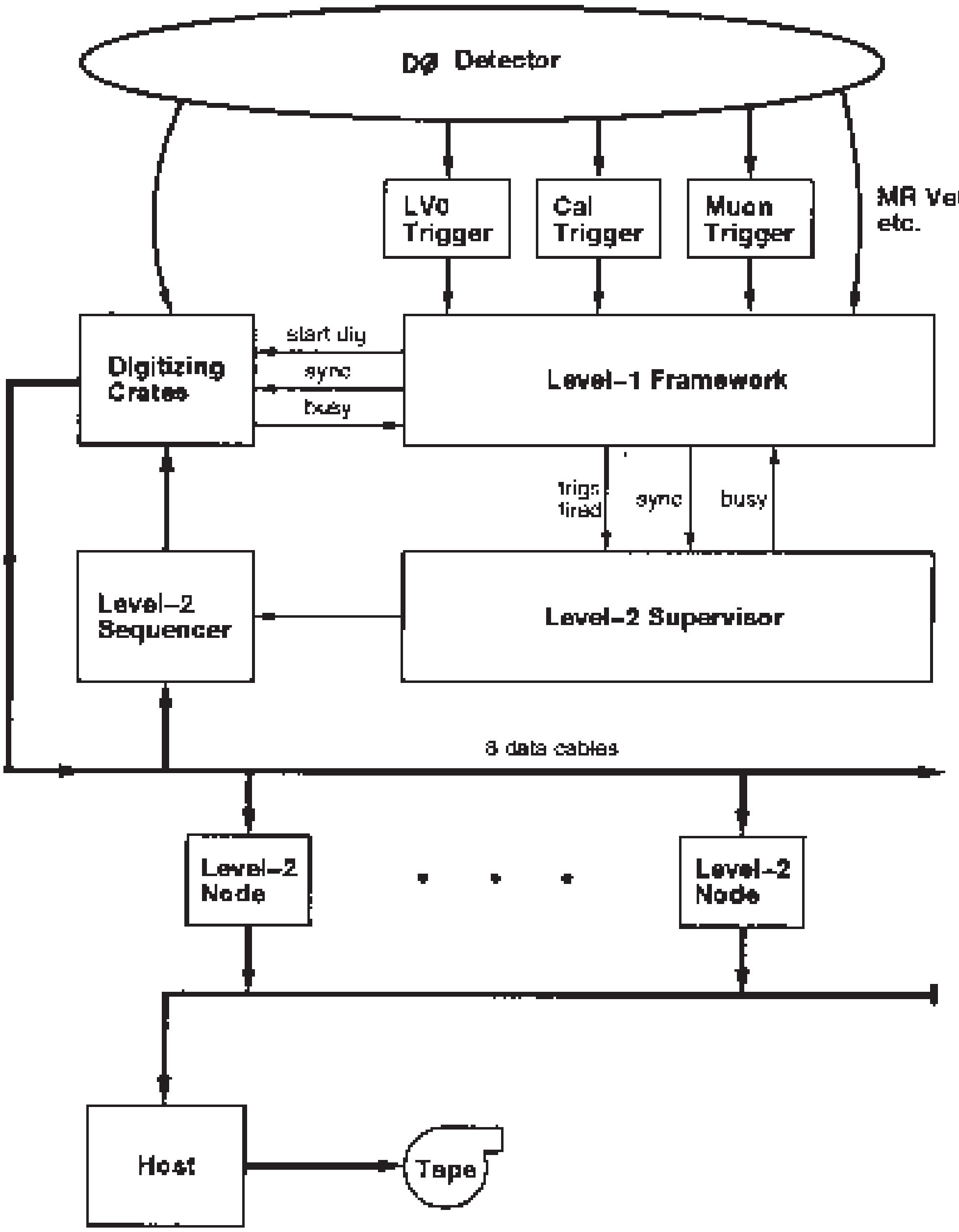

Figure 3.1: Schematic diagram of the DØ Trigger System.

If an event passes the Level-1 trigger it is completely digitized and the data sent to one of the 48 Level-2 nodes. Fast event reconstruction software resides in the Level-2 processors which reduce the event rate to about 2 Hz. Events which pass Level-2 trigger are transferred to the host system for event monitoring and recording on permanent storage medium.

In the following we briefly discuss the main components of the trigger system, but a detailed discussion can be found elsewhere [35, 65–67].

3.1.1 Level-0

The Level-0 trigger [68, 69] indicates the occurrence of inelastic collisions and serves as luminosity monitor. It comprises two sets of scintillator hodoscopes mounted on the front surfaces of the two end-calorimeter modules. These hodoscopes have a checker-board like pattern of scintillators giving partial coverage in the region $1.9 < |\eta| < 4.3$ and full coverage for $2.3 < |\eta| < 3.9$. The spectator quarks in an inelastic $p\overline{p}$ collision hadronise in the far forward region; thus one looks for a coincidence between signals from the two sets of hodoscopes. The rapidity coverage is set by the requirement that the detector be $\geq 99\%$ efficient in detecting non-diffractive inelastic collisions. Good knowledge of z coordinate of the interaction vertex is necessary for the precise determination of the transverse momentum (energy) of electrons, jets or muons. It is determined by comparing the arrival times of the signals at the two hodoscopes. A fast determination of the vertex with a resolution of ± 15 cm is available within 800 ns after the collision and is used by the Level-1 trigger. An event is accepted at Level-0 if $|z_{vtx}| < 100$ cm. More precise value of the vertex with resolution ± 3.5 cm (slow z) is determined within 2.1 μs for use in the Level-2 trigger. The Level-0 trigger is also used to identify multiple interactions in an event by analysing the distribution of arrival times.

3.1.2 Level-1

Once an event is recognised by the Level-0 trigger as originating from hard scattering it is passed on to the Level-1 setup. Most decisions are made between the two bunch crossings but some events require additional confirmation (known as Level-1.5 trigger) which can come after several bunch crossings. The overall control of the Level-1 trigger components and the interface to the next higher level reside in the Level-1 framework [70–

72]. The inputs to the Level-1 framework are 256 *trigger terms* comprising data from the calorimeter, the muon system, the Level-0 hodoscope and the accelerator timing signals. It also uses information about main ring activity to veto events which are suspected to be corrupted. The 256 trigger terms are reduced to a set of 32 Level-1 *trigger bits* by an AND-OR network. Each of these trigger bits requires that a specific pattern of the trigger terms be satisfied. Users can download through the Trigger Control Computer (TCC) the threshold for the firing of the AND-OR terms or a specific pattern. Each trigger bit also has a programmable prescale. If a prescale is set to a value N then the trigger will actually fire only once in every N times the trigger conditions are satisfied.

When a Level-1 trigger is satisfied, the framework sends commands to the digitising crates to start digitisation, and send the trigger decisions to the Level-2 system. The digitisation hardware is located in 86 front-end VME crates. If an event needs Level-1.5 confirmation, the framework starts digitisation but delays notifying Level-2. If the event passes the Level-1.5 requirements, the framework sends the digitised event to Level-2; otherwise it aborts digitisation. As mentioned earlier the Level-1 trigger checks the main ring activity. This is important because the the main ring passes through the DØ calorimeter and the loss of particles from the main ring may contaminate the information from the calorimeter or the muon system. The maximum losses in main ring occur during injection (beam injection into the main ring) and transition (when the accelerating fields are changed to compress the bunches). This is called MRBS_LOSS. Events during these periods are vetoed, resulting in a dead time penalty of $\sim 17\%$ [73]. Moreover when main ring bunches pass through the detector losses can occur. The veto to take care of this is called MICRO_BLANK and it causes a dead time of about 8% [73].

3.1.3 Level-2 and Data Acquisition System

The DØ data acquisition system and the Level-2 filter are closely related. Level-2 is a software filter which uses the digitised information of an event and performs fast reconstruction enabling application of sophisticated criteria to reduce the event rate from about 200 Hz to about 2 Hz. This trigger system is a farm of 48 Vaxstation 4000 processors running in parallel. These processors are connected to a multiport memory via a VME bus. As indicated in Fig 3.1, the process of transferring an event from the digitising crates to a Level-2 node is controlled by a Level-2 supervisor. Once an event is received by a Level-2 node, it is converted to ZEBRA format [74] , a standard format used at DØ for all subsequent data processing. The Level-2 filtering software is a collection of "tools". Each tool can take a set of parameters describing the cuts to be made. The lists of tools with specific values for the parameters are collected together into *filter scripts*. Each of the 32 Level-1 trigger bits is associated with one or more of the 128 filter scripts. Depending on the Level-1 trigger mask the Level-2 system calls in a sequence every script associated with the Level-1 bits which were set. If at least one of the scripts is passed, the event is temporarily written to disk and later transferred to 8mm magnetic data tapes for further processing.

3.2 Event Reconstruction and Particle Identification

The events recorded by the data acquisition system (RAW events) contain information like digitised counts in calorimeter cells, counts per time bin of a tracking chamber etc. However, in physics analysis one studies the objects like jets, electrons, photons etc.. The process of converting the raw data into interesting physics objects is called the *reconstruction.* In DØ this task is performed by a huge computer program (about 150,000 lines long) called DØRECO [35, 75].

3.2.1 The Reconstruction Program: DØRECO

Apart from the raw data, DØRECO needs detector survey and calibration information as its input. The outputs of DØRECO consist of two different sets of files both written in the Zebra format: the standard stream (STA) and the data summary tape (DST). Size of STA files for an event is quite large, typically $\sim 600-1000$ kbytes, and it contains the raw information along with the reconstruction results. DST contains those results of the reconstruction and summary of the event data which are likely to be needed frequently for the physics analysis. The size of DST file is about 15 kbytes/event. The enormous volume of data collected by the DØ detector necessitated further reduction in the size of data files that can be kept in the disk. This third set of data files called micro DST's (μDST's) contain minimum amount of information needed for further analyses in a compressed format.

The reconstruction program performs three major tasks.:

- *Hit finding*, in which, digitised signals from the sense wires of the tracking chambers are converted into spatial locations of hits. Also, signals from calorimeter cells are converted to energy depositions.
- *Tracking and Clustering*, where the tracking chamber hits are joined together to form tracks and the calorimeter energy depositions in the cells are grouped to form clusters.
- *Particle identification*, during which the tracking and calorimeter information are combined to form candidates for electrons, photons, jets, or muons. The criteria applied by DØRECO in choosing the candidates are quite loose.

The first step in reconstructing a track in the central detector is unpacking the digitised charge versus time bin data of all sense wires. The identification of individual pulses is achieved by looking for leading and trailing edges of the pulses. The total charge deposited (used later to find dE/dx) is found by integrating the pulse. The time of arrival of the pulse is used to determine the position. Due to the left-right ambiguities there are two possibilities of the location of the hits; hence two sets of hits are stored, one at the actual position of the track and the other at its mirror image.

After the individual hits are found, track *segments* in each layer are formed by fitting groups of hits in a straight line. At this point, due to the stagger in the sense wire positions, the sets of hits corresponding to the true track yield a better fit. Segments from different layers are then matched to form tracks. Finally, tracks are matched between vertex chamber, TRD and the CDC (or FDC) to reconstruct the final track. More details on the central tracking reconstruction can be found elsewhere [54–57].

As mentioned earlier the z position of the interaction varies widely from event to event. Since it is essential to know the θ direction of the particle to calculate its transverse momentum or energy, the z vertex of each event must be precisely determined. Since the cross-section of the beam is very small $\sim 50\mu m$, the (x,y) position of the vertex can be taken as (0,0). To measure the z position of the vertex, the CDC tracks which have an impact parameter with respect to the z axis of less than 2.5 cm are projected into the (r,z) plane. After that, a histogram is made from the positions of convergence of these tracks with the z axis. The highest peak is attributed to the primary vertex (resolution achieved by this method is about 1-2 cm) and any other peak is attributed to the secondary vertex due to multiple interactions. It should be noted that the smaller peak should at least be 7 cm away from the main peak for it to be resolved.

In the calorimeter, hit finding converts the raw information of digitised counts from each cell to energy, with appropriate calibrations determined from test beam measurements. Corrections are applied to account for cell-by-cell variations in gain and pedestals. The cell energies are converted to transverse energy values by using the position of the interaction vertex. Cells with the same η and ϕ are grouped together to form *towers*. These towers are used in the next stage to form electrons, photons and jets.
Data from the muon system are processed following the same idea as is used in the central detectors but due to the differences in geometry and front-end electronics the details are different.

3.2.2 Electron/Photon Identification

Electrons or photons are identified by the nearest neighbour algorithm [76] as the localised deposition of energy in the electromagnetic section of the calorimeter. At first all EM towers are arranged in the decreasing order in E_T. Beginning with the highest E_T tower, all the neighbouring towers with E_T above 50 MeV are added to the cluster, and the process repeated until all the neighbouring towers satisfying the energy requirements are added to the cluster. A new cluster formation is then begun from the highest E_T tower not previously assigned to a cluster.

Any cluster that has 90% of its energy deposited in the electromagnetic calorimeter and at least 40% of the energy contained in a single tower is identified by the DØRECO package as a candidate electron or photon. The cluster centroid is calculated from the $log(E)$ weighted mean of the cell positions in the third layer of the electromagnetic calorimeter. The position resolution achieved by this method is 1.5-2 mm. Electron candidates are distinguished from photon candidates by requiring the presence of at least one CDC or FDC track within a road of size $\Delta\eta \times \Delta\phi = 0.1 \times 0.1$ pointing from the interaction vertex to the cluster centroid.

The requirements used by the reconstruction program to form candidates are purposely kept quite loose so that the user can apply further requirements tailored for that particular analysis. There are many additional variables for identifying good quality isolated electrons.

Parameters used to identify a good electron in this analysis are, i) isolation fraction (f_{iso}), ii) track match significance and iii) H-matrix χ^2. In the following section we discuss them in detail.

- Isolation Fraction: This is defined by comparing the electromagnetic energy within a cone of radius $\sqrt{\Delta\eta^2 + \Delta\phi^2} = 0.2$ centered around the electron $[E_{EM}(0.2)]$ to the total energy contained within a concentric cone of radius 0.4 $[E_{tot}(0.4)]$. The isolation fraction is defined as:

$$f_{iso} = \frac{E_{tot}(0.4) - E_{EM}(0.2)}{E_{EM}(0.2)} \tag{3.1}$$

- Track Match Significance: A significant source of background to electrons is from photons produced either directly or by the decay of a π^0 or η. Such photons are expected not to have a track in the central detector but due to the overlapping tracks from nearby charged particles they may be reconstructed as electrons. This background can be reduced effectively by requiring that the track point at the centroid of calorimeter cluster. To quantify this, track match significance parameter S, is defined as (for CC)

$$S = \sqrt{\left(\frac{\Delta\phi}{\sigma_{\Delta\phi}}\right)^2 + \left(\frac{\Delta z}{\sigma_{\Delta z}}\right)^2} \tag{3.2}$$

  For EC, z is replaced by r.

- H-matrix χ^2: The longitudinal and transverse development of showers for electrons or photons are different than those for hadrons. The shower shape can be characterised by a covariance matrix [77, 78] derived from a sample of N simulated electrons :

$$M_{ij} = \frac{1}{N}\sum_{n=1}^{N}(x_i^n - \overline{x}_i).(x_j^n - \overline{x}_j) \tag{3.3}$$

  where the observables $x_i (i = 1, 41)$ are fractional energies in layers 1, 2 and 4 of the EM calorimeter, the fractional energies in each cell of a 6×6 array around the shower centre in the third EM layer, the z position of the interaction vertex, and the logarithm of the total cluster energy.
  The matrix M is calculated individually for towers at different $|\eta|$, so there are 37

distinct matrices.

Given the matrix M the χ^2 is defined as

$$\chi^2 = \sum_{ij} (x_i^n - \overline{x}_i).H_{ij}.(x_j^n - \overline{x}_j) \tag{3.4}$$

where H is the inverse of M.

3.2.3 Muon Identification

Muons are identified by the tracks they leave in the muon chambers which point back to the interaction vertex. The reconstruction of the muon tracks, similar to that of that of central detector tracks, starts from conversion of the raw hits and time information into three dimensional position information. Then the hits are fit to a straight line and point to the interaction vertex. Since the muon system is embedded in a toroidal magnetic field for momentum measurements, the tracking is done separately for segments before and after the magnet. The segments are then matched and the momentum is determined from the measurement of the bend of track while passing through the magnet. The momentum resolution can be improved by a global fitting, in which the muon tracks can be associated with a track in the central detector and the event vertex. The momentum measured in this way needs to be corrected for the loss of several GeV of energy in the calorimeter. This loss is estimated through simulation.

Primary backgrounds to muon candidates are the cosmic rays and the leakage of hadronic showers out of the calorimeter called *punchthroughs.* To reduce the cosmic ray contamination a track in the central region ($|\eta| < 1.0$) is rejected if there is another track located back to back both in η and ϕ. To enhance the cosmic ray rejection capability during the later part of data taking, the outer layers of the muon detector were partly covered with large area scintillator detectors to provide a cosmic muon veto. The timing information from these scintillators can be effectively used to reject cosmic ray muons.

The hadronic punchthrough is important only in the transition region of the central and end calorimeters.

Several variables were devised to identify good muons but as events involving muons are not the focus of this analysis, we will not discuss them in further detail.

3.2.4 Reconstruction of Jets

Most DØ analyses reconstruct jets using a cone jet algorithm [79–81] which proceeds as follows:

- Preclustering: The calorimeter towers are first ordered in E_T. Starting from the highest E_T tower, for every tower with $E_T > 1$ GeV, a precluster is formed from all adjacent towers with $\Delta\eta < 0.3$, $\Delta\phi < 0.3$. Preclustering continues until all the towers with $E_T > 1$ GeV are assigned to a precluster. The E_T-weighted centroid of each precluster defines the axis of the corresponding candidate jet.

- Cone Clustering: Starting from the candidate jet axis, all towers within a radius of R in the $\eta - \phi$ space (for this analysis R is chosen to be 0.5) are assigned to the cluster. The centroid of this new jet is recalculated. If the new jet axis is different from the earlier one, then the summation is redone and axis recalculated. This process is repeated until it stabilises.

- Merging and splitting: No towers should be shared among jets. But during cone clustering it may happen that few towers are shared among different jets. If two jets share some towers, the fraction of the total energy which is shared between them is examined. If it is more than 50% of the E_T of the softer jet then the two jets are merged and jet axis is recalculated. Otherwise, they are split into two jets with each tower being assigned to the closest jet.

- To suppress random noise fluctuations that can produce jets, an E_T threshold of 8 GeV is imposed.

The jet candidates have a large number of quality variables associated with them. The parameters used in this analysis are the i) coarse hadronic fraction (CH fraction): the ratio of the energy deposited in the coarse hadronic calorimeter to the energy of the jet, ii) The hot cell ratio: the ratio of the energy deposited in the hottest to the next to hottest cell and iii) the em fraction: fraction of the energy deposited in the EM calorimeter to the total energy of the jet.

3.2.5 Reconstruction of $\not\!\!E_T$

Since the neutrinos are neutral and weakly interacting, they do not leave any trace in the detector and their energy cannot be measured. However, their presence can be inferred

by the momentum imbalance in an event. In $p\overline{p}$ collisions the initial momentum of the colliding partons along the direction of the beam is not known and therefore the momentum conservation cannot be applied. But as the initial momentum in the transverse plane is very small one can apply conservation of momentum in the plane perpendicular to the beam direction. The transverse energy components are added vectorially and any significant deviation from zero is attributed to one or more neutrinos which escaped detection. The reconstruction software supplies three different sets of $\not{E}_T$; the first one is based on the calorimeter measurements, second incorporates the information from the ICD as well as Massless Gaps and the third takes into account the muons.
The calorimeter $\not{E}_T$ is defined as

$$\not{E}_T{}^{cal} = \sqrt{(\not{E}_x{}^{cal})^2 + (\not{E}_y{}^{cal})^2} \tag{3.5}$$

with

$$\not{E}_x{}^{cal} = -\sum_{i=1}^{n} E_i sin\theta_i cos\phi_i \tag{3.6}$$

and

$$\not{E}_y{}^{cal} = -\sum_{i=1}^{n} E_i sin\theta_i sin\phi_i \tag{3.7}$$

where E_i is the energy deposited in the cell i. For the muon corrected $\not{E}_T$, the momenta of the muons are added vectorially in the above sum and the estimated energy loss of muons in the calorimeter is subtracted.

3.3 Corrections

The energies of the objects reconstructed by DØRECO need to be corrected for various effects prior to the physics analysis. The following sections briefly discuss the various corrections.

3.3.1 Correction for Electrons and Photons

Calibration of the energy scales of the calorimeters were determined using test beam data. Since the test beam setup and the actual DØ run conditions are not exactly similar, corrections to the energy scale need to be applied to obtain the true energies of the electrons or photons. To do this for electrons, Z resonance is taken as a reference point as its mass is determined accurately by the LEP collaboration. The electron energies are scaled up so that the invariant mass of two electrons (at DØ as determination of charge is not possible, positrons and electrons are not distinguished) match with the Z mass. This correction is about 4-6%. As electron and photon showers are similar in nature, this correction holds for photons as well.

3.3.2 Jet corrections

For physics analyses it is necessary that the energy of a reconstructed jet be the same as the energy of the original parton that formed the jet. However, there are systematic effects which lead to differences. Hence an energy scale correction is needed. The energy scale can be affected by the following:

- Jets are usually composed of a large number of particles of different energies, e.g., approximately 67% of the particles in a 50 GeV jet have energy less than 5 GeV [82]. The response of the calorimeter in this energy region is nonlinear and therefore summing up the response of the calorimeter to each particle does not give the correct result.
- Showering losses of particles outside the jet cone.
- Energy deposited by particles not originating from hard scattering e.g., particles arising from the fragmentation of the spectator quarks (underlying events), or from the natural radioactive decay of Uranium used as absorber in the calorimeter. These sources affect the jets much more than the electrons because they are extended objects.
- The zero-suppression used in the calorimeter readout can produce a shift in the energy.

Correction to jet energy response is obtained by using the method called the $\not\!\!E_T$ projection fraction (MPF) [83]. In this method one looks for events which have one good photon and one jet lying back-to-back in ϕ and no other objects. The photon energy is corrected using the electromagnetic energy scale correction. There should be no neutrinos in these events, so that any $\not\!\!E_T$ in the event is due to the mismeasurement of the energy of the

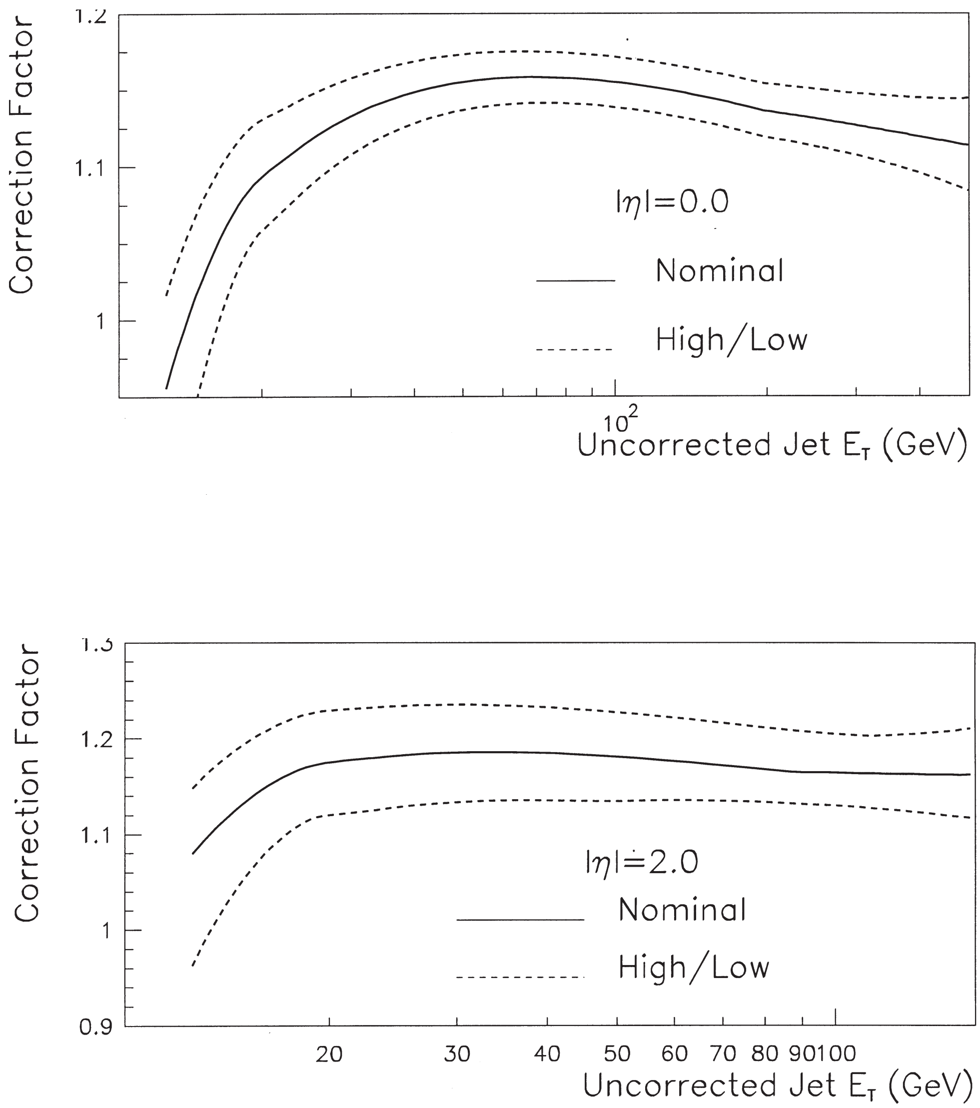

Figure 3.2: Energy scale corrections for both the central calorimeter and the end calorimeter.

hadronic jet. By projecting the $\not{E}_T$ along the jet axis, the required correction can be obtained.

Contribution from the underlying event is measured from the minimum bias events and the out of cone showering has been determined from the test beam data. The corrections arising due to zero suppression, and uranium noise have been obtained from data taken without zero suppression.

Finally these corrections are obtained as a function of E_T of the jets in the central and end calorimeters separately, as shown in Fig 3.2.

3.3.3 Corrections for $\not{E}_T$

As $\not{E}_T$ is obtained from energy deposits in all the cells in the calorimeters, it is mismeasured to the same extent to which objects in the calorimeters are mismeasured. So the correction to $\not{E}_T$ is obtained by taking the difference between the summed uncorrected E_T and summed corrected E_T of the calorimeter objects.

Chapter 4

Analysis of Collider Data and Estimation of Background

In this chapter, the analysis of the data to look for the evidence of supersymmetry in the R-parity violating scenario is discussed. The chapter begins with a description of the data sample. The online trigger and the offline selection requirements used for this analysis are then described with their justifications. This is followed by a discussion of the background modeling and the method adopted for their estimation. This chapter also describes the consistency checks made to establish the validity of the background modeling.

4.1 Data Sample

In this analysis, we have used the data collected by the DØ detector during the 1994-95 collider run (Run 1B). Luminosity delivered by the accelerator and recorded at DØ in collider Run I between 1992-95 is shown in Fig. 4.1. Runs during which the detector system or the data acquisition system had problems are excluded. The resulting data sample from Run 1B corresponds to an integrated luminosity of $96 \pm 5.2\ pb^{-1}$, where the quoted uncertainty of 5.4% includes the error in Level-0 trigger efficiency and the error in the inelastic scattering cross-section.

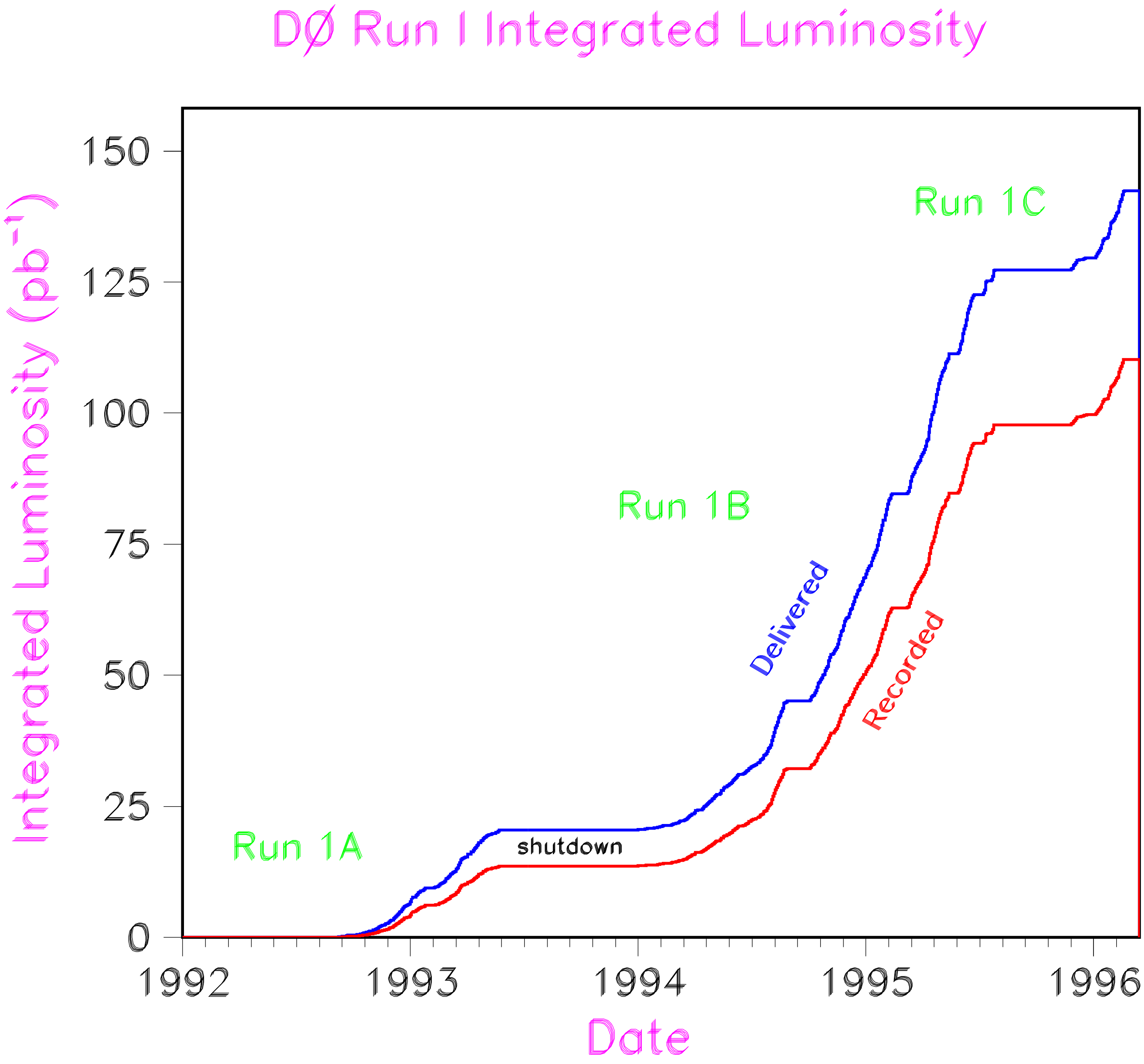

Figure 4.1: Delivered and recorded luminosity during Run I (1992-95).

4.2 Monte Carlo Simulation

In this analysis, for the study of signal and background processes, we will use the Monte Carlo simulation techniques extensively. In general, this proceeds in three steps:

- event generation, in which simulation of the particle collisions is done,
- detector simulation, where the simulation of the final state particles passing through the detector is done, and finally,
- simulation of the trigger.

In the following we will discuss these three steps in brief.

4.2.1 Event Generation

While there exist a number of event generators for the simulation of hadron-hadron collisions, we use in the present analysis ISAJET [84], PYTHIA [85] and HERWIG [86] programs which produce an output that is compatible to the detector simulator at DØ. ISAJET has been used for the generation of signal events and all three event generators have been used for simulation of various background processes (discussed in detail later). The basic steps followed in all these event generators are similar but they differ in the details of their implementation.

- A primary hard scattering is generated using QCD cross-section for two body parton-parton scattering and for appropriate parton structure functions.
- All partons participating in the hard scattering are then evolved through repeated branchings according to the Altarelli-Parisi splitting functions. Through this procedure both initial and final state radiations are generated.
- Quarks and gluons produced in the first two steps are then fragmented into hadronic final states. This process is known as fragmentation or hadronisation. As this cannot be done in perturbative QCD, different event generators employ different empirical schemes for hadronisation, e.g., ISAJET uses Feynman-Field scheme [87], PYTHIA uses Lund String fragmentation scheme [88] and HERWIG uses Cluster hadronisation model [86].

- The final step in the event generation is to evolve and hardonise the leftover partons known as "spectators". There is no unique way of dealing with the leftover partons. PYTHIA uses an extension of the Lund Colour scheme whereas in ISAJET and HERWIG, a minimum bias event is overlaid on top of the primary hard scattering event.

4.2.2 Detector Simulation

A detailed simulation of the detector response when particles pass through it is necessary to understand the systematic effects. At DØ the primary package for detector simulation is based on the GEANT [89] program developed at CERN. This program simulates the tracks and interactions of the particles traversing through a volume containing user-specified material. The interactions included in it are electromagnetic and hadronic showering, decays of short-lived particles, multiple Coulomb scattering, electron and muon bremsstrahlung and production of δ-rays. GEANT collects the response from all these processes in the detector and converts them to simulated digitised signals.

The most critical and error prone step in using GEANT is the coding of the geometrical model. In the adaptation of GEANT at DØ, called the DØGEANT, the complex geometrical model using fortran code has been replaced by a number of ASCII data files which are read by the program and contain all the arguments for the GEANT geometry routines. The DØGEANT does tracking in the tracking chambers and the muon chambers in great detail.

A full simulation of the calorimeter using complete details of uranium plates, liquid argon gaps, G10 signal boards etc. (often referred to as plate level Monte Carlo) takes an inordinate amount of time generating and tracking hundreds of secondaries through the calorimeter volumes. Therefore it is necessary to take some steps to speed up the simulation in the calorimeter part. One way of doing it is called the Mixture Monte Carlo in which the calorimeter is modeled as homogeneous blocks of uranium-G10-argon mixture. This greatly reduces the number of volumes and hence speeds up tracking [90]. However, the sampling fluctuations and attenuation of electromagnetic energy to obtain correct resolution and e/π response ratio must be put in by hand. An even faster option uses Shower Library [91–93]. In this method no tracking is done in the calorimeter. Electrons, photons and hadronic particles are stopped on entry and a matching shower is obtained from a library on a direct access data file. Large number of showers generated using the full DØGEANT package is used to make the library file.

4.2.3 Trigger Simulation

Not all the events due to hard scattering are recorded by the data acquisition system. Thus, to have a realistic estimation of the efficiency with which a given event can be detected, one needs to treat the events passing through DØGEANT as raw data and pass them through the trigger generators. For this purpose, the program TRIGSIM [94, 95] which is actually a combination of two packages L1SIM and L2SIM is used to simulate the function of the trigger system. The simulator uses the same configuration files which are used at the time of data taking.

4.3 Event Selection

The online trigger and offline selection criteria are chosen after studying the features of both the signal and background processes in order to retain a sizable fraction of signal events and also to reduce the background significantly.

4.3.1 Triggers

The trigger JET_MULTI is found to be the most suitable for this analysis. The level-2 requirements for this trigger are
a) five or more jets with a cone of radius $\mathcal{R}$ $(= \sqrt{(\Delta\eta)^2 + (\Delta\phi)^2}) = 0.3$ and $|\ \eta\ | \leq 2.5$
b) $H_T \geq 115$ GeV, where H_T is the sum of E_T of all Level-2 jets within $|\ \eta\ | \leq 2.0$.

The efficiency of this trigger condition is determined by the trigger simulator to be 95±5%.

4.3.2 Offline Selection Criteria

In the following, we first describe the definition of electrons and jets used in this analysis (quality cuts) and then describe the kinematic cuts.

Electron Quality Cuts:

The following parameters described in the previous chapter are used for defining good and isolated electrons:

- EM fraction (f_{EM}),
- Isolation fraction (f_{iso}),
- Cluster shape (χ^2) and
- Track match significance (S).

As mentioned in chapter 3, the DØRECO makes cuts only on the EM fraction ($f_{EM} > 0.9$) in identifying an electromagnetic object (electron or photon). In addition, electrons for this analysis are required to satisfy the following conditions:

$$f_{iso} < 0.15, \quad \chi^2 < 100 \quad \text{and } S < 10$$

The variable f_{iso} is used to check the electron isolation. It is a very useful discriminant against electrons originating from the decay of heavy (b or c) quarks. Since an electron is expected to have a track in the tracking chamber, the variable S is used to distinguish it from a photon that has been reconstructed as an electron. The cluster shape variable χ^2 is used to check the resemblance of the shower profile of the candidate electron to that of a true electron.

Electron identification efficiency

Since the quality parameters for electrons cannot be obtained well enough from simulation, electron identification efficiencies ϵ_{el-id} are determined directly from collider data. Electron identification efficiency has two parts: 1) efficiency of all quality cuts (ϵ_{qty}) and 2) electron tracking efficiency (ϵ_{trk}). Efficiency for quality cuts for electrons with $E_T \geq 25$ GeV is determined from $Z \to ee$ data [97]. Efficiencies for track finding in CC and EC are obtained from $(Z \to ee)+ \geq 2$ jets data and are assumed to be independent of the P_T of the particle.

Efficiencies for electron identification and for track finding are given below separately for CC and EC.

	CC (%)	EC (%)
Electron id	93.8 ± 0.7	84.1 ± 2.0
Track finding	85.0 ± 7.0	85.0 ± 7.0

The net identification efficiency for electrons with $E_T > 25$ GeV ($\epsilon^{25}_{el\_id}$) is given by

$\epsilon^{25}_{el\_id} = \epsilon_{qty} \times \epsilon_{trk}$

For lower E_T electrons, a parametrisation of the efficiency as a function of the E_T of the electron for central calorimeter (CC) and end calorimeter (EC) is used. This is obtained [98] from plate level monte carlo electron events overlaid with minimum bias collider data. Monte Carlo events generated at $\eta = 0.4(2.0)$ are used for CC (EC) electrons. Figure 4.2 shows the parametrisation functions, and are expressed as follows for the two fiducial regions of the detector:

$f = 1 - 1.66 \times e^{-0.176 E_T}$, $E_T \leq 25$ for CC;
$f = 1 - 1.09 \times e^{-0.153 E_T}$, $E_T \leq 25$ for EC and
$f = 1$, $E_T \geq 25$ for both CC and EC.

The net efficiency for identifying electrons with $E_T \geq 10$ GeV is given by

$\epsilon_{el\_id} = \epsilon^{25}_{el\_id} \times f$.

Jet Quality cuts:

We have used the following cuts on the jet parameters in order to suppress the contribution from main ring activity as well as from noise in the calorimeter:

- EM fraction, f_{EM}: $0.05 \leq f_{EM} \leq 0.95$,
- coarse hadronic fraction, $f_{CH} < 0.4$ and
- ratio of the largest signal to the next-to-largest signal in individual cells of the calorimeter (R) to be < 10.

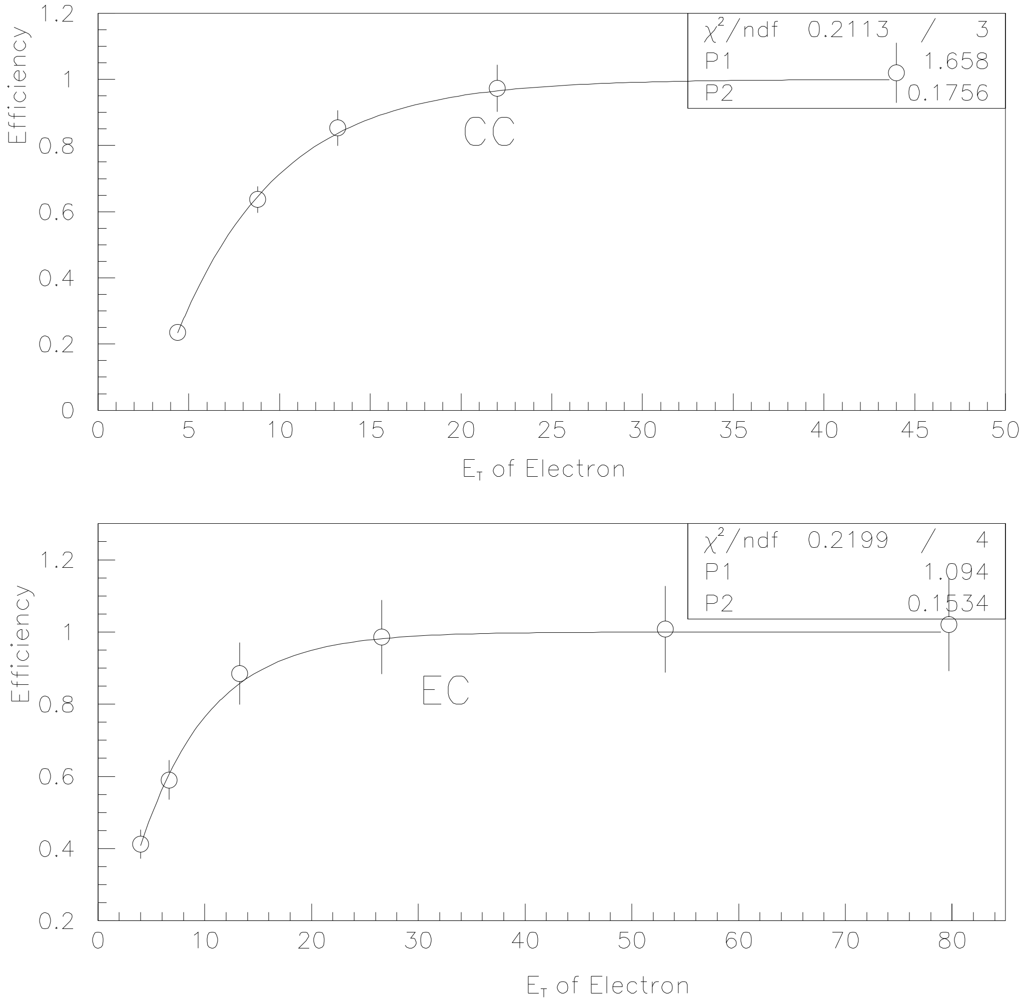

Figure 4.2: Parametrisation for low E_T electron identification efficiency as a function of E_T of electrons. The upper plot is for CC electrons while the lower one is for EC electrons.

The requirement on the EM fraction, defined as the ratio of the energy deposited in the electromagnetic calorimeter to the energy of the jet, is used to eliminate the electromagnetic objects from the jet sample. Jets are required to have at least 5 % as EM fraction because all the jets are expected to deposit part of their energy in the EM calorimeter.

The cut on the coarse hadronic fraction is motivated by the fact that the Main Ring passes through the coarse hadronic calorimeter. Particles which stray out of the Main Ring during the injection or transition phases deposit their energies in the coarse hadronic calorimeter. These are often picked up by the jet reconstruction algorithm to form jets. But the genuine jets are expected to deposit less energy in the coarse hadronic calorimeter. Thus, $f_{CH} < 0.4$ cut helps in discriminating genuine jets from the jets due to the Main Ring splash.

Sometimes jets get reconstructed out of a calorimeter cell that has spurious energy deposition due to detector malfunction. In this case other calorimeter cells within the jet will have very small energy deposited in them. But in a genuine jet the shower profile is expected to be smooth. So, the ratio of the largest signal to the next-to-largest in the individual cells of the calorimeter is a good quantity to eliminate jets arising out of detector malfunction.

Kinematic cuts:

In addition to electron and jet quality cuts the following kinematic cuts are applied to further reduce the background and to improve the signal to background ratio.

- There should be at least two good electrons, one with $E_T \geq 15$ GeV and the other with $E_T \geq 10$ GeV satisfying the electron quality cuts described earlier. These two electrons are required to be within $|\eta| \leq 1.1$ in the central calorimeter (CC), or $1.5 \leq |\eta| \leq 2.5$ in the end calorimeters (EC).

- Number of good jets in the event must be at least four, with $E_T \geq 15$ GeV and $|\eta| \leq 2.5$.

- H_T, the scalar sum of E_T of all the electrons and jets that pass the kinematic, quality and fiducial cuts, must be ≥ 150 GeV.

- The invariant mass (m_{ee}) of the two selected electrons should not be in the range $76\ GeV/c^2 - 106\ GeV/c^2$ (Z mass window).

4.3.3 Effect of the selection criteria on the signal and on the background

The kinematic cuts described above were chosen after studying the effect of these cuts on signal as well as on various backgrounds. This study was done using simulated events for both signal and backgrounds. In this section, we justify the above cuts. For the signal, a typical point in the SUGRA parameter space, $m_0 = 130$ GeV/c^2 and $m_{1/2} = 100$ GeV/c^2 has been chosen for illustration. In making these plots no trigger requirements were imposed. All the distributions are normalised to a luminosity of 100 pb^{-1}.

Figure 4.3 shows the E_T distribution of the softer electron arising from various sources of backgrounds and signal. Only the isolation fraction cut on electrons is imposed in making these plots. It is clear that a cut of $E_T \geq 10$ GeV does not remove any significant amount of signal and it is not effective in removing backgrounds from any of the sources discussed here. But this cut is very important, because unless we impose the 2 electrons requirement many other sources e.g., W+ 4jets, QCD heavy quark (b or c) events where the heavy quark decays to electrons are likely to contribute to the background. The instrumental background is also expected to increase (not shown in the figure).

Figure 4.4 shows the E_T distribution of the jet with the fourth highest E_T from various sources of background and the signal. Figure 4.5 shows the distribution in the number of jets with $E_T \geq 15$ GeV and with quality cuts imposed on them for different processes. It can be seen from these two figures that these cuts are effective in suppressing the background from all the sources.

Invariant mass distributions of the two highest E_T electrons (m_{ee}) are shown in Fig. 4.6. The cut on the dielectron invariant mass removes almost all Z events, without affecting the signal.

A clean H_T cut is important, because in the *JET_MULTI* trigger events were required to have $H_T \geq 115$ GeV at Level-2. Moreover, as seen from Fig. 4.7, the signal is not seriously affected by this cut, but it provides an effective way to suppress events from Drell-Yan and $Z \rightarrow \tau\tau \rightarrow ee$ processes.

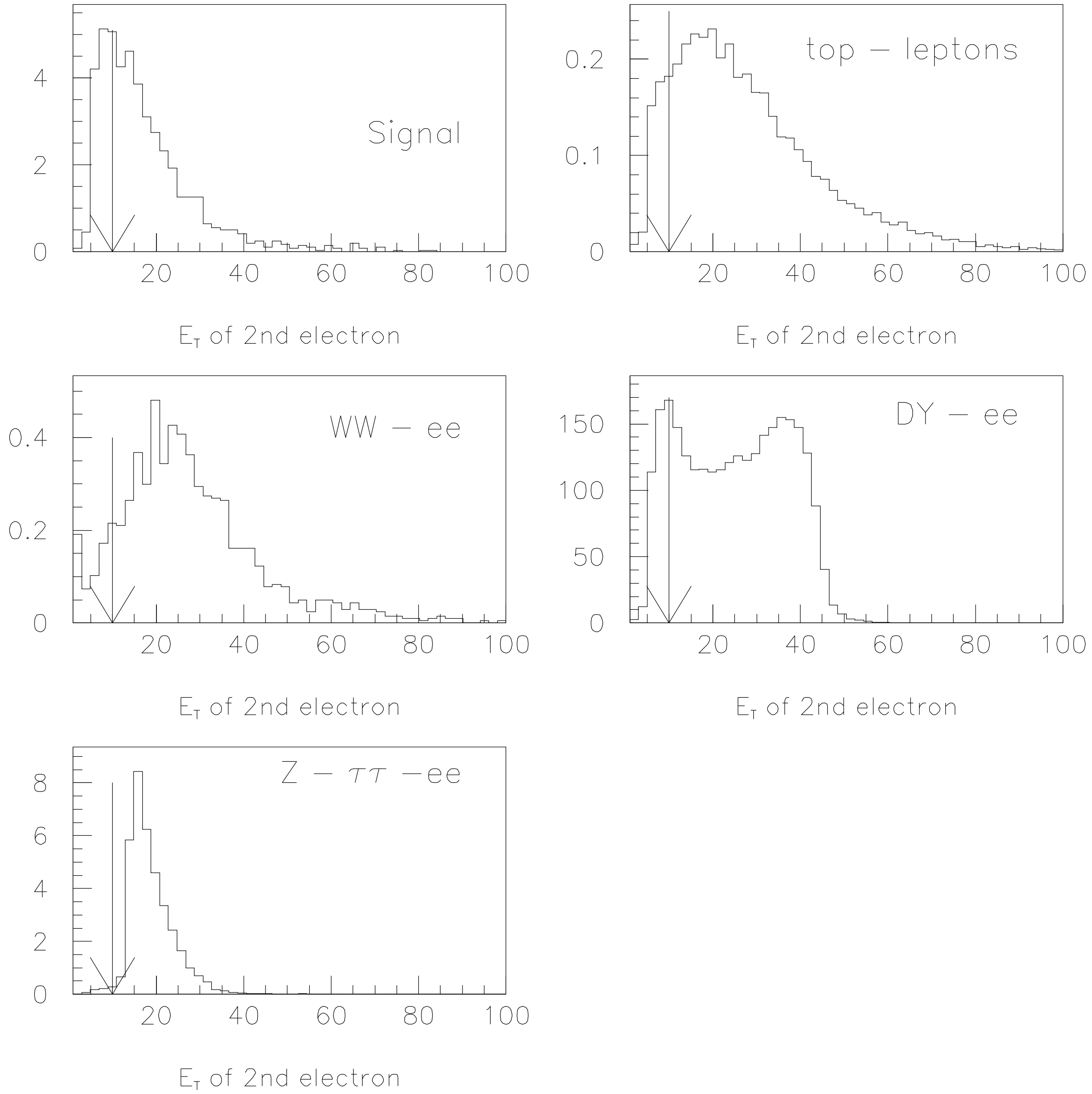

Figure 4.3: E_T distributions of the second highest E_T electron and the chosen cut. (shown by a vertical arrow).

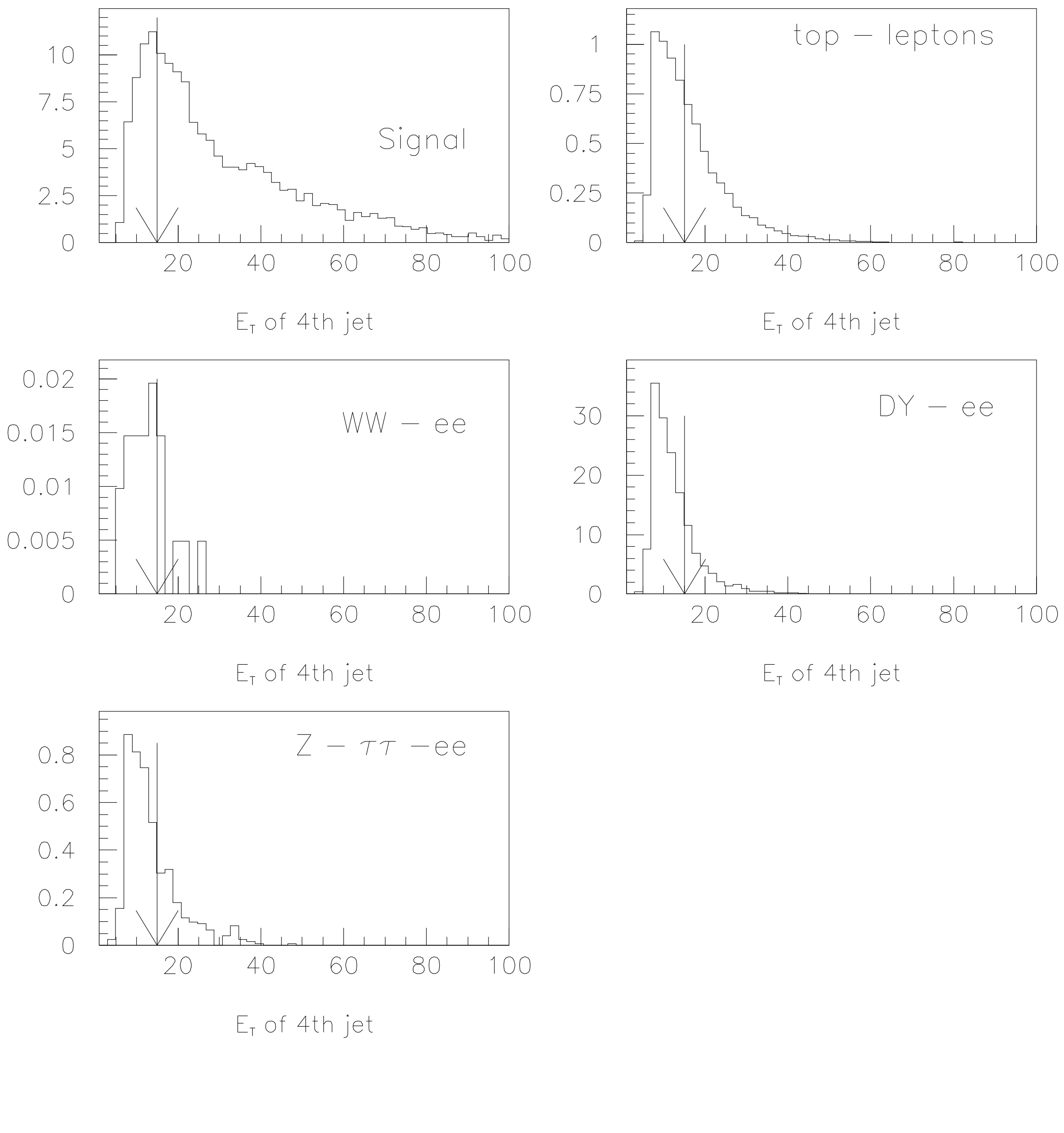

Figure 4.4: E_T distributions of the 4th highest E_T jet and the chosen cut.

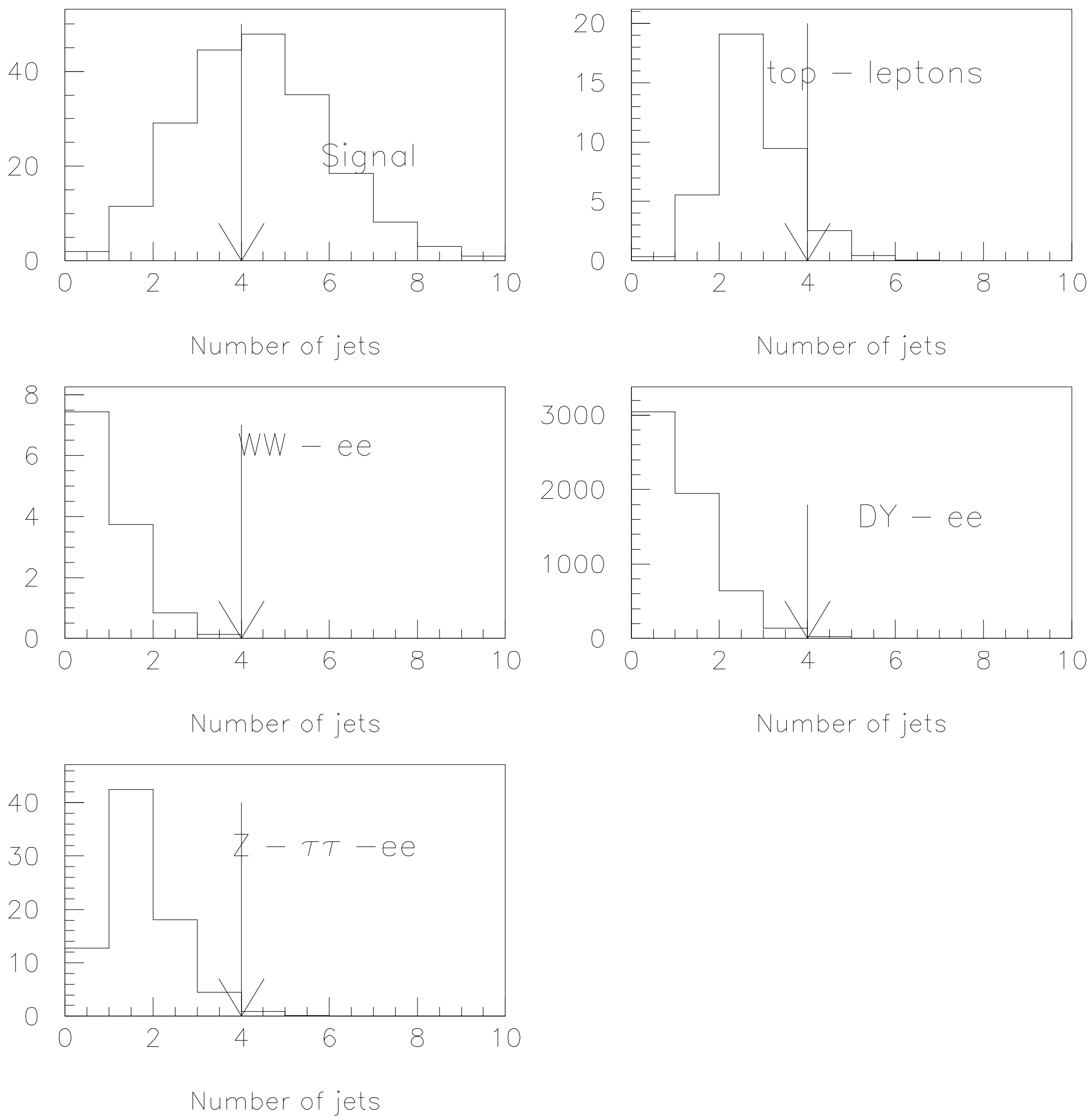

Figure 4.5: Distributions of the number of jets ($E_T \geq 15$ GeV) and the chosen cut on the number of jets.

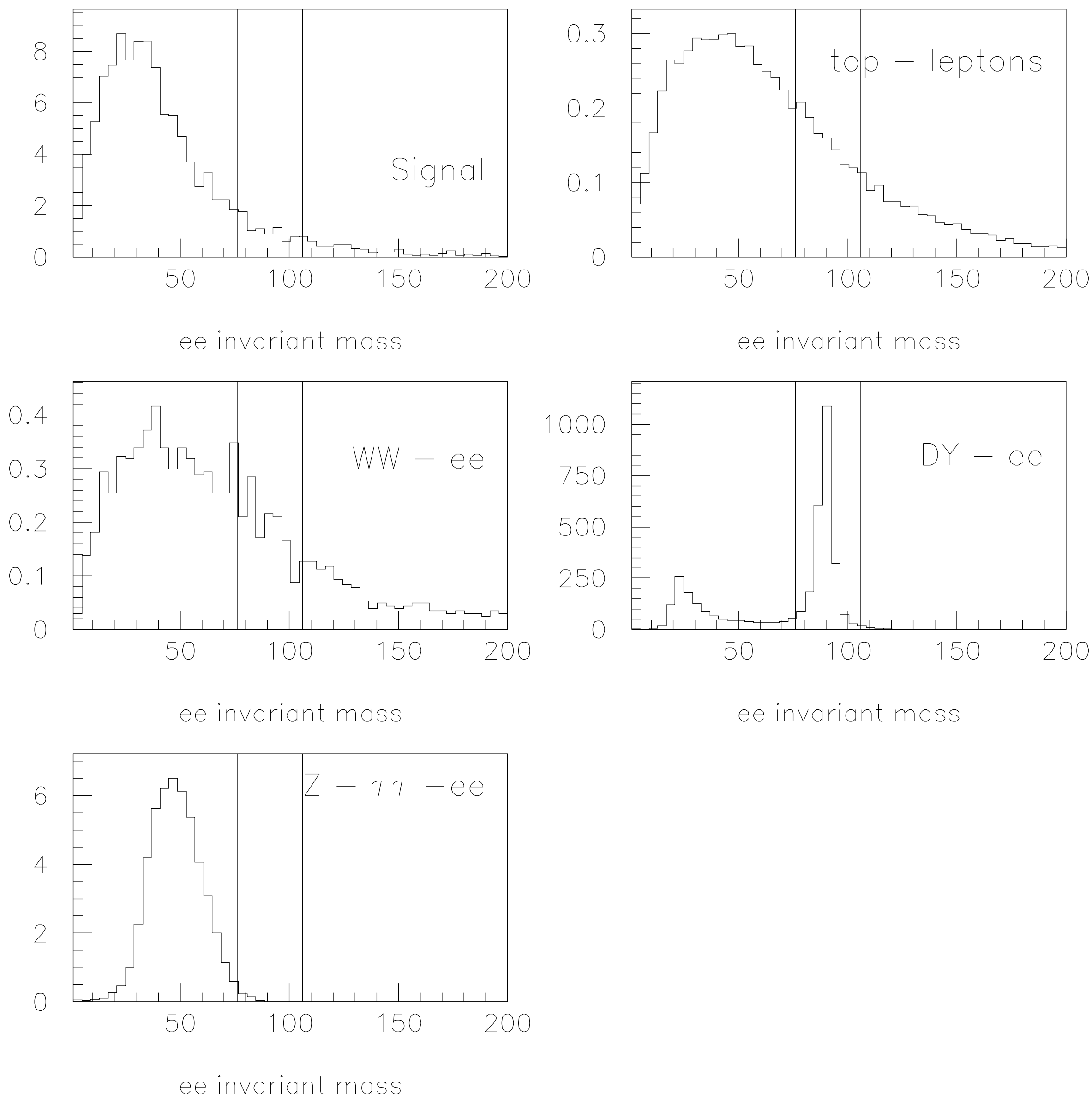

Figure 4.6: Invariant mass distributions for dielectron pairs and the chosen cut.

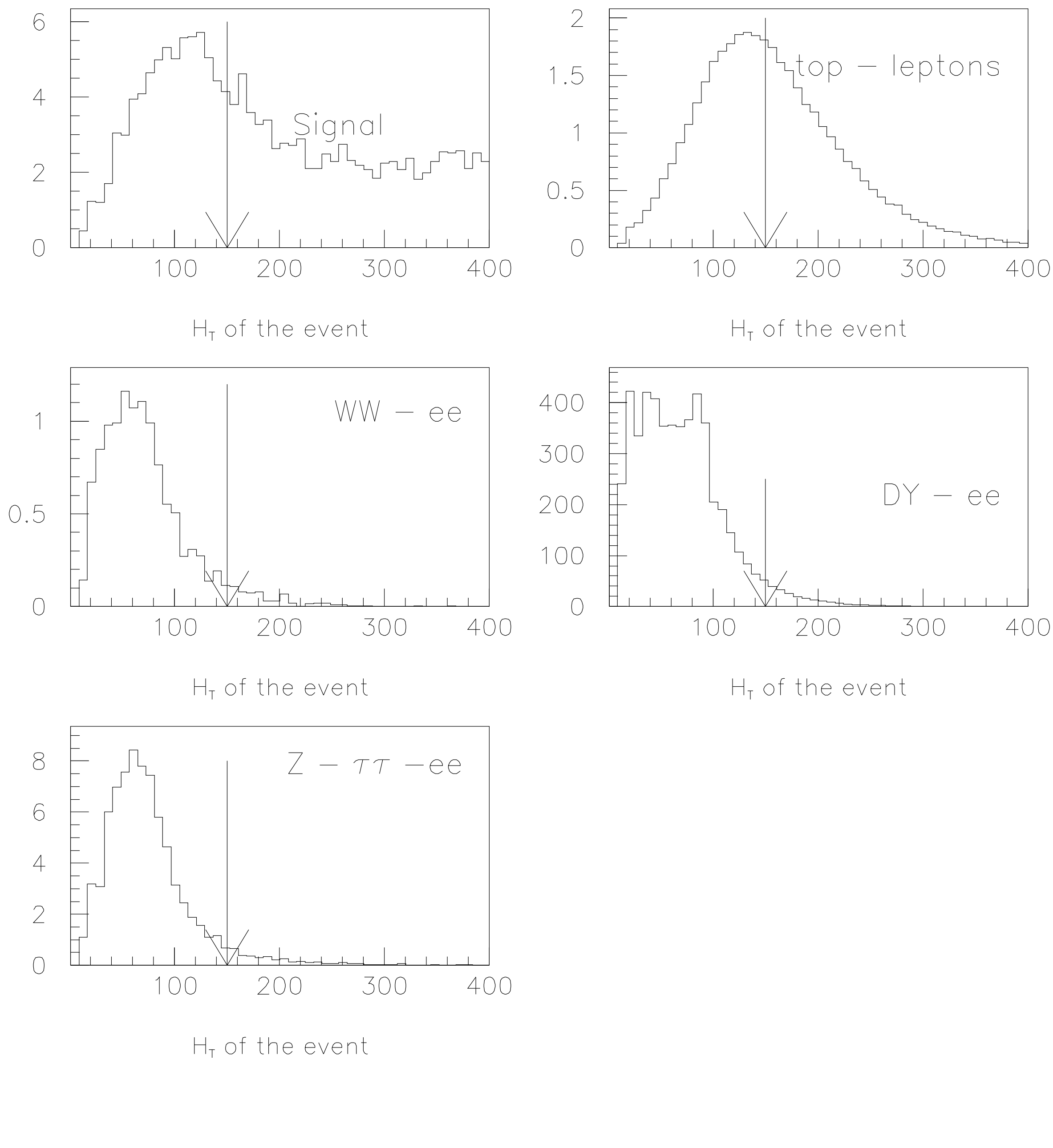

Figure 4.7: H_T distributions and the chosen cut.

4.4 Data Analysis

The data from Run 1B, corresponding to a luminosity of 96 pb^{-1}, have been analysed using the cuts as described above. The effect of imposing these cuts on the data is shown in Table 4.1. A total of 163140 events passed the JET_MULTI trigger described earlier, i.e., each of these events had at least 5 or more clusters (either hadronic or electromagnetic) in the calorimeter with $E_T > 10$ GeV and $H_T \geq 115$ GeV. These events were then analysed further offline to look for R-parity violating SUSY signal in the following way. We first selected those events which have at least 2 electrons within $\mid \eta \mid \leq 1.1$ or $1.5 \leq \mid \eta \mid \leq 2.5$ (EC) passing our electron identification requirements and kinematic requirements (at least one electron with $E_T > 15$ GeV and another with $E_T > 10$ GeV). Only 38 events passed these requirements. These events are then subjected to additional requirements of having 4 good jets with $E_T > 15$ GeV in $\mid \eta \mid < 2.5$ and satisfying the quality cuts for jets. Only 6 events out of the 38 events passed these additional cuts. In order to reduce the Z background, we further required that the invariant mass of the 2 electrons should not be within the Z mass window ($76\ GeV/c^2 < m_{ee} < 106\ GeV/c^2$). Only 2 events survived. These two events also survived the additional requirements on $H_T > 150$ GeV. In Table 4.1 we summarise the effects of imposing these cuts on the data.

Cut	No. of events
Passed trigger requirement	163140
2 electrons satisfying quality, kinematic and fiducial cuts	38
4 jets satisfying quality, kinematic and fiducial cuts	6
Invariant mass cut	2
H_T	2

Table 4.1: Cumulative effect of different requirements on the data sample.

4.4.1 The two candidate events

The end-views and side-views ($r-z$ plane) of the two events surviving all the signal requirements are shown in Fig. 4.8 and Fig. 4.9 respectively. These figures are produced by using PIXIE [96], an event displaying software package used at DØ.

The quantities shown in the figure are uncorrected. Corrected quantities are given in Table 4.2. In the first event, Run # 86211 and Event # 25024, one electron with

Run # 86211	Electrons					
	E_T	η	ϕ	S	χ^2	f_{iso}
Event # 25024	30.78	1.86	0.76	4.61	94.92	0.07
	15.07	2.05	4.26	1.54	27.84	0.08
	Jets					
	E_T	η	ϕ	f_{EM}	f_{CH}	R
Invariant Mass = 42.56	43.14	0.53	6.10	0.61	0.01	1.02
	34.10	-1.69	2.53	0.76	0.01	2.41
$H_T = 171$	29.93	0.78	3.91	0.68	0.04	1.28
	17.97	-2.31	1.98	0.65	0.01	1.39

Run # 84870	Electrons					
	E_T	η	ϕ	S	χ^2	f_{iso}
Event # 29117	62.51	1.73	4.83	3.75	98.75	.01
	48.65	0.78	0.81	1.65	12.07	.01
	Jets					
	E_T	η	ϕ	f_{EM}	f_{CH}	R
Invariant Mass = 113.71	76.00	-0.33	3.07	0.18	0.03	2.56
	75.29	-0.86	5.82	0.71	0.22	1.47
$H_T = 320$	35.26	-0.94	2.46	0.34	0.15	1.18
	22.64	-1.35	1.32	0.44	0.06	1.81

Table 4.2: Details of the two events satisfying all the analysis requirements.

$E_T = 30.8$ GeV is seen at the upper right corner in the $r-z$ plane i.e., view Fig. 4.8(a) in the end calorimeter. The other electron with $E_T = 10.1$ GeV can be seen in the bottom right corner in the $r-z$ view in the end calorimeter. Both the electrons clearly have VTX and FDC tracks associated with them. Jets are also seen in the figure; two of the jets are in the upper left half in the end calorimeter and two other jets are in the lower right half in the central calorimeter. The vertex of the event can also be seen, displaced from

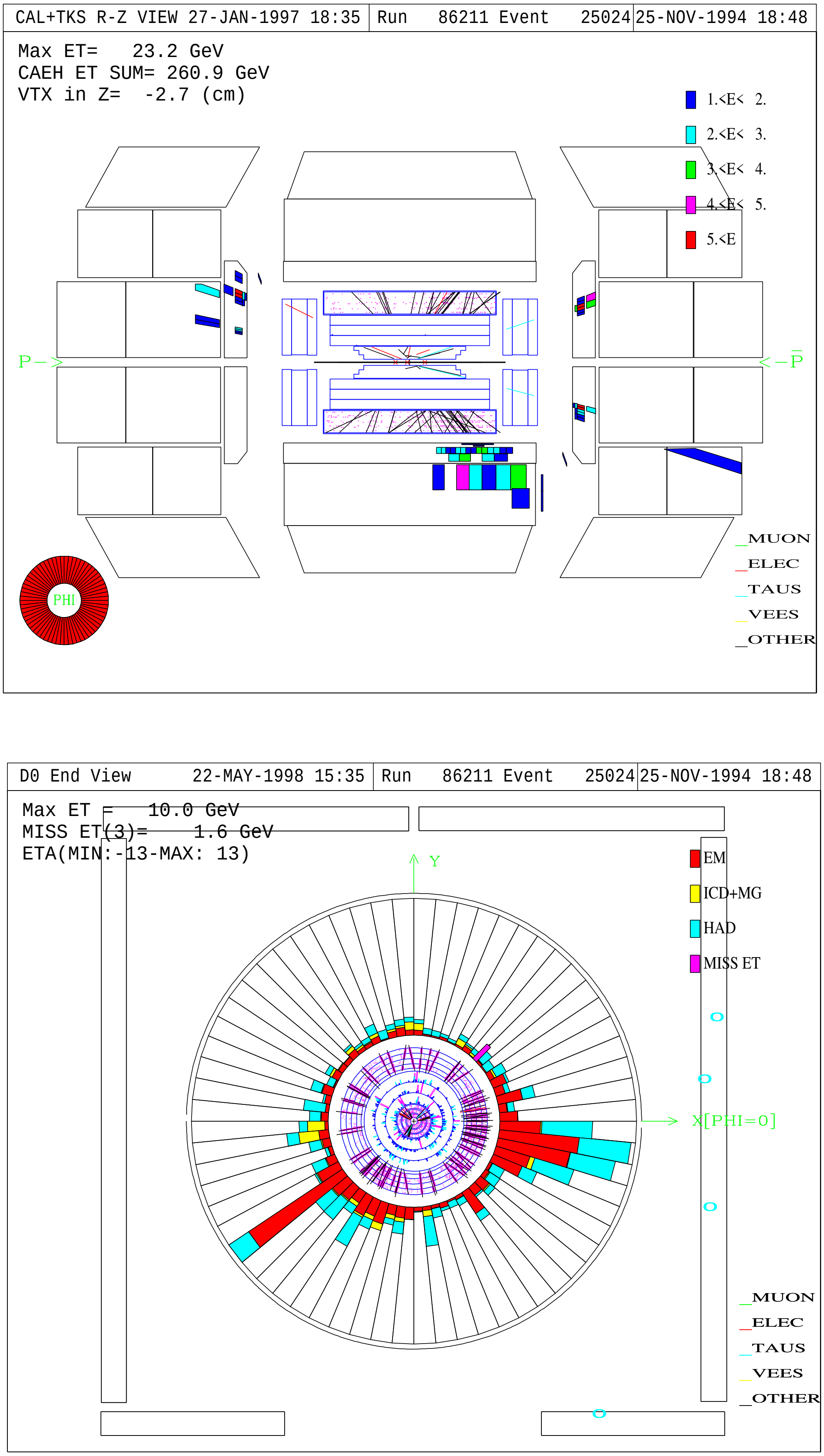

Figure 4.8: Event 86211.

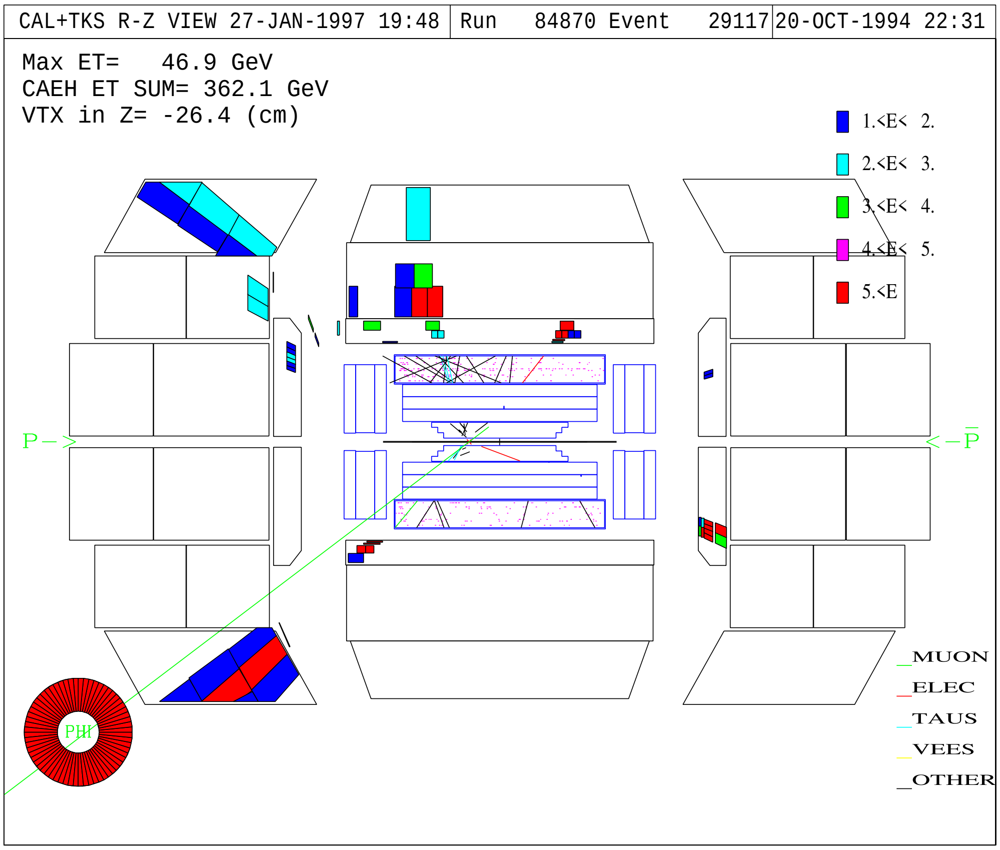

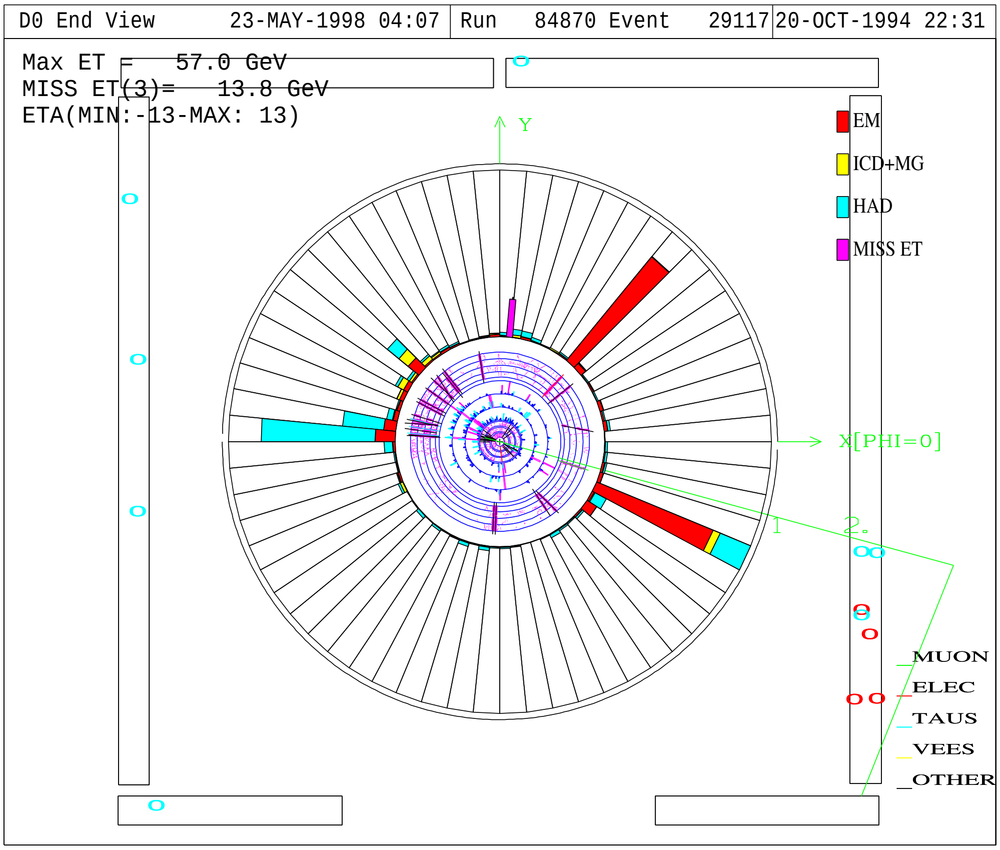

Figure 4.9: Event 84870.

the centre of the detector by about 2.7 cm in the negative direction of the z axis. The end-view, Fig 4.8(b), shows the energy depositions in the ϕ direction for $-1.3 < \eta < 1.3$. Only two jets can be identified from this; other jets and electrons are not seen in the figure, as they have $|\eta| > 1.3$.

The $r - z$ view of the second event is shown in Fig. 4.9(a). The vertex is displaced from the centre of the detector towards the left by 26.4 cm. One electron is seen in the central calorimeter on the upper right hand side of the $r - z$ view and the other one in the end calorimeter on the lower right hand side in the $r - z$ view. Three jets and one electron can be identified easily from the end view.

4.5 Study of Background

After complete analysis of the DØ data, we found that 2 events survive all our requirements. Thus 2 events constitute our final data set. In order to investigate further the origin of these two events we first need to estimate the contribution from various physics processes as well as due to misidentification of certain objects. In principle any known process that gives rise to an event with two or more electrons and four or more hadronic jets satisfying the selected cuts, could constitute a background. These can be classified as (a) background from Standard Model processes (SM backgrounds) and (b) instrumental background due to imperfections in the detector and misidentification of some jets as electrons. We estimate various physics backgrounds using Monte Carlo simulation, whereas the instrumental background is estimated directly from data.

The SM processes that were considered are:

- Drell-Yan production (with $Z^*, \gamma^* \rightarrow ee$)
- $t\bar{t}$ production (with $t\bar{t} \rightarrow ll$ + jets, where $l = e, \mu$)
- Z production (with $Z \rightarrow \tau\tau \rightarrow ee$ + jets)
- WW production (with $WW \rightarrow ee$ + jets)

Specific details of these processes are given below.

1. Drell-Yan: $Z^*/\gamma^* \rightarrow ee$

The cross section for Z^*, γ^*(+ jets) production depends strongly on the mass of the Z^*/γ^*. Four sets of Monte Carlo events, corresponding to the Z^*/γ^* mass ranges of 20-60, 60-120, 120-250 and 250-500 GeV/c^2 were generated using the ISAJET (v7.13) generator. Events were not generated for invariant mass < 20 GeV/c^2 because electrons produced in such events would be too soft to pass the offline E_T cut. No events were generated for invariant mass > 500 GeV/c^2 because the cross section is expected to be small, and their contribution to background negligible. Events were then passed through the detector simulation package DØGEANT (v3.15) using SHOWERLIBRARY, and DØRECO (v12.21). The generated events were processed further only if they had 2 or more electrons with $E_T > 5$ GeV, and 2 or more jets with $E_T > 5$ GeV. While estimating the background these four sets of events were treated as four independent backgrounds and the total contribution from Drell-Yan was obtained by summing them up.

2. $t\bar{t} \rightarrow ll$

To estimate background due to top quark production, events were generated (for $m_t =$ 170 GeV/c^2) using the HERWIG(5.7) event simulation package, without any generator-level cut. These events were also passed through DØGEANT (v3.15) using SHOWERLIBRARY and DØRECO (v12.21).

3. $Z \rightarrow \tau\tau \rightarrow ee$

For assessing the $Z \rightarrow \tau\tau \rightarrow ee$ background, events were generated using ISAJET (v7.08). At the generator level, a minimum cut on the p_T of Z $>$ 25 GeV/c was used in order to increase statistics in the region where contributions to background were important. These were processed through DØGEANT (v3.14), using the SHOWERLIBRARY option and DØRECO (v12.15).

4. $WW \rightarrow ee$

For the $WW \rightarrow ee$ sample, events were generated using PYTHIA (v5.60), without any cuts at the generator level. Events were then passed through full DØGEANT (v3.14) and DØRECO (v11.19).

A summary of the Monte Carlo generation of events in this analysis is given in Table 4.3.

4.5.1 Calculation of Net Efficiency

The number of events expected from any physics process can be written as

$$< N >= \mathcal{L}.\sigma.\epsilon$$

Process	No. of events	Generator	Remark
$t\bar{t} \rightarrow ll$	101339	HERWIG 5.7	top mass 170 GeV/c^2
$WW \rightarrow ee$	2485	PYTHIA 5.6	
$Z \rightarrow \tau\tau \rightarrow ee$	9610	ISAJET 7.08	Z $P_T > 25$ GeV/c
$Z/\gamma^* \rightarrow ee$	460,000	ISAJET 7.13	Z/γ^* mass 20-60 GeV/c^2
$Z/\gamma^* \rightarrow ee$	480,000	ISAJET 7.13	Z/γ^* mass 60-120 GeV/c^2
$Z/\gamma^* \rightarrow ee$	100,000	ISAJET 7.13	Z/γ^* mass 120-250 GeV/c^2
$Z/\gamma^* \rightarrow ee$	50,000	ISAJET 7.13	Z/γ^* mass 250-500 GeV/c^2

Table 4.3: Summary of Monte Carlo events used for background estimation.

where $< N >$ is the number of events for luminosity $\mathcal{L}$ (96 pb^{-1} for this analysis) and cross-section σ. The net detection efficiency ϵ, can be expressed as

$$\epsilon = \epsilon_{trig}.\epsilon_{kin}.\epsilon_{el\_id}$$

where ϵ_{trig} is the trigger efficiency for the events which pass the offline cuts and ϵ_{kin} is the offline cut efficiency and ϵ_{el_id} is the electron identification efficiency described earlier.

As the efficiencies for electron identification are different for CC and EC we first count the number of events which pass all the kinematic cuts and have either two electrons in CC (N_{cc}) or two electrons in EC (N_{ee}) or one electron in CC and another in EC (N_{ce}).

If the number of generated events is N, then the kinematic efficiency for events with both the electrons in CC can be written as $\epsilon_{cc}^{kin} = N_{cc}/N$
The net efficiency is therefore given by

$\epsilon_{cc} = \epsilon_{cc}^{kin}.\epsilon_{el-id}^{cc}(1).\epsilon_{el-id}^{cc}(2).\epsilon_{trig}.$
where (1) and (2) are the indices for the two electrons. ϵ_{ee} and ϵ_{ce} are also found in a similar manner.

The net efficiency over the full detector volume is given by
$\epsilon = \epsilon_{cc} + \epsilon_{ee} + \epsilon_{ce}$

and is shown in Table 4.4 for various physics processes.

Background Processes	Net Efficiency (in %) ($\epsilon_{trig}.\epsilon_{kin}.\epsilon_{el\_id}$)
$DY \rightarrow ee$ ($20 < M_{ee} < 60$)	$0.00025 \pm 0.00016 \pm 0.0003$
$DY \rightarrow ee$ ($60 < M_{ee} < 120$)	$0.00091 \pm 0.00043 \pm 0.0004$
$DY \rightarrow ee$ ($120 < M_{ee} < 250$)	$0.01834 \pm 0.00374 \pm 0.003$
$Z \rightarrow \tau\tau \rightarrow ee$	$0.1028 \pm 0.0284 \pm 0.02$
$t\bar{t} \rightarrow ll$	$0.2280 \pm 0.0254 \pm 0.03$

Table 4.4: Net efficiency for various background processes.

4.5.2 Background Cross sections

Drell-Yan Process

Because ISAJET uses leading order calculation for cross-sections, Drell_Yan cross-section values given by it are multiplied by a scale factor of 1.7 ± 0.1. This scale factor was obtained [99] by normalising the observed number of events at the Z-peak. Values of ISAJET cross-sections for four different invariant mass ranges (m_{ee}) are given in Table 4.5.

Invariant mass range (GeV)	Cross-section (pb)
20-60	145.4
60-120	201.9
120-250	2.13
250-500	0.112

Table 4.5: Drell-Yan cross-sections (as given by ISAJET) for different m_{ee} ranges.

$Z \rightarrow \tau\tau \rightarrow ee$

As mentioned earlier the sample used for studying this background was generated for Z bosons with $P_T \geq 25$ GeV. According to the DØ measurement of the P_T distribution of Z, 13% of the total cross-section is for events with $P_T \geq 25$ GeV. Thus, the effective cross-section for this process is:

(σ for $p\overline{p} \rightarrow Z \rightarrow \tau\tau$)$\times$ (B.R of $\tau\tau \rightarrow ee$)$\times$(fraction of Z with $P_T \geq 25$ GeV).

Using the DØ measured value for the cross-section as $210 \pm 0.003 \pm 0.003$ pb and the SM value for the branching ratio as 2.89 %, we find the effective cross-section as 0.79 ± 0.04 pb.

$t\bar{t} \rightarrow ll$

The total measured cross-section for top quark production is 5.5 ± 1.8 pb [100]. As the final state contains e's or μ's (which may come directly or from the decay of τ) the relevant branching ratio is 6.85%. This makes the effective cross-section for $top \rightarrow ll$ as $0.377 \pm .123$ pb.

$WW \rightarrow ee$

Taking the theoretical WW production cross-section [101] as 10 pb and the branching ratio for $WW \rightarrow ee$ as 1.23%, the effective cross-section for this process is 0.123 pb. No events survive the cuts from this Monte Carlo sample and the background from this process is taken as 0.

4.5.3 Instrumental Background

The instrumental background arises mainly from misidentification of jets as electrons. This is due to fluctuations in the energy deposition patterns of jets, and is difficult to estimate by simulations. Collider data were therefore used for this purpose.
First, we estimate the probability that a jet can be misidentified as an isolated electron, and then calculate the number of events that can mimic the signal.

Probability that a jet mimics an electron:

We count the number of electrons (N_{el}) that satisfy the quality criteria in events that have passed the JET_MULTI trigger, and have at least 4 jets within the fiducial volume. Events with more than one good electron are discarded as possible $Z \rightarrow ee$ events. We then count the number of jets (N_{jets}) in a sample in which there are at least 5 jets (counting electrons also as jets). Here it is assumed that all the energetic electrons of good quality in multijet samples are not electrons, but rather hadronic jets misidentified as electrons. The misidentification probability is then obtained from $\frac{N_{el}}{N_{jets}}$, separately for CC & EC, as well as for different E_T thresholds. As seen from Table 4.6, these probabilities are different for CC jets and EC jets, but are quite stable with respect to E_T thresholds.
The probability of a jet to mimic an electron is thus estimated as $(4.56 \pm .37) \times 10^{-4}$ in the central calorimeter and $(1.38 \pm .22) \times 10^{-3}$ in the end calorimeter.

E_T threshold (in GeV)	CC	EC
10	$(4.19 \pm 0.1) \times 10^{-4}$	$(1.44 \pm 0.03) \times 10^{-3}$
15	$(4.13 \pm 0.1) \times 10^{-4}$	$(1.61 \pm 0.03) \times 10^{-3}$
20	$(4.4 \pm 0.22) \times 10^{-4}$	$(1.26 \pm 0.05) \times 10^{-3}$
25	$(5.0 \pm 0.4) \times 10^{-4}$	$(1.16 \pm 0.1) \times 10^{-3}$

Table 4.6: Probability of a jet appearing to be an electron in different parts of the calorimeter and for different E_T thresholds.

Number of events that mimic the signal:

A data set was defined from events that passed the JET_MULTI trigger, and had $H_T \geq 150$ GeV. For each event, we consider the jet combinations that do not have an invariant mass between 76-106 GeV/c^2. These two jets are required to have $\mid \eta \mid \leq 1.1$ or $1.5 \leq \mid \eta \mid \leq 2.5$ with one of them having $E_T \geq 15$ GeV while the other $E_T \geq 10$ GeV. We require that at least 4 additional jets satisfy the quality and kinematic cuts for jets in the event. Since a combination satisfying all these requirements may simulate the signal, a weight is assigned to this combination, which is simply the product of the individual electron-misidentification probabilities of the two jets. The sum of all the weights for the valid combinations is the expected background.

4.5.4 Estimation of Uncertainty

The following sources of errors have been considered in the estimation of the background contributions from various sources.

(1) Statistical error due to the finite size of the Monte Carlo sample, and the error due to the uncertainties in the electron id efficiencies.

(2) Systematic error due to the jet energy scale uncertainties. This is estimated by analysing the Monte Carlo events with nominal, high (one standard deviation higher than the nominal) and low (one standard deviation lower than the nominal) jet energy scale correction (jet energy scale correction has been discussed in 3.3.2). Difference in the results between high and nominal correction is the positive part of the error and that between nominal and low correction is the negative part of the error.

(3) Wherever we have used the experimentally measured cross sections, the errors in their

measurement is propagated as systematic error.

4.5.5 Background summary

Table 4.7 shows the breakdown of background contributions from various sources and their uncertainties. The first error is statistical and the second one is systematic, which includes uncertainties in the jet energy scale as well as in the values of cross sections.

Background Processes	Net Efficiency (in %)	Effective cross-section (in pb)	Expected Contribution to 96 pb^{-1}
$DY \rightarrow ee$ $(20 < M_{ee} < 60)$	$0.00025 \pm 0.00016 \pm 0.0003$	247 ± 14	$0.06 \pm 0.04 \pm 0.07$
$DY \rightarrow ee$ $(60 < M_{ee} < 120)$	$0.00091 \pm 0.00043 \pm 0.0004$	343 ± 20	$0.3 \pm 0.15 \pm 0.13$
$DY \rightarrow ee$ $(120 < M_{ee} < 250)$	$0.01834 \pm 0.00374 \pm 0.003$	$3.62 \pm .21$	$0.06 \pm 0.01 \pm 0.02$
$DY \rightarrow ee$ Total			$0.42 \pm 0.15 \pm 0.16$
$Z \rightarrow \tau\tau \rightarrow ee$	$0.1028 \pm .0284 \pm 0.02$	0.79 ± 0.04	$0.08 \pm 0.02 \pm 0.02$
$t\bar{t} \rightarrow ll$	$0.02280 \pm 0.0254 \pm 0.030$	0.377 ± 0.123	$0.08 \pm 0.01 \pm 0.03$
Fake			1.27 ± 0.24
Total			$1.8 \pm 0.2 \pm 0.3$

Table 4.7: Summary of background studies.

4.6 Background Consistency check

In order to check the validity of the background modeling, different sets of cuts are devised by dropping some of the cuts and the effect of those on data and background estimation are studied.

In all sets there should be at least 2 electrons, one with $E_T > 15$ GeV and another with $E_T > 10$ GeV. Jets are counted if they have $E_T \geq 15$ GeV and the invariant mass is outside the Z window (76-106 GeV/c^2) chosen for this analysis.

Set 1: 3 or more jets , invariant mass cut, and H_T >150 GeV.
Set 2: 3 or more jets, no invariant mass cut, and H_T >150 GeV.
Set 3: 4 or more jets.
As seen from Table 4.8, there is good agreement between data and background estimates

Process	Set 1	Set 2	Set3
$WW \to ee$	0.006 ± 0.003	0.006 ± 0.003	0
$Z \to \tau\tau \to ee$	0.33 ± 0.06	0.35 ± 0.06	0.11 ± 0.02
$t\bar{t} \to ll$	0.38 ± 0.13	0.51 ± 0.17	0.10 ± 0.04
$DY \to ee$	2.7 ± 0.5	17.1 ± 5.1	3.3 ± 1.1
QCD fake	2.1 ± 0.38	2.5 ± 0.45	1.4 ± 0.3
Total	5.51 ± 0.65	20.5 ± 5.1	4.9 ± 1.14
Data	10	22	6

Table 4.8: Comparison of expected background and number of events observed in the data for different sets of cuts.

under different sets of cuts. This implies that a) there is very little, if any, R-parity violating signal in data and b) the backgrounds are modeled reasonably well.

4.7 Summary

After analysing the data and estimating the background contribution from various sources we find that 2 events survive all our analysis requirements and we expect $1.8 \pm 0.2 \pm 0.3$ such events from various background sources. We therefore see no significant excess of events above the expected background. In the next chapter we concentrate on interpreting this null result in the framework of R-parity violating SUSY models.

Chapter 5

Results

In the previous chapter we have shown that there is no evidence of excess of events in the dielectron and multijet final states over the estimated background events in our data. This was further confirmed by analysis of the data and the backgrounds using a set of loose cuts. In this chapter we will present an interpretation of this null result in the SUGRA framework.

5.1 Simulation of Signal

Although it is desirable to make the search for supersymmetry as model independent as possible, realistically, it is necessary to resort to some specific model in order to reduce the number of free parameters to a phenomenologically tractable level. We have chosen the SUGRA model for this purpose. A brief discussion of it is given in Chapter 1, but to recapitulate, it has the following five free parameters:

- m_0, the common mass for scalar fermions at the unification scale
- $m_{1/2}$, the common mass for all gauginos at the unification scale
- $tan(\beta)$, the ratio of the vacuum expectation values of the two Higgs doublets
- A_0, the common trilinear coupling constant at the unification scale
- $sign(\mu)$, the Higgsino mixing parameter.

Out of these five parameters, A_0 affects only the third generation sparticle masses. Consequently, once the sign of μ and a value for $tan(\beta)$ is chosen, there will be only two free parameters, i.e., m_0 and $m_{1/2}$, and the results of a supersymmetric particle search in this model can be presented in a two dimensional parameter space.

Events are generated at different values of m_0 and $m_{1/2}$, keeping A_0, $sign(\mu)$ and $tan(\beta)$ fixed at 0, -1 and 2 respectively. These are the same values as used in current SUSY searches at DØ. Events are generated using ISAJET, a standard event generator for hadron colliders. Within ISAJET, the calculation of the masses, cross-sections and branching ratios for decays of supersymmetric particles are done by a program called ISASUSY [102].
In ISAJET the production of sparticles and their subsequent decays follow the steps described below:

- The masses of all the sparticles and Higgs particles are calculated.
- Depending on the masses of sparticles and the gaugino and Higgsino contents of charginos and neutralinos, the decay modes and branching ratios are determined.
- $2 \rightarrow 2$ sparticle production cross-sections of all SUSY processes are calculated in the lowest order (LO) perturbation theory.
- A primary hard scattering is generated according to the cross-sections.
- QCD radiative corrections are added to initial and final state particles.
- Partons are fragmented into hadrons and the decays of hadrons with short lifetime (10^{-12} second) are taken into account.
- Underlying events are modeled assuming them to be identical to the minimum bias events.
- Events are finally written to an output file in the ZEBRA format useful for detector simulation.

Because of a change in the DØ program library during the analysis, events for about 70 points in the $m_0 - m_{1/2}$ plane were generated using ISAJET version 7.13, while for the remaining points we used version 7.22. We confirmed that results obtained are not sensitive to this change by comparing them for a few representative values of m_0 and $m_{1/2}$.

The R-parity violating SUSY option is not available in ISAJET, and the desired decay modes and branching ratios of the LSP were therefore added separately. The branching ratio for LSP decay into a charged lepton mode or neutrino mode depends on the composition of the LSP, which in turn depends on the input parameters of SUGRA. In this analysis, we added a subroutine in ISAJET that uses the composition of the LSP in calculating the branching ratios. This is based on the following set of equations [103]:

The 4 neutralino states $\tilde{\chi}_i^0$ (i=1,4), can be written in terms of the 4 interaction states $\tilde{B}$ [the U(1) gaugino], $\tilde{W}_3$ [the neutral component of SU(2) gaugino] and the two neutral higgsinos $\tilde{H}_1^0$, $\tilde{H}_2^0$ as

$$\tilde{\chi}_i^0 = N_{i1}\tilde{B} + N_{i2}\tilde{W}^3 + N_{i3}\tilde{H}_1^0 + N_{i4}\tilde{H}_2^0 \tag{5.1}$$

Where N_{i1}, N_{i2}, N_{i3}, N_{i4} are obtained by diagonalising the neutralino mixing matrix

$$\begin{pmatrix} M_1 & 0 & -m_Z sin\theta_W cos\beta & m_Z sin\theta_W sin\beta \\ 0 & M_2 & m_Z cos\theta_W cos\beta & -m_Z cos\theta_W sin\beta \\ -m_Z sin\theta_W cos\beta & m_Z cos\theta_W cos\beta & 0 & -\mu \\ m_Z sin\theta_W sin\beta & -m_Z cos\theta_W sin\beta & -\mu & 0 \end{pmatrix}$$

Now the ratio of the decay widths of LSP into charged lepton mode and neutrino mode is given by

$$\frac{\Gamma_{\tilde{\chi}_1^0 \to e^- c\bar{s}}}{\Gamma_{\tilde{\chi}_1^0 \to \overline{\nu_e} s\bar{s}}} = \frac{(A^e_{\tilde{\chi}_1^0})^2 + (A^u_{\tilde{\chi}_1^0})^2 + (B^d_{\tilde{\chi}_1^0})^2 - A^e_{\tilde{\chi}_1^0}A^u_{\tilde{\chi}_1^0} + A^e_{\tilde{\chi}_1^0}B^d_{\tilde{\chi}_1^0} + A^u_{\tilde{\chi}_1^0}B^d_{\tilde{\chi}_1^0}}{(A^\nu_{\tilde{\chi}_1^0})^2 + (A^d_{\tilde{\chi}_1^0})^2 + (B^d_{\tilde{\chi}_1^0})^2 - A^\nu_{\tilde{\chi}_1^0}A^d_{\tilde{\chi}_1^0} + A^\nu_{\tilde{\chi}_1^0}B^d_{\tilde{\chi}_1^0} + A^d_{\tilde{\chi}_1^0}B^d_{\tilde{\chi}_1^0})} \tag{5.2}$$

Where

$A^e_{\tilde{\chi}_1^0} = -\frac{g'}{\sqrt{2}}N_{11} - \frac{g}{\sqrt{2}}N_{12}, \quad A^\nu_{\tilde{\chi}_1^0} = -\frac{g'}{\sqrt{2}}N_{11} + \frac{g}{\sqrt{2}}N_{12}$

$A^u_{\tilde{\chi}_1^0} = \frac{g'}{3\sqrt{2}}N_{11} + \frac{g}{\sqrt{2}}N_{12}, \quad A^d_{\tilde{\chi}_1^0} = \frac{g'}{3\sqrt{2}}N_{11} - \frac{g}{\sqrt{2}}N_{12}$

$B^u_{\tilde{\chi}_1^0} = \frac{4g'}{3\sqrt{2}}N_{11}, \quad B^d_{\tilde{\chi}_1^0} = -\frac{2g'}{3\sqrt{2}}N_{11}$

In Table 5.1, we show a few values of branching ratio (BR) for LSP decaying into a charged lepton:

At the time of event generation, one has to specify a particular decay mode. λ'_{122} was chosen for this purpose, but this analysis should be equally valid for any of the λ'_{1jk} couplings (where j=1, 2 and k=1, 2, 3), as the final states are similar. The case j=3 is not allowed by the large top quark mass for the charged leptonic decay mode of the LSP.

At first we studied the sensitivity of our search over the $m_0 - m_{1/2}$ plane using generator level Monte Carlo events. From this we identified a region in the parameter space where detailed study needs to be done. The generated events in that region are written to a ZEBRA file, provided they have two or more electrons with $E_T > 5$ GeV, and three or

m_0	$m_{1/2}$	BR
50	70	.83
160	80	.78
60	70	.83
70	70	.83
80	80	.80

$$BR = \frac{\Gamma_{\tilde{\chi}_1^0 \to e^- c\bar{s}}}{\Gamma_{\tilde{\chi}_1^0 \to \overline{\nu_e} s\bar{s}} + \Gamma_{\tilde{\chi}_1^0 \to e^- c\bar{s}}}$$

Table 5.1: Branching Ratio of LSP decaying to a charged lepton.

more parton jets with $E_T > 5$ GeV. This selection at the generator level is applied so as to minimise the overall use of CPU time. Events are subsequently passed through the DØ detector simulation package DØGEANT, the trigger simulator TRIGSIM, and the reconstruction package DØRECO. In the DØGEANT simulation, the SHOWERLIBRARY option is used to further reduce the usage of CPU time. So far, events have been generated and analysed for over 100 points in the m_0-$m_{1/2}$ plane as shown in Fig. 5.1.

5.2 Signal Efficiencies

The procedure for the determination of signal efficiency is the same as that of Standard Model background processes, as described in the last chapter. Since, all types of SUSY events have been generated, these efficiencies include the *net* branching ratio to dielectron channels. Table 5.2 gives values for efficiency times branching ratio to dielectron channels and the expected number of events for 96 pb^{-1} luminosity for all the points at which events were generated.

5.3 Contributions of sub-processes to the signal

While generating the events all possible SUSY processes are considered. So, it is of interest to see the fractional population of events due to different subprocesses passing all the analysis cuts. This is shown in the Table 5.3 for a few representative points.
It can be seen from Table 5.3 that more than 50 % of all events, which satisfy the cuts,

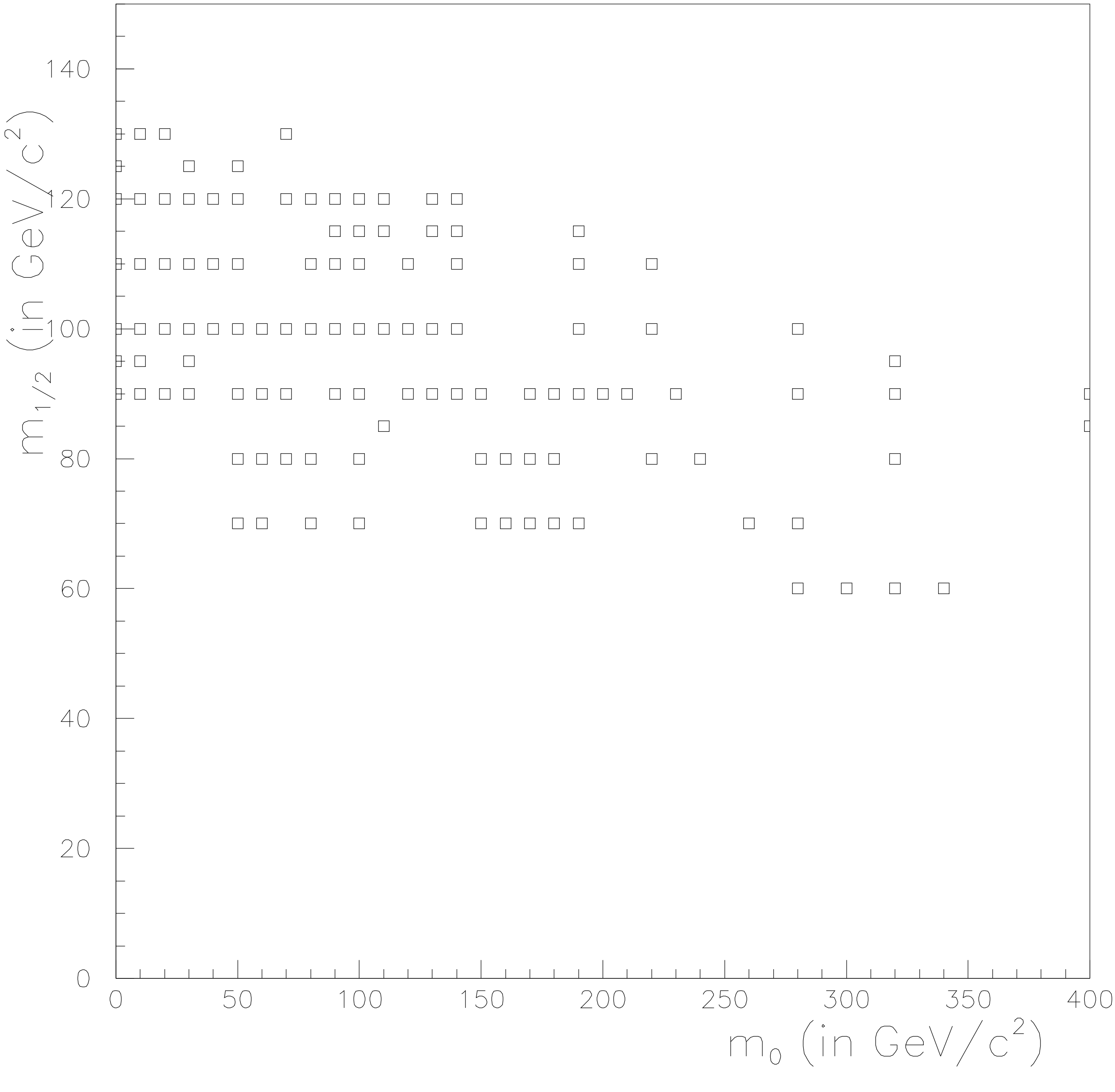

Figure 5.1: Points in the $m_0 - m_{1/2}$ plane at which Monte Carlo events were generated.

m_0	$m_{1/2}$	$\epsilon B.R.(\%)$	$< N >$	m_0	$m_{1/2}$	$\epsilon B.R.(\%)$	$< N >$
0	120	$1.866 \pm 0.221^{+0.068}_{-0.050}$	4.1 ± 0.5	0	95	$1.624 \pm 0.192^{+0.062}_{-0.006}$	14.7 ± 1.7
0	100	$1.747 \pm 0.209^{+0.093}_{-0.056}$	10.9 ± 1.3	0	110	$1.783 \pm 0.206^{+0.093}_{-0.099}$	5.8 ± 0.7
0	125	$1.962 \pm 0.233^{+0.050}_{-0.075}$	3.5 ± 0.4	0	130	$1.835 \pm 0.211^{+0.043}_{-0.105}$	2.6 ± 0.3
0	90	$0.736 \pm 0.101^{+0.043}_{-0.019}$	24.4 ± 3.4	10	110	$1.849 \pm 0.215^{+0.043}_{-0.074}$	6.2 ± 0.7
10	95	$1.644 \pm 0.189^{+0.068}_{-0.056}$	14.0 ± 1.6	10	120	$1.765 \pm 0.209^{+0.099}_{-0.044}$	3.8 ± 0.4
10	100	$1.788 \pm 0.201^{+0.049}_{-0.006}$	10.9 ± 1.2	10	90	$0.945 \pm 0.125^{+0.025}_{-0.062}$	20.8 ± 2.8
10	130	$1.920 \pm 0.223^{+0.099}_{-0.012}$	2.7 ± 0.3	20	130	$2.140 \pm 0.248^{+0.000}_{-0.075}$	2.9 ± 0.3
20	100	$1.589 \pm 0.190^{+0.112}_{-0.031}$	8.8 ± 1.0	20	120	$1.867 \pm 0.217^{+0.019}_{-0.136}$	3.9 ± 0.4
20	100	$1.589 \pm 0.190^{+0.112}_{-0.031}$	8.8 ± 1.0	20	90	$1.718 \pm 0.205^{+0.012}_{-0.106}$	19.3 ± 2.3
20	110	$1.851 \pm 0.212^{+0.130}_{-0.019}$	5.9 ± 0.7	30	100	$1.853 \pm 0.214^{+0.056}_{-0.037}$	9.4 ± 1.1
30	125	$1.987 \pm 0.235^{+0.168}_{-0.075}$	3.0 ± 0.4	30	90	$1.579 \pm 0.185^{+0.136}_{-0.043}$	14.4 ± 1.7
30	115	$1.787 \pm 0.213^{+0.137}_{-0.050}$	4.3 ± 0.5	30	110	$1.912 \pm 0.221^{+0.143}_{-0.019}$	5.7 ± 0.7
30	120	$2.078 \pm 0.236^{+0.074}_{-0.006}$	3.9 ± 0.4	30	95	$1.879 \pm 0.218^{+0.031}_{-0.087}$	12.4 ± 1.4
40	110	$2.009 \pm 0.229^{+0.056}_{-0.056}$	5.5 ± 0.6	40	100	$1.811 \pm 0.216^{+0.081}_{-0.031}$	8.4 ± 1.0
40	120	$1.842 \pm 0.219^{+0.093}_{-0.056}$	3.3 ± 0.4	50	90	$1.582 \pm 0.185^{+0.074}_{-0.056}$	11.5 ± 1.3
50	80	$1.411 \pm 0.163^{+0.043}_{-0.006}$	19.6 ± 2.3	50	125	$1.937 \pm 0.219^{+0.093}_{-0.124}$	2.6 ± 0.3
50	110	$1.747 \pm 0.208^{+0.075}_{-0.019}$	3.3 ± 0.4	50	120	$1.762 \pm 0.216^{+0.075}_{-0.044}$	2.9 ± 0.4
50	70	$1.289 \pm 0.158^{+0.019}_{-0.006}$	35.8 ± 4.4	50	100	$1.764 \pm 0.208^{+0.043}_{-0.037}$	7.3 ± 0.9
60	80	$1.484 \pm 0.179^{+0.056}_{-0.043}$	6.6 ± 0.8	60	120	$1.483 \pm 0.174^{+0.111}_{-0.062}$	2.2 ± 0.3
60	90	$1.536 \pm 0.177^{+0.006}_{-0.062}$	10.3 ± 1.2	60	100	$1.512 \pm 0.184^{+0.006}_{-0.050}$	6.0 ± 0.7
60	70	$1.207 \pm 0.148^{+0.006}_{-0.056}$	30.7 ± 3.8	70	80	$0.858 \pm 0.111^{+0.000}_{-0.037}$	10.3 ± 1.3
70	130	$1.539 \pm 0.190^{+0.118}_{-0.131}$	1.5 ± 0.2	70	115	$2.434 \pm 0.269^{+0.074}_{-0.149}$	4.3 ± 0.5
70	100	$1.148 \pm 0.145^{+0.056}_{-0.074}$	4.2 ± 0.5	70	90	$0.986 \pm 0.122^{+0.000}_{-0.043}$	6.2 ± 0.8
70	120	$1.281 \pm 0.161^{+0.075}_{-0.006}$	1.8 ± 0.2	70	70	$0.820 \pm 0.107^{+0.000}_{-0.031}$	19.5 ± 2.5
80	80	$1.959 \pm 0.224^{+0.074}_{-0.025}$	20.9 ± 2.4	80	100	$0.902 \pm 0.117^{+0.019}_{-0.049}$	3.1 ± 0.4
80	70	$1.665 \pm 0.194^{+0.111}_{-0.056}$	36.1 ± 4.2	80	110	$1.053 \pm 0.133^{+0.006}_{-0.068}$	2.2 ± 0.3
80	120	$1.002 \pm 0.128^{+0.043}_{-0.049}$	1.4 ± 0.2	90	90	$2.026 \pm 0.226^{+0.049}_{-0.056}$	11.3 ± 1.3
90	120	$2.241 \pm 0.253^{+0.124}_{-0.000}$	2.9 ± 0.3	90	110	$2.213 \pm 0.254^{+0.037}_{-0.006}$	4.3 ± 0.5
90	115	$2.293 \pm 0.266^{+0.100}_{-0.087}$	3.7 ± 0.4	90	100	$2.045 \pm 0.238^{+0.062}_{-0.068}$	6.6 ± 0.8
100	115	$2.262 \pm 0.255^{+0.043}_{-0.155}$	3.5 ± 0.4	100	110	$2.188 \pm 0.239^{+0.062}_{-0.080}$	4.0 ± 0.4
100	90	$1.964 \pm 0.221^{+0.019}_{-0.080}$	10.2 ± 1.1	100	100	$2.195 \pm 0.244^{+0.025}_{-0.037}$	6.5 ± 0.7
100	80	$1.894 \pm 0.211^{+0.049}_{-0.031}$	18.0 ± 2.0	100	120	$2.314 \pm 0.265^{+0.093}_{-0.180}$	2.8 ± 0.3
100	70	$2.053 \pm 0.235^{+0.105}_{-0.025}$	38.0 ± 4.3	110	85	$2.106 \pm 0.237^{+0.050}_{-0.019}$	14.1 ± 1.6
110	100	$2.269 \pm 0.255^{+0.118}_{-0.074}$	6.6 ± 0.7	110	120	$2.437 \pm 0.267^{+0.148}_{-0.173}$	2.9 ± 0.3
110	115	$2.382 \pm 0.266^{+0.093}_{-0.118}$	3.5 ± 0.4	120	100	$2.041 \pm 0.226^{+0.179}_{-0.000}$	5.7 ± 0.6
120	90	$2.101 \pm 0.230^{+0.086}_{-0.025}$	10.1 ± 1.1	120	110	$2.194 \pm 0.243^{+0.099}_{-0.025}$	3.9 ± 0.4

Table 5.2: Efficiency$\times$B.R(%) and the expected event yield $< N >$ for 96 pb^{-1} luminosity at various signal points in the $m_0 - m_{1/2}$ parameter space.

m_0	$m_{1/2}$	$\epsilon B.R.(\%)$	$< N >$	m_0	$m_{1/2}$	$\epsilon B.R.(\%)$	$< N >$
130	90	$1.957 \pm 0.222^{+0.062}_{-0.050}$	24.8 ± 2.8	130	100	$2.125 \pm 0.248^{+0.150}_{-0.019}$	5.7 ± 0.7
130	115	$2.223 \pm 0.251^{+0.118}_{-0.012}$	3.0 ± 0.3	130	120	$2.471 \pm 0.272^{+0.161}_{-0.099}$	2.8 ± 0.3
140	120	$2.370 \pm 0.272^{+0.075}_{-0.068}$	2.5 ± 0.3	140	110	$2.293 \pm 0.257^{+0.124}_{-0.130}$	3.7 ± 0.4
140	115	$2.201 \pm 0.248^{+0.105}_{-0.043}$	2.9 ± 0.3	140	90	$2.020 \pm 0.225^{+0.080}_{-0.006}$	8.4 ± 0.9
140	100	$1.964 \pm 0.231^{+0.044}_{-0.093}$	5.1 ± 0.6	150	90	$1.950 \pm 0.218^{+0.068}_{-0.037}$	7.8 ± 0.9
150	70	$2.060 \pm 0.231^{+0.012}_{-0.025}$	26.1 ± 2.9	150	80	$2.039 \pm 0.234^{+0.112}_{-0.043}$	14.2 ± 1.6
160	80	$1.899 \pm 0.215^{+0.031}_{-0.037}$	12.4 ± 1.4	160	70	$1.943 \pm 0.222^{+0.012}_{-0.099}$	23.2 ± 2.6
170	90	$1.884 \pm 0.222^{+0.106}_{-0.124}$	6.9 ± 0.8	170	70	$1.809 \pm 0.202^{+0.025}_{-0.043}$	20.1 ± 2.2
170	80	$2.123 \pm 0.235^{+0.031}_{-0.105}$	13.2 ± 1.5	180	90	$1.851 \pm 0.215^{+0.093}_{-0.043}$	6.5 ± 0.8
180	70	$1.824 \pm 0.210^{+0.025}_{-0.049}$	19.3 ± 2.2	180	80	$1.742 \pm 0.199^{+0.056}_{-0.068}$	10.3 ± 1.2
190	115	$2.216 \pm 0.248^{+0.124}_{-0.019}$	2.6 ± 0.3	190	90	$1.721 \pm 0.199^{+0.056}_{-0.019}$	5.9 ± 0.7
190	100	$1.841 \pm 0.207^{+0.086}_{-0.031}$	4.0 ± 0.4	190	110	$2.088 \pm 0.231^{+0.062}_{-0.037}$	2.9 ± 0.3
190	70	$1.118 \pm 0.143^{+0.012}_{-0.019}$	10.5 ± 1.3	200	90	$1.739 \pm 0.201^{+0.062}_{-0.037}$	5.8 ± 0.7
210	90	$1.500 \pm 0.174^{+0.099}_{-0.012}$	4.8 ± 0.6	220	110	$1.642 \pm 0.192^{+0.105}_{-0.050}$	2.2 ± 0.3
220	100	$1.668 \pm 0.195^{+0.099}_{-0.031}$	3.3 ± 0.4	220	80	$1.291 \pm 0.154^{+0.371}_{-0.074}$	6.7 ± 0.8
230	90	$1.320 \pm 0.159^{+0.062}_{-0.006}$	4.1 ± 0.5	240	80	$0.885 \pm 0.117^{+0.062}_{-0.062}$	4.4 ± 0.6
260	70	$0.761 \pm 0.103^{+0.006}_{-0.043}$	6.3 ± 0.9	280	100	$1.241 \pm 0.154^{+0.112}_{-0.037}$	2.4 ± 0.3
280	90	$1.123 \pm 0.142^{+0.025}_{-0.074}$	3.4 ± 0.4	280	70	$0.613 \pm 0.088^{+0.037}_{-0.025}$	5.1 ± 0.7
280	60	$0.521 \pm 0.080^{+0.006}_{-0.012}$	8.3 ± 1.3	320	90	$0.844 \pm 0.119^{+0.044}_{-0.044}$	2.6 ± 0.4
320	80	$0.656 \pm 0.093^{+0.043}_{-0.000}$	3.2 ± 0.5	320	60	$0.407 \pm 0.066^{+0.019}_{-0.000}$	6.7 ± 1.1

Table 5.2 (cont'd.)

m_0	$m_{1/2}$	$\tilde{q}-\tilde{q}$	$\tilde{g}-\tilde{g}$	$\tilde{q}-\tilde{g}$	$\tilde{W},\tilde{Z}$	$\tilde{l}-\tilde{l}$	others
0	120	37.05	0.94	9.10	21.82	18.05	13.03
120	110	34.60	2.03	10.85	22.52	17.23	12.75
280	90	8.69	12.76	11.72	52.48	.17	14.18
220	100	16.90	6.66	13.19	48.91	.13	14.21

Table 5.3: Relative contribution of various subprocesses to the signal for a few values of m_0 and $m_{1/2}$.

originate from processes other than the pair production of squarks or gluinos. This makes it mandatory to generate all types of SUSY events, for this analysis. While finding the exclusion contour we are constrained to use only the leading order cross-sections (LO, given by ISAJET) instead of the next-to-leading order (NLO) cross-sections, since the latter are available only for squark-gluino production. In general, this leads to conservative limits from the data.

5.4 Extraction of cross-section limits

In Run 1B data, corresponding to a luminosity of 96 pb^{-1}, we do not see any significant excess of events over the background. This result has been used to find the region in the parameter space which could be excluded at the 95% C.L. At various points in the $m_0 - m_{1/2}$ plane, the upper limits of the cross-section were obtained using the estimated values of signal efficiencies for that point, the estimated values of the background and the number of events observed in data. A Bayesian technique has been adopted [104] to find the cross-section limit. Here we give a brief overview of the method adopted to calculate the upper limits of the cross-section

Bayes theorem can be written as

$$P(A|BC) = \frac{P(B|AC)P(A|C)}{P(B|C)} \tag{5.3}$$

In writing this equation standard notation for probability theory has been adopted where $P(A|B)$ denotes the probability of proposition A to be true, given that proposition B is true. For a continuous variable X, $P(x|B)dx$ is the probability of X to have a value between x and $x+dx$, given the proposition B is true. Here the denominator is determined from the normalisation condition

$$\sum_{all\ A} P(A|BC) = 1 \tag{5.4}$$

To find the limit the first step is to define a model. For a counting experiment such as this analysis, the expected number of events μ, the integrated luminosity $\mathcal{L}$, the signal cross section σ, the signal efficiency ϵ and the expected number of background events b are related by

$$\mu = b + \mathcal{L}\epsilon\sigma \tag{5.5}$$

Here the first term on the right is the expected number of background events and the 2nd term is the expected number of signal events. In case of a counting experiment the probability of observing k events in the data, given an expectation value of μ, is given by the Poisson likelihood function

$$P(k|\mu, I) = \frac{e^{-\mu}.\mu^k}{k!} \tag{5.6}$$

where I denotes all the relevant prior information in the problem. From equation 5.5 and equation 5.6 one can write

$$P(k|\sigma, \mathcal{L}, \epsilon, b, I) = \frac{e^{-(b+\mathcal{L}\epsilon\sigma)}.(b + \mathcal{L}\epsilon\sigma)^k}{k!} \tag{5.7}$$

The next step will be to assign the prior probabilities for all parameters. Assuming the parameters σ, $\mathcal{L}$, ϵ and b to be independent and uncorrelated, the prior probability can be factorised and written as

$$P(\sigma, \mathcal{L}, \epsilon, b|I) = P(\sigma|I)P(\mathcal{L}, \epsilon, b|I) \tag{5.8}$$

For the signal cross section a flat prior probability is taken

$$P(\sigma|I) = \begin{cases} 1/\sigma_{max} & \text{if } 0 \leq \sigma \leq \sigma_{max} \\ 0 & \text{otherwise} \end{cases} \tag{5.9}$$

As for $\mathcal{L}$, ϵ and b we have estimation of both their mean values and the errors on them; for all of them Gaussian prior probabilities are assumed. From equation 5.7 and from our assumption of the prior, the Bayes theorem can be written as

$$P(\sigma, \mathcal{L}, \epsilon, b|k, I) \propto \frac{e^{-(b+\mathcal{L}\epsilon\sigma)}.(b + \mathcal{L}\epsilon\sigma)^k}{k!}.P(\sigma, \mathcal{L}, \epsilon, b|I) \tag{5.10}$$

where the constant of proportionality is determined from the normalisation

$$\int_0^\infty d\sigma \int_0^\infty d\mathcal{L} \int_0^1 d\epsilon \int_0^\infty db P(\sigma, \mathcal{L}, \epsilon, b|I) = 1 \tag{5.11}$$

Since we are only interested in σ, we integrate equation 5.10 over the nuisance parameters $\mathcal{L}$, ϵ and b to get the 'posterior' probability distribution for σ

$$P(\sigma|k, I) = \int_0^\infty d\mathcal{L} \int_0^1 d\epsilon \int_0^\infty P(\sigma, \mathcal{L}, \epsilon, b|k, I) \tag{5.12}$$

'Posterior' probability distribution for σ carries full information of the Bayesian analysis. The $100\beta\%$ confidence level upper limit on the cross section σ_{UL}, is defined by

$$\beta = \int_0^{\sigma_{UL}} d\sigma P(\sigma|k, I) \tag{5.13}$$

Here one interesting point to note is that if the posterior distribution for σ peaks significantly away from zero, it may be considered as a discovery.

In Table 5.4 we give the theoretical cross-section values obtained from ISAJET and the 95% C.L. cross-section upper limits obtained for the current analysis at each of the points generated.

5.5 Cross-section limits and the excluded region

In this section we will present the region in the $m_0 - m_{1/2}$ plane excluded by this analysis at 95% C.L. and discuss its important features. A point in the $m_0 - m_{1/2}$ plane is excluded if the theoretical cross-section for that point is higher than the measured 95% C.L. cross-section upper limit. The exclusion contour was found using a graphical method. For fixed values of m_0, theoretical cross-sections as well as the 95 % C.L. cross-section upper limits are plotted as a function of $m_{1/2}$. The corresponding plots for a few values of m_0 are shown in Fig. 5.2. The lower bound on $m_{1/2}$ is given by that value of $m_{1/2}$ at which the theoretical and experimental curves cross. An exclusion contour is then drawn by fitting a cubic spline through all such points of lower bounds in the $m_0 - m_{1/2}$ plane.

The exclusion contour is shown in Fig. 5.3 where the region below the thick solid line is excluded by the present analysis. The hatched region is not theoretically allowed.

m_0	$m_{1/2}$	Theoretical cross-section	95% C.L cross-section upper limit	m_0	$m_{1/2}$	Theoretical cross-section	95% C.L cross-section upper limit
0	120	2.27	3.08	0	95	9.41	3.50
0	100	6.48	3.29	0	110	3.62	3.27
0	125	1.85	2.96	0	130	1.50	3.20
0	90	34.5	7.21	10	110	3.48	3.15
10	95	8.87	3.51	10	120	2.24	3.24
10	100	6.36	3.18	10	90	22.9	6.15
10	130	1.45	2.94	20	130	1.42	2.73
20	100	5.75	3.57	20	120	2.15	3.20
20	90	11.7	3.47	20	110	3.35	3.04
30	100	5.26	3.09	30	125	1.56	2.87
30	90	9.5	3.60	30	115	2.51	3.18
30	110	3.12	2.94	30	120	1.98	2.73
30	95	6.89	3.12	40	110	2.87	2.87
40	100	4.82	3.16	40	120	1.84	3.12
50	90	7.67	3.64	50	80	14.5	3.69
50	125	1.42	3.02	50	110	2.64	3.27
50	120	1.72	3.27	50	70	28.93	4.47
50	100	4.38	3.27	60	80	13.2	3.90
60	120	1.58	3.87	60	90	6.96	3.83
60	100	4.14	3.87	60	70	26.47	4.89
70	80	12.48	6.61	70	130	1.02	3.85
70	115	1.86	2.40	70	100	3.79	5.11
70	90	6.57	5.88	70	120	1.49	4.43
80	80	11.18	2.91	80	100	3.59	6.38
80	70	22.67	3.43	80	110	2.2	5.62
80	120	1.42	5.78	90	90	5.79	2.84
90	120	1.34	2.51	90	110	2.12	2.58
90	115	1.66	2.52	90	100	3.33	2.82
100	115	1.6	2.60	100	110	1.93	2.63
100	90	5.43	2.97	100	100	3.17	2.62
100	80	9.95	3.02	100	120	1.27	2.55
100	70	19.3	2.76	110	85	7.0	2.71
110	100	3.0	2.51	110	120	1.23	2.40
110	115	1.53	2.44	120	100	2.9	2.73
120	90	5.0	2.69	120	110	1.84	2.58

Table 5.4: Theoretical cross-sections and the 95% C.L. upper limits of the cross-section for all the points at which events were generated. Theoretical cross-section values were obtained from ISAJET and the 95% C.L. cross-section upper limits were obtained for the current analysis at each of the points generated. All the cross-section values are in pb.

m_0	$m_{1/2}$	Theoretical cross-section	95% C.L cross-section upper limit	m_0	$m_{1/2}$	Theoretical cross-section	95% C.L cross-section upper limit
130	90	4.4	2.71	130	100	2.77	2.68
130	115	1.42	2.49	130	120	1.16	2.27
140	120	1.12	2.43	140	110	1.70	2.53
140	115	1.37	2.58	140	90	4.33	2.80
140	100	2.7	2.98	150	90	4.17	2.93
150	70	13.2	2.80	150	80	7.22	2.78
160	80	6.84	3.04	160	70	12.4	3.03
170	90	3.83	3.11	170	70	11.6	3.19
170	80	6.48	2.75	180	90	3.66	3.09
190	115	1.2	2.54	190	90	3.56	3.32
190	100	2.26	3.09	190	110	1.46	2.73
190	70	10.6	5.17	200	90	3.46	3.30
210	90	3.34	3.75	220	110	1.41	3.48
220	100	2.09	3.40	220	80	5.43	4.33
230	90	3.25	4.31	240	80	5.18	6.46
260	70	8.60	7.21	280	100	2.04	4.59
280	90	3.13	5.25	280	070	8.56	8.01
280	60	16.7	8.50	320	90	3.18	6.68
320	80	5.08	7.64	320	60	16.8	8.91

Table 5.4 (cont'd.)

To understand the characteristics of the exclusion contour it will be convenient to divide the $m_0 - m_{1/2}$ plane into three regions - *low m_0 region ($m_0 < 150$ GeV/c^2), intermediate m_0 region (150 GeV/c^2 < m_0 < 280 GeV/c^2) and the asymptotic region ($m_0 > 280$ GeV/c^2).*

In the low m_0 region the dominant SUSY process that contributes to the signal is pair production of squarks. As we move horizontally towards higher m_0 values, the corresponding squark mass also increases, thereby reducing the squark pair production cross-section. Hence, in this region, it is expected that the exclusion contour should follow the equal squark mass contour. This is nicely demonstrated in Fig. 5.3 where we see the exclusion contour follows the curve on which the mass of the squark is 280 GeV/c^2.

The dip in the contour near $m_0 = 60 - 80$ GeV/c^2 can be attributed to the fact that the two electrons can originate either from the decay of LSP or from any other SUSY or SM particles. In about 70 % of the cases both LSPs decay into electrons (as can be estimated from Table 5.1). Moreover, the electrons arising from the decay of LSP do not always pass the E_T cut. In such cases, however, additional electrons arising from the decay of $\tilde{\chi}_2^0$ can make the event pass this criterion. But in the region of $m_0 = 60 - 80$ GeV/c^2, sneutrino becomes lighter than the $\tilde{\chi}_2^0$ and the decay of $\tilde{\chi}_2^0$ to $\tilde{\chi}_1^0$ and neutrinos [$\tilde{\chi}_2^0 \rightarrow \nu\tilde{\nu}$; $\tilde{\nu} \rightarrow \tilde{\chi}_1^0\nu$] becomes dominant. This reduces the overall branching ratio to the dielectron final state resulting in the observed dip.

As m_0 increases further, sneutrino becomes heavier than $\tilde{\chi}_2^0$ and the branching ratio of $\tilde{\chi}_2^0$ decay to neutrino reduces. This is because such a decay can now proceed only through the exchange of a virtual sneutrino and has to compete with the corresponding decay through virtual selectrons. This again enhances the branching ratio to the dielectron final state. So the exclusion contour moves up and follows the equal squark mass contour till about $m_0 = 150$ GeV/c^2.

In the intermediate m_0 region processes like the production of gluino, $\tilde{\chi}_1^{\pm}$ and $\tilde{\chi}_2^0$ start becoming more important. As the masses of these particles do not change significantly with a change in m_0, their cross-sections also do not change with the increase of m_0 for the same $m_{1/2}$. This causes the exclusion contour to become more and more flat.

Finally, in the asymptotic region, production of squarks becomes insignificant and the exclusion contour becomes flat.

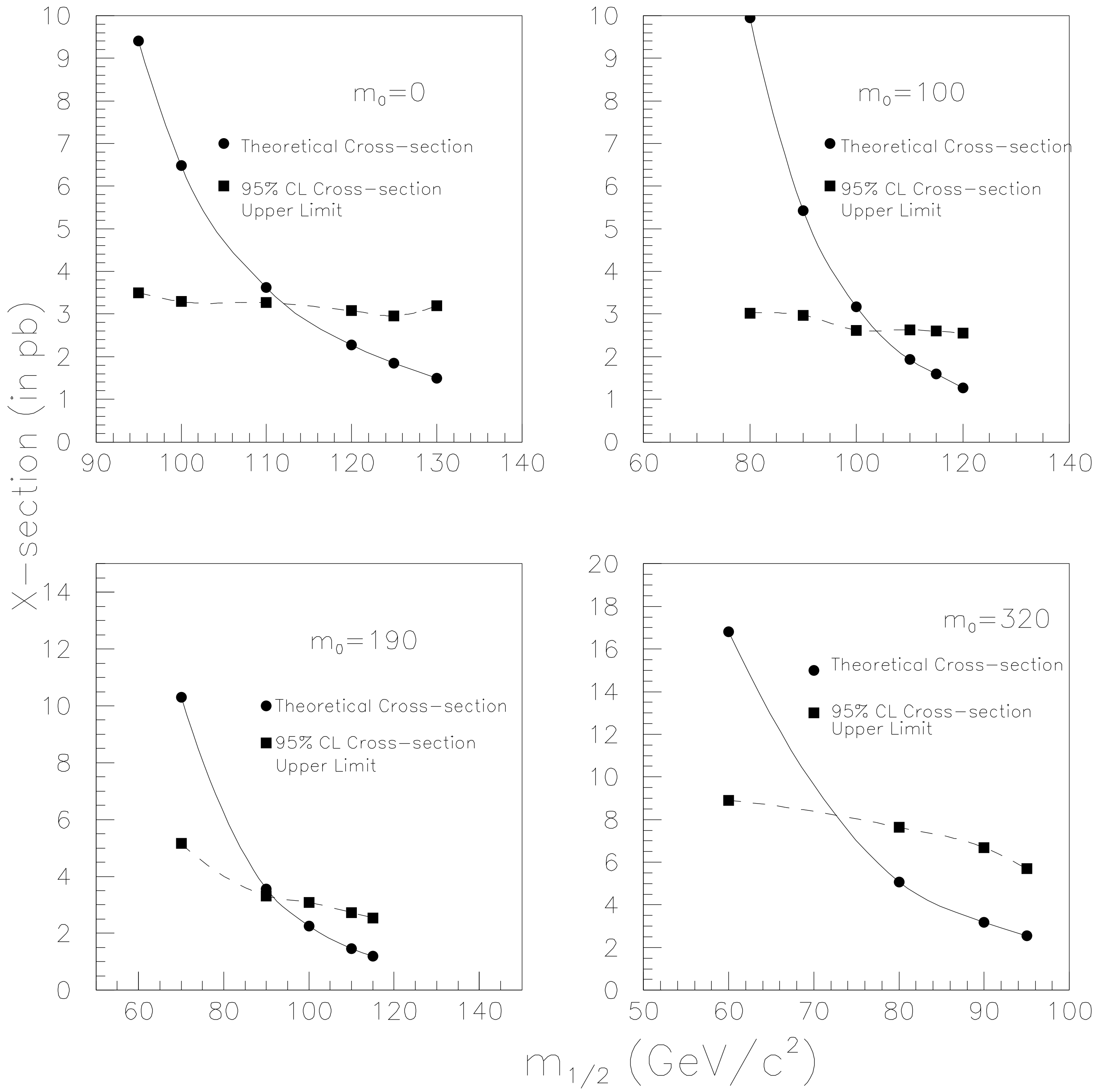

Figure 5.2: Determination of the limits on $m_{1/2}$ for different values of m_0.

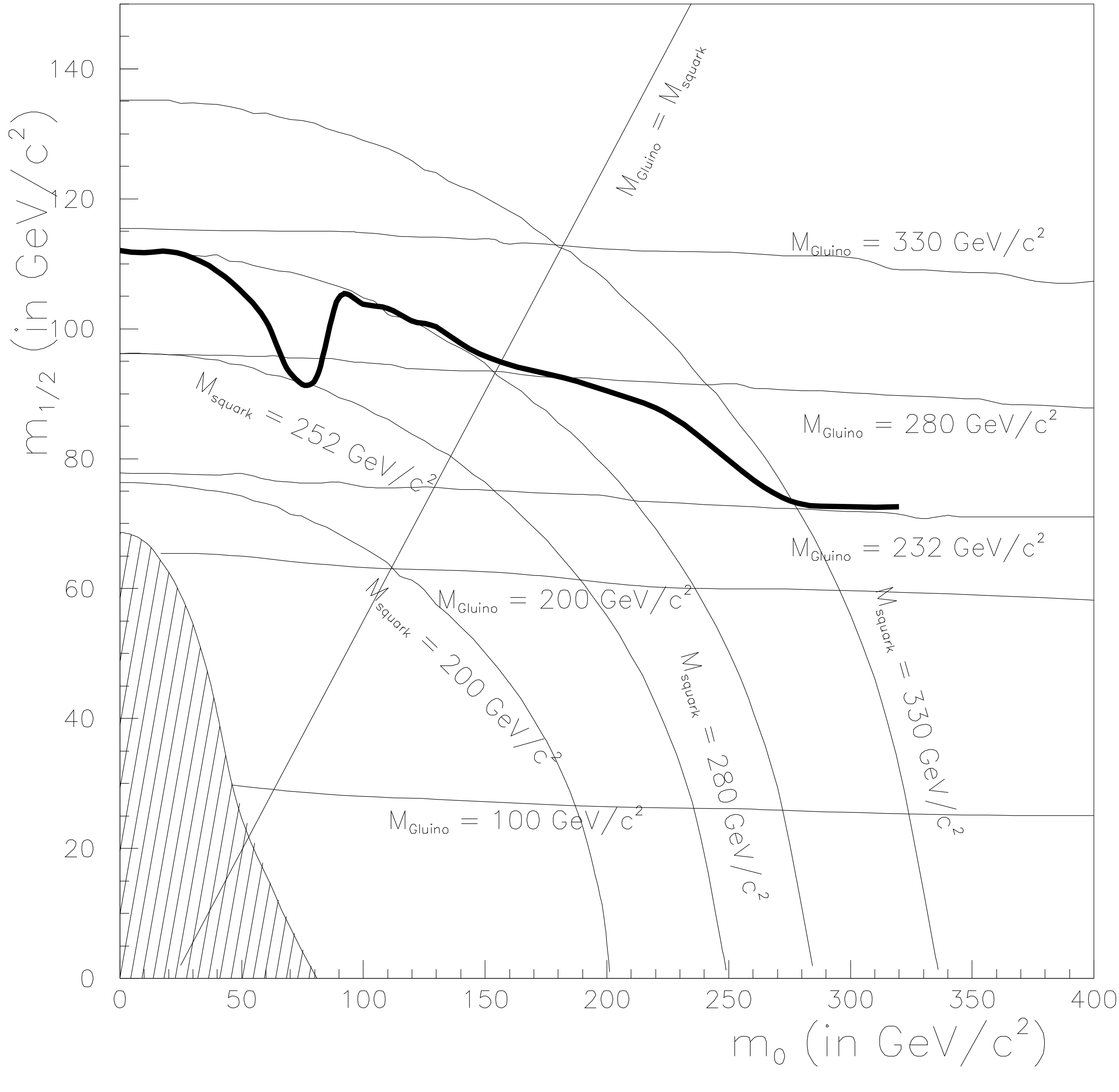

Figure 5.3: Exclusion contour in the $m_0 - m_{1/2}$ plane for $tan(\beta) = 2$, $sign(\mu) = -1$, $A_0 = 0$ and nonzero values of λ'_{1jk} (where j=1, 2 and k=1, 2, 3) coupling. The region below the bold line is excluded at 95 % C.L.

5.6 Mass Limits on SUSY particles

Masses of all supersymmetric particles can be uniquely determined once the values of the five SUGRA parameters m_0, $m_{1/2}$, $sign(\mu)$, A_0 and $tan\beta$ are specified. Thus, limits on various supersymmetric particles can be obtained from the exclusion contour in the $m_0 - m_{1/2}$ plane. Figure 5.4 shows the exclusion contour in the squark-gluino mass plane as obtained by translating the exclusion contour from the $m_0 - m_{1/2}$ plane.

It is seen from Fig. 5.3 and Fig. 5.4 that within the SUGRA framework masses of squarks below 252 GeV/c^2 and gluinos below 232 GeV/c^2 are completely ruled out for fixed values of A_0=0, $sign(\mu)$=-1, $tan(\beta)$=2 and non zero values of the λ'_{1jk} (where j=1, 2 and k=1, 2, 3) couplings. For equal masses of squarks and gluinos, the corresponding limit is 283 GeV/c^2. As seen from the Fig. 5.4, in the SUGRA framework, the gluinos cannot be much heavier compared to the squarks and hence the reach of this analysis is confined mostly to the region where the gluinos are lighter than the squarks.

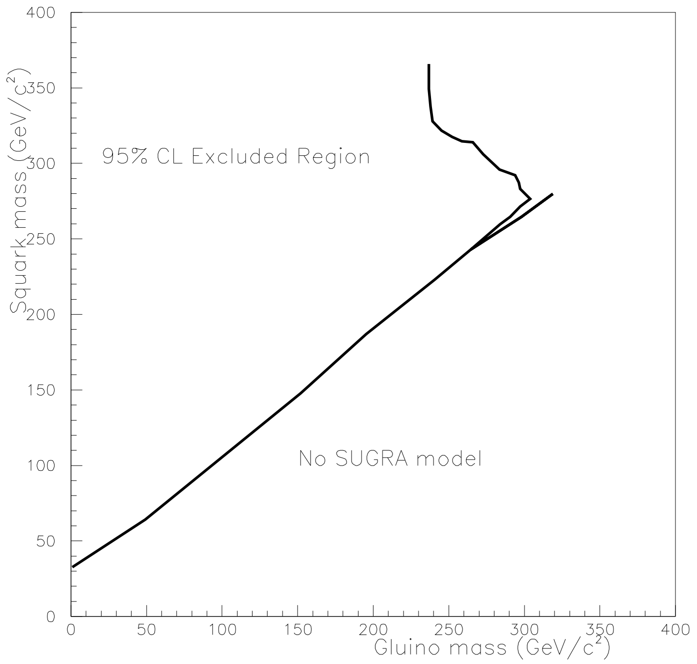

Figure 5.4: Exclusion contour in the Squark - Gluino mass plane for $tan(\beta) = 2$, $sign(\mu) = -1$, $A_0 = 0$ and nonzero values of λ'_{1jk} (where j=1, 2 and k=1, 2, 3) couplings.

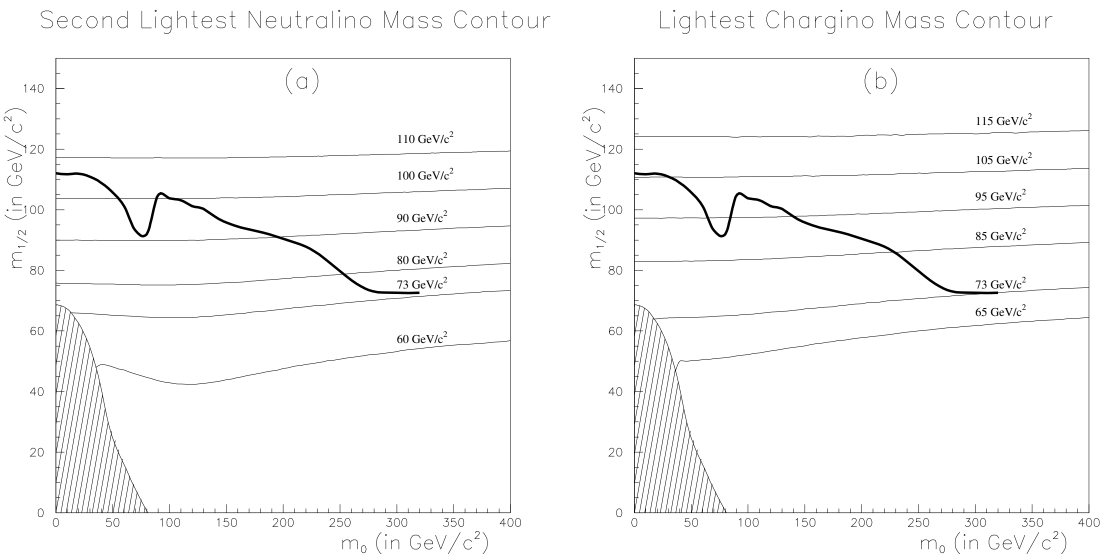

Figure 5.5: Exclusion contour in the $m_0 - m_{1/2}$ plane with (a) Second lightest Neutralino and (b) Lightest Chargino Mass contours.

Similarly, Fig. 5.5 shows the mass ranges excluded at 95% C.L. for the second lightest neutralino ($\tilde{\chi}_2^0$) and the lightest chargino ($\tilde{\chi}_1^{\pm}$). It can be seen from these two figures that both $\tilde{\chi}_2^0$ and $\tilde{\chi}_1^{\pm}$ with masses less than $\sim$ 70 GeV/c^2 are ruled out for A_0=0, $sign(\mu)$=-1, $tan(\beta)$=2 and non zero values of the λ'_{1jk} (where j=1, 2 and k=1, 2, 3) couplings.

Chapter 6

Conclusion

Details of a search for R-parity violating supersymmetry in the dielectron plus four jets final state using a data sample of 96 pb^{-1} collected by the DØ detector during the 1994-95 run have been given in the previous chapters. The search was done in the SUGRA framework for fixed values of $A_0 = 0$, $tan\beta = 2$ and $sign(\mu) = -1$ and non-zero values of R-parity violating Yukawa couplings λ'_{1jk} (where j=1,2 and k=1,2,3). In this chapter, the results have been summarised and an outline of future plans is given.

6.1 Summary of Results

In this search it is assumed that supersymmetric particles are pair produced at the Tevatron and decay to Lightest Supersymmetric Particles (LSP s) through R-parity conserving channels. Each LSP is then assumed to decay through R-parity violating channel into ν_e/e + 2 jets. Thus, the event topology considered consists of two or more energetic electrons and four or more energetic jets. A study of the distributions of various variables has been made for simulated signal as well as for various sources of backgrounds. This helped in choosing the following set of selection criteria that suppresses the background significantly while retaining a good efficiency for detection of signal events:

- Trigger: JET_MULTI
- At least two good electrons, one with $E_T \geq 15$ GeV and the other with $E_T \geq 10$ GeV in the region $\mid \eta \mid \leq 1.1$ or $1.5 \leq \mid \eta \mid \leq 2.5$.
  For defining good electron the quality cuts used are
  - Isolation fraction, $f_{iso} < 0.15$

- Shower shape variable, $\chi^2 < 100$, and
- Track match significance, $S < 10$

- At least four jets of $E_T > 15$ GeV in the region $\mid \eta \mid \leq 2.5$

  The quality cuts used for jets are
  - $0.05 \leq f_{EM} \leq 0.95$, where f_{EM} is the electromagnetic fraction of the jets.
  - Coarse hadronic fraction, $f_{CH} < 0.4$
  - ratio of the largest signal to the next-to-largest in the individual cells of the calorimeter, R < 10.

- $\mid m_{ee} - m_Z \mid \geq 15$, where m_{ee} is the invariant mass of the two highest E_T electrons.

With these cuts, we observed 2 events in the data with the expected background of

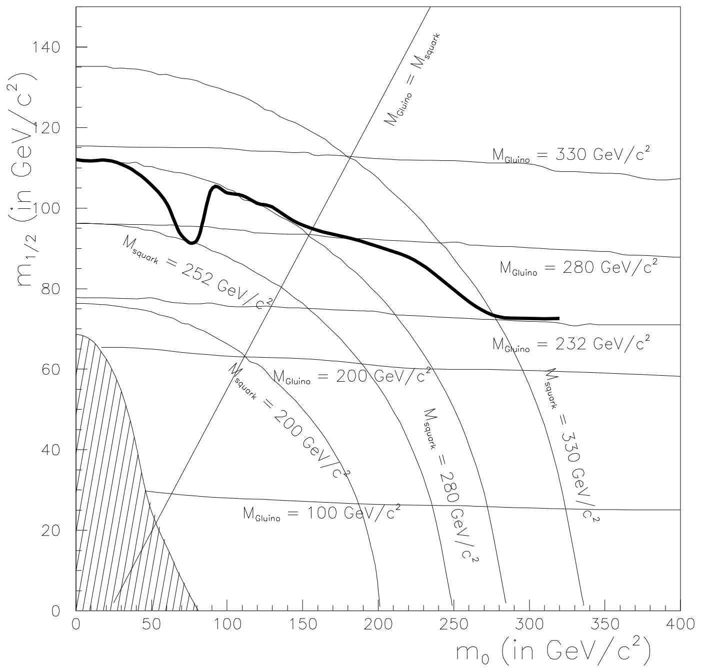

Figure 6.1: Exclusion contour in the $m_0 - m_{1/2}$ plane for $tan(\beta) = 2$, $sign(\mu) = -1$, $A_0 = 0$ and nonzero value of λ'_{1jk} coupling (where j=1,2 and k=1,2,3). The region below the bold line is excluded at 95 % C.L.

1.8 ± 0.4 events. This result has been interpreted in the framework of supergravity with R-parity violation. We have excluded a region in the $m_0 - m_{1/2}$ plane as shown in Fig 6.1.

The mass contours for squarks of the first two generations and gluinos are indicated in the figure. The straight line passes through the points where $m_{\tilde{q}} = m_{\tilde{g}}$. It is seen from Fig. 6.1 that within the SUGRA framework masses of squarks below 252 GeV/c^2 and gluinos below 232 GeV/c^2 are ruled out for fixed values of A_0=0, $sign(\mu)$=-1, $tan(\beta)$=2 and non zero values of λ'_{1jk} (where j=1,2 and k=1,2,3) couplings. For equal masses of squarks and gluinos, the corresponding limit is 283 GeV/c^2. We have also ruled out the lightest chargino and the second lightest neutralino below a mass of $\sim$ 70 Gev/c^2.

6.2 Future plans

In the analysis presented in this thesis, we have worked within the SUGRA framework at fixed values of $A_0 = 0$, $sign(\mu) = -1$ and $\tan(\beta)$=2. At present, work is in progress to extend this analysis to the MSSM framework so that the region where gluinos are much heavier than the squarks can also be explored. After that we plan to study the sensitivity of the result with the variation of $\tan(\beta)$.

In this analysis we have concentrated on the λ' type R-parity violating Yukawa coupling involving electrons. It is necessary to look for λ' terms involving muons in the final state as well as λ terms involving both electrons and muons. Analysis is in progress within the new phenomena group of DØ to explore some of these processes.

With the addition of the Main Injector to the Tevatron it is expected that data corresponding to an integrated luminosity of 2 fb^{-1} will be collected during the year 2000. Moreover, the DØ detector will undergo a substantial upgrade that will improve the identification and measurement capability of leptons. These will certainly help to explore a larger parameter space and widen the chance of discovering supersymmetry.

References

[1] H.E. Haber and G.L. Kane, Physics Reports 117, Nos. 2-4 (1985)

[2] X. Tata, Lectures presented at the Mt. Sorak Symposium on the Standard Model and Beyond, Mt. Sorak (Aug 1990), DØnote 2065

[3] Michael Dine, hep-ph/9612389

[4] S. Dimopoulos, S. Thomas, J.D. Wells, hep-ph/9609434

[5] V. Barger, M.S Berger, P. Ohmann, hep-ph/9311269

[6] M. Dress, hep-ph/9611409

[7] U. Amaldi, W. deBoer, and H. Furstenau, Phys. Lett. 260B, 447 (1991)

[8] D. Freedman, S. Ferrara and P. van Nieuwenhuizen, Phys. Rev. D13, 3214(1976)

[9] R. Barbieri, S. Ferrara and C. Savoy, Phys. Lett. 119B, 343 (1982)

[10] R. Arnowitt, A. Chamseddine and P. Nath, Phys. Rev. Lett., 49, 970 (1982)

[11] B. Campbell, Phys. Rev. D 28, 209 (1983).

[12] S. Dawson, Nucl. Phys., B261, 297(1985)

[13] H. Dreiner, hep-ph/9707435

[14] M. Guchait,D.P. Roy, hep-ph/9707275

[15] A. Abachi, et al., Proceedings of the 28th International Conference on High energy Physics, eds. Z. Adjuk and A. K. Wroblewski (World Scientific, Singapore, 1997), FERMILAB-CONF-96/427-E.

[16] S. Abachi, et al., FERMILAB-CONF-97/357-E

[17] J. Done, Proceedings of 1996 Divisional Meeting of the Division of Particles and Fields, (DPF '96 Minneapolis, MN, 1996), FERMILAB-CONF-96/371-E.

[18] S. Abachi et al., Phys. Rev. Lett. 76, 2222 (1996)

[19] R. Barate et al., Physics Letters B 413, 431 (1997)

[20] R. Barate et al., Physics Letters B 407, 377 (1997)

[21] B. Abbott et al., Phys. Rev. Lett. 80, 1591 (1998)

[22] B. Bevensee, Proceedings of The International Workshop on Quantum Effects in the MSSM, (Barcelona, Spain, 1997), Fermilab-conf-97/405-E.

[23] R. Barate et al., Eur. Phys. J. C2, 417 (1998)

[24] P.D. Acton et al., Phys. Lett. B 313, 333 (1993)

[25] M. Acciarri et al., Phys. Lett. B 414, 373 (1997)

[26] B. Buskulic et al., Phys. Lett. B 349, 238 (1995)

[27] B. Barate et al., Eur. Phys. J. C4, 433 (1998)

[28] S. Aid et al., Z. Phys. C 71, 211 (1996)

[29] D. P. Roy, Phys. Lett. B 283, 270 (1992)

[30] C. Adloff et al., Z. Phys. C 74, 191 (1997)

[31] J. Breitweg et al., Z. Phys. C 74, 207 (1997)

[32] D. Choudhury and S. Raychaudhury, Phys. Lett. B 401, 54 (1997)

[33] D. Choudhury and S. Raychaudhury, Phys. Rev. D 56, 1778 (1997)

[34] M. Chertok, J. P. Dome and T. Kamon, Abstract submitted to ICHEP98, Vaccouver, 1998.

[35] S. Abachi et. al. (DØ). Nucl. Inst. Meth. A338, 185 (1994)

[36] S. Snyder, DØ Internal Note 2500 (1995)

[37] L. Lederman. Scientific American, 264(3), 48 (1991)

[38] H. T. Edwards. Ann. Rev. Nucl. Part.Sci., 35, 605 (1985)

[39] F.T. Cole et al., Design Report Tevatron 1 project, FNAL Internal Note (1984).

[40] F.T. Cole et al., A Report of the Design of the Fermi National Laboratory Superconding Accelerator, FNAL Internal Note (1979)

[41] W.J Thompson, DØ Internal Note 2367 (1994)

[42] J. Bantly et al., DØ Luminosity Monitor Constant for the 1994-94 Tevatron Run, FNAL Technical memo, Fermilab-TM-1995, (1997)

[43] N. Amos et al., Luminosity Calculation for DØ, DØ Note 2031 (1994)

[44] N. Amos et al., Change to the DØ Luminosity Monitor Constant, DØ Note 2186, 1994

[45] F. Sauli, Principles of Operation of Multiwire Proportional and Drift Chambers, Lectures given in the academic training programme of CERN 1975-1976.

[46] A. R. Clark et al. Nucl. Inst. Meth. A261, 420(1987)

[47] A. R. Clark et al. Nucl. Inst. Meth. A279, 243(1989)

[48] A. R. Clark et al. Nucl. Inst. Meth. A315, 193(1992)

[49] R. Fernow. Introduction to Experimental Particle Physics, Cambridge University Press, 1986

[50] K. Kleinknecht. Detectors for Particle Radiation, Cambridge University Press, 1986

[51] J.F. Decœuf et al., Nucl. Inst. Meth. A265,157 (1988)

[52] J.F. Decœuf et al., Nucl. Inst. Meth. A279,310 (1989)

[53] D. Buchhloz et al., Nucl. Inst. Meth. A257, 556 (1987)

[54] T. Bhenke, The Central Drift chamber for DØ Detector: Design, Construction, and Test. Ph.D thesis, SUNY, Stony Brook, New York (1989) (unpublished)

[55] D. Pizzuto, DØ Central Tracking Performance Studies. Ph.D thesis, SUNY, Stony Brook, New York, 1991

[56] S. Rajagopalan, The dE/dx Capability of the DØ tracking System. Ph.D thesis, Northwestern University, Evanston, Illinois, 1992 (Unpublished)

[57] J. W. Bantly, The DØ Forward Drift Chamber Performance and Physics Capability in the 1990 FNAL Testbeam Run. Ph.D thesis, Northwestern University, Evanston, Illinois, 1992 (Unpublished)

[58] C. Fabjan, Calorimetry in High Energy Physics in T.Ferbel editor, Experimental Techniques in high Energy Physics. Addision-Wesley (1987)

[59] U. Amaldi, Fluctuation in Calorimetry Measurements in T.Ferbel editor, Experimental Techniques in high Energy Physics. Addision-Wesley (1987)

[60] S. J. Wimpenny et al., Nucl. Inst. Meth., A279,107 (1989)

[61] A. L. Spadafora et al., Nucl. Inst. Meth., A315,279, (1992)

[62] Paolo Franzini et al. Nucl. Inst. Meth., A289,438, (1990)

[63] Hiroaki Aihara et al. IEEE Trans. Nucl. Sci., 38(2),398, (1991)

[64] C. Brown et al., Nucl. Inst. Meth., A279,331 (1989)

[65] A. Lankford, Trigger and data Acquisition at High Rate colliders in Proceedings of the 20th SLAC Summer Institute, SLAC, Standford, California (1992).

[66] M. Breidenbach, Data Acquisition for High energy Physics Experiments in Proceedings of the 14th SLAC Summer Institute, SLAC, Standford, California (1986)

[67] R.K. Bock, H. Grote, D. Notz and M. Regler, Data Analysis Techniques for High Energy Physics Experiments. Cambridge University Press (190)

[68] G. S. Gao and R. Partridge. IEEE trans. Nucl. Sci., 38(2),286 (1991)

[69] J. Bantly et al. The level 0 trigger for the DØ detector. DØ note 1996. (1993)

[70] M. Abolins et al. The level 1 framework. DØnote 705 (1988)

[71] M. Abolins et al. IEEE Trans. Nucl. Sci., 36(1),384 (1989)

[72] M. Abolins et al. Nucl. Inst. Meth., A289,543 (1990)

[73] J. Butler, Main ring deadtime. DØnote 1682 (1993)

[74] M. Goosens et al., CERN Program Library Long Writeup (1991)

[75] G. manning. DØ Software Documentation.

[76] S. Youssef. Comp. Phys. Comm., 45,423 (1987)

[77] R. engelmann et al. Nucl.Inst. Meth., A216,45 (1983)

[78] M. Narain. Electron Identification in the DØ detecto, FERMILAB-Conf-93/054-E (1993)

[79] G. Arnison et al. (UA1). Phys. Lett. B123,115 (1983)

[80] G. Arnison et al. (UA1). Phys. Lett. B132,214 (1983)

[81] N.J. Hadley. Cone algorithm for jet finding. DØ note 904. (1989)

[82] A. Milder, R. V. Astur, DØnote 1595 (1989)

[83] F. Abe et al. (CDF). Phys. Rev. Lett., 69,2899 (1992)

[84] F. Paige and S. Protopopescu, Brookhaven National Laboratory Report No. 38304 (1986).

[85] H. U. Bengtsson, T. Sjöstrand, PYTHIA $v5.6$, CERN Program Library Long Writeup , CERN (1991).

[86] G. Marchesini, B.R. Webber, G. Abbiendi, I.G. Knowels, M.H. Seymour, Computer Physics Communications 67, 465(1992)

[87] R.D. Field, R.P. Feynman, Nucl. Phys. B136, 1 (1978)

[88] B. Anderson, G. Gustafson, G. Ingelman, and T. Sjöstrand, Phys. Rep. 97, 33 (1983)

[89] R. Brun, F. Carminati, GEANT, CERN Program Library Long Writeup CERN (1993)

[90] J. Womersley, The DØ Monte Carlo, DØnote 1520.

[91] J. Womersley, R. Raja and A. Jonckheere, Shower Libraries for DØ GEANT Monte Carlo, DØnote 650 (1987).

[92] R. Raja, DØ Shower Library, DØnote 1045 (1990).

[93] W. Dharmaratna, R. Raja and C. Stewart, DØ Showerlibrary Version 2.0, DØnote 1730, (1993).

[94] D0$LEVEL1:L1SIM.DOC, DØ documentation file, Dec. 1992.

[95] D. Claes, D0$LEVEL2:L2SIM.DOC, DØ documentation file, Apr. 1994.

[96] R. Avery et al., DØnote 1355, (1992)

[97] S. Chopra, U. Heintz and M. Narain, DØnote 2351 (1994).

[98] D. Norman, private communication.

[99] G. Wang, DØnote 3161 (1997).

[100] S. Abachi et. al (DØ) Phys. Rev. Lett 79, 1203 (1997)

[101] J. Ohnemus, Phys. Rev. D 44, 1403(1991)

[102] H. baer et al., Proceedings of the Workshop on Physics at Current Accelerators and Supercolliders, edited by J. Hewett et al. (Argonne National Laboratory) (1993)

[103] Like sign dilepton signature for gluino production at the CERN LHC with or without R conservation.
H. Dreiner, M. Guchait, D.P Roy. Phys. Rev D 49 3270(1994)

[104] A recipe for the construction of the confidence limit. I. Bertram et. al., DØnote 2775